
# Advanced High Resolution Methods for Radar Imaging and Micro-Doppler Signature Extraction

---

**Carmine Clemente**

**A thesis submitted for the degree of**

**Doctor of Philosophy**

**Centre for Excellence in Signal and Image Processing**

**Department of Electronic and Electrical Engineering**

**University of Strathclyde**

**Glasgow**

**2013**

# Declaration

This thesis is the result of the author's original research. It has been composed by the author and has not been previously submitted for examination which has led to the award of a degree.



Carmine Clemente January 24, 2013

To my family.

# Acknowledgement

It is a pleasure to thank the many people who made this thesis possible. I would like to begin with thanking my supervisor Prof. John Soraghan for giving me an excellent opportunity to carry out a very innovative and challenging research. Prof. Soraghan provided me endless source of ideas and encouragement. His enthusiasm in research, systematic organisation in work and optimistic attitude towards life positively influenced my study and life.

Thanks also to my second and third supervisors Dr Ian Glover and Dr Des McGhee for their support and technical help.

Thanks to my sponsors, the Engineering and Physical Research Council (grant N. EP/H012877/1), the MOD University Defence Research Centre in Signal Processing and Selex-Galileo Edinburgh.

My deepest and sincere thanks are always to my family for its constant support.

A big thank you to Gaetano di Caterina, my very first point of reference in Glasgow, a good friend and colleague.

I would like to thank all my friends here in Glasgow that supported and stood me during my stressed days. The same friends that helped me in forgiving the fatigue of research. Thanks to Armando, Filippo, Daniele, Grace, Domenico, Ilaria, Giacomo, Jessica, Davide, Beppe, Enrica, Francesco, Electra, Marco, Maria Pia...and all the people whom carved Glasgow on my heart.

Thanks to my friends in Italy for their encouragement and unconditioned support. Thanks to Marica, Peppe, Maria, Agnese, Emanuela, Francesco e Renato.

Lastly, and most importantly, I owe my loving thanks to Alessia for her understanding, patience and encouragement.

# Abstract

This Thesis presents radar concepts and signal processing techniques including the fractional Fourier transform (FrFT), Chebyshev polynomial approximation and Singular Spectrum Analysis (SSA) for advanced high resolution radar imaging and micro-Doppler signature extraction.

Two novel SAR focussing algorithms in the time-frequency domain are developed using the FrFT. These are called the Fractional Range Doppler Algorithm (FrRDA) and the enhanced Fractional Chirp Scaling Algorithm (eFrCSA. The new methods are tested on simulated and real data sets and are shown to provide higher performances in terms of image quality and resolution than existing frequency domain based methods.

The state of the art signal spectrum models of a bistatic point target spectrum for bistatic SAR imaging has been improved by deriving Chebyshev polynomial approximations in place of the conventional Taylor based approximations. This new model increases the accuracy and the efficiency of frequency domain focussing algorithms.

Models for micro-Doppler signatures in bistatic SAR are developed and the effect of the different acquisition geometries are considered, including the effect on the final image.

A new concept for a Passive Bistatic Radar is introduced for micro-Doppler analysis of helicopters rotor blades. The proposed system exploits the forward scattering enhancement to increase the radar cross section of the helicopters rotor blade allowing an acceptable operative range. The analysis shows how the proposed system could be considered as a good candidate for cheap coast and border control.

A detailed analysis on the effect of micro-Doppler from wind turbines and

their impact on SAR images is presented. The signal model for such a distributed target is presented and simulation results show how the presence of such a target can significantly decrease and corrupt the image quality. Singular Spectrum Analysis (SSA) is developed for micro-Doppler signature extraction from SAR clutter and from the direct signal interference and clutter of a passive bistatic radar. The SSA is shown to be robust and capable of performing as a useful tool with the capability of mitigating the effects of clutter on micro-Doppler signatures.

# Contents

# List of Figures

# List of Tables

# List of Abbreviations

**2D** - Two Dimensional

**AF** - Ambiguity Function

**AOK** - Adaptive Optimal Kernel

**BPTS** - Bistatic Point Target Spectrum

**BSAR** - Bistatic Synthetic Aperture Radar

**CEMD** - Complex Valued Empirical Mode Decomposition

**CIRT** - Complex-valued Inverse Radon Transform

**CPI** - Coherent Processing Interval

**CSA** - Chirp Scaling Algorithm

**DMO** - Deep Move Out

**DSI** - Direct Signal Interference

**eFrCSA** - enhanced Fractional Chirp Scaling Algorithm

**FFT** - Fast Fourier Transform

**FrCSA** - Fractional Chirps Scaling Algorithm

**FrFT** - Fractional Fourier Transform

**FrRDA** - Fractional Range Doppler Algorithm

**GNSS** - Global Navigation Satellite System

**GPS** - Global Positioning System

**IFFT** - Inverse Fast Fourier Transform

**IMF** - Intrinsic Mode Function

**ISAR** - Invere Synthetic Aperture Radar

**ISLR** - Integrated SideLobe Ratio

**LBF** - Loffeld's Bistatic Formula

**LOP** - Local Optimization Procedure

**LRCM** - Linear Range Cell Migration

**m-D** - micro-Doppler

**mmW** - millimeter Wave

**MSP** - Modular SAR Processor

**MSR** - Method of Series Reversion

**NLCSA** - Non-Linear Chirp Scaling Algorithm

**PBR** - Passive Bistatic Radar

**PEP** - Paired Echoes Principle

**PRF** - Pulse Repetition Frequency

**PRN** - Pseudo Random Noise

**PSLR** - Peak SideLobe Ratio

**PSP** - Principle of Stationary Phase

**PTS** - Point Target Spectrum

**PWVD** - Pseudo Wigner-Ville Distribution

**RCMC** - Range Cell Migration Correction

**RCS** - Radar Cross Section

**RDA** - Range Doppler Algorithm

**RIRT** - Real-valued Inverse Radon Transform

**SAR** - Synthetic Aperture Radar

**SCR** - Signal to Clutter Ratio

**SNR** - Signal to Noise Ratio

**SSA** - Singular Spectrum Analysis

**SSL** - SideLobe Level

**SVD** - Singular Value Decomposition

**TFR** - Time Frequency Distribution

**UK** - United Kingdom

**WVD** - Wigner-Ville Distribution

# List of Symbols

### Section 2.4

| | |
|---|---|
| $\eta$ | Slow time |
| $\hat{R}(\cdot)$ | Taylor series expansion of $R(\cdot)$ |
| $\Phi_{2df}(\cdot,\cdot)$ | Phase of the 2D point target spectrum |
| $\rho(\cdot)$ | Compressed range envelope |
| $\tau$ | Fast time |
| $\theta$ | Fractional transformation angle |
| $\theta_{opt}$ | Optimum fractional transformation angle |
| $\theta_{sqR}$ | Receiver squint angle |
| $\theta_{sqT}$ | Transmitter squint angle |
| $a$ | Fractional transformation Order |
| $A_0$ | Amplitude coefficient |
| $A_i$ | Amplitude coefficient |
| $c$ | Speed of light |
| $f_0$ | Carrier frequency |
| $f_\eta$ | Azimuth frequency variable |
| $f_\tau$ | Range frequency variable |

| | |
|---|---|
| $F_s$ | Sampling frequency |
| $K_a(\cdot,\cdot)$ | FrFT kernel |
| $k_i$ | Taylor series coefficient |
| $K_r$ | Transmitted chirp rate |
| $N$ | Number of samples |
| $R(\cdot)$ | Instantaneous 2 way slant range |
| $R_{cen}$ | Sum of $R_{T_{cen}}$ and $R_{R_{cen}}$ |
| $R_{R_{cen}}$ | Receiver range distance at $\eta = 0$ |
| $R_{T_{cen}}$ | Transmitter range distance at $\eta = 0$ |
| $s(\cdot,\cdot)$ | Received signal |
| $S_1(\cdot,\cdot)$ | Fourier transform of $s_1(\cdot,\cdot)$ |
| $s_1(\cdot,\cdot)$ | Range compressed signal rearranged before the MSR |
| $S_{2df}(\cdot,\cdot)$ | 2D point target spectrum |
| $s_{rc}(\cdot,\cdot)$ | Range compressed signal |
| $u$ | Generic domain |
| $u'$ | Generic domain |
| $V_r$ | Receiver velocity |
| $V_T$ | Transmitter velocity |
| $W_r\cdot$ | Fourier transform of $w_r(\cdot)$ |
| $W_{az}(\cdot)$ | Fourier transform of $w_{az}(\cdot)$ |
| $w_{az}(\cdot)$ | Composite antenna pattern |
| $w_r(\cdot)$ | Range envelope |

**Section 2.5**

| | |
|---|---|
| $\bar{\Phi}_{RCM}(\cdot)$ | RCM phase component |
| $\beta_a$ | Azimuth scaling factor |
| $\lambda$ | Carrier wavelength |
| $\mu_c$,$\mu_{r1}$,$\mu_{r2}$ | Support variables |
| $\mu_{t1}$,$\mu_{t2}$ | Support variables |
| $\Phi_R(\cdot)$ | Receiver phase modulation contribute |
| $\Phi_T(\cdot)$ | Transmitter phase modulation contribute |
| $\Phi_{AC}(\cdot,\cdot)$ | Azimuth compression phase contribute |
| $\Phi_{AS}(\cdot,\cdot)$ | Azimuth scaling phase contribute |
| $\Phi_{RCMC}(\cdot,\cdot,\cdot)$ | RCM phase contribute |
| $\Phi_{RC}(\cdot,\cdot)$ | Range compression phase |
| $\Phi_{res}(\cdot,\cdot)$ | Residual phase component |
| $\Psi_B(\cdot,\cdot,\cdot)$ | Bistatic PTS |
| $\sigma(\cdot,\cdot)$ | Reflectivity profile |
| $\tau$ | Slow time |
| $\tau_{0R}$ | Azimuth time of closest approach |
| $\tau_{cb}$ | Azimuth center time |
| $\tilde{\tau}_R(\cdot)$ | Receiver time-Doppler correspondence |
| $\tilde{\tau}_T(\cdot)$ | Transmitter time-Doppler correspondence |
| $D_R$, $D_T$ | Support variables |
| $f_{\tau R}$ | Receiver azimuth frequency |

| | |
|---|---|
| $f_{\tau T}$ | Transmitter azimuth frequency |
| $f_{DcR}$ | Receiver Doppler Centroid |
| $f_{DcT}$ | Transmitter Doppler Centroid |
| $g(\cdot,\cdot,\cdot,\cdot)$ | Received signal |
| $K_{aR}$ | Receiver azimuth modulation rate |
| $K_{aT}$ | Transmitter azimuth modulation rate |
| $p_{ij}$ | Coefficients of the geometrical image transformation |
| $R_R(\cdot)$ | Receiver to target slant range |
| $R_T(\cdot)$ | Transmitter to target slant range |
| $R_{0R}$ | Range at closest approach |
| $s_l(\cdot)$ | Range envelope |
| $t$ | Fast time |
| $v_r$ | Receiver velocity |
| $v_t$ | Transmitter velocity |

**Chapter 3**

| | |
|---|---|
| $\alpha$ | Radar azimuth angle |
| $\beta$ | Radar elevation angle |
| $\lambda_c$ | Carrier wavelength |
| $\rho$ | Target backscattering coefficient |
| $\Theta(\cdot)$ | Instantaneous aspect angle |
| $D_(\cdot)$ | Displacement function |
| $D_v$ | Vibrating displacement |

$f_v$ Vibrating frequency

$f_{mD_{rot}}(\cdot)$ Rotating micro-Doppler frequency

$f_{mD_{vib}}(\cdot)$ Vibrating micro-Doppler frequency

$f_{md}(\cdot)$ Micro-Doppler frequency

$J_k(\cdot)$ Bessel function of the first kind

$s_b(\cdot,\cdot)$ Baseband received signal

**Chapter 4**

$\tau_{start}$ Start sampling time of the linear chirp

$\tau_{stop}$ Stop sampling time of the linear chirp

$\theta_{opt_{az}}$ Optimum fractional transformation order in the azimuth direction

$\theta_{opt_{rg}}$ Optimum fractional transformation order in the range direction

$dur$ Duration of the acquisition

$k_{az}$ Azimuth modulation rate

$k_{rg}$ Range modulation rate

**Chapter 5**

$\chi(\cdot,\cdot)$ Support variable

$\hat{\Phi}_{AC}(\cdot,\cdot)$ Chebyshev approximation of $\Phi_{AC}(\cdot,\cdot)$

$\hat{\Phi}_{RCM}(\cdot,\cdot)$ Chebyshev approximation of $\Phi_{RCM}(\cdot,\cdot)$

$\hat{\Phi}_{RC}(\cdot,\cdot)$ Chebyshev approximation of $\Phi_{RC}(\cdot,\cdot)$

$\hat{\Psi}_B(\cdot,\cdot)$ Bistatic PTS using 2DPSP and Chebyshev approximation

$\hat{F}_R(\cdot)$ Chebyshev approximation of $F_R(\cdot)$

$\hat{F}_T(\cdot)$ Chebyshev approximation of $F_T(\cdot)$

| | |
|---|---|
| $\hat{R}_{Cheb}(\cdot)$ | Chebyshev polynomial approximation of $R.$ |
| $c_k$ | Chebyshev coefficient |
| $F_R(\cdot)$ | Range frequency coupling term |
| $F_T(\cdot)$ | Azimuth frequency coupling term |
| $f_k$ | Chebyshev node |
| $f_{max}$ | Maximum frequency |
| $f_{min}$ | Minimum frequency |
| $g_k$ | Support variable |
| $T_k(\cdot)$ | Chebyshev polynomial |

**Chapter 6**

| | |
|---|---|
| $\Phi(\cdot)$ | Phase of the received signal |
| $\Phi_{BSAR}(\cdot)$ | Bistatic SAR signal phase |
| $\Phi_{Target}(\cdot)$ | Phase modulation due to the target motion |
| $\rho$ | Bistatic factor |
| $A_v$ | Vibrating amplitude |
| $f_{BSAR}(\cdot)$ | Doppler frequency due to the bistatic SAR |
| $f_D(\cdot)$ | Doppler frequency |
| $f_{MD_{mono}}(\cdot)$ | Micro-Doppler shift for the monostatic case |
| $f_{MD}(\cdot)$ | Micro-Doppler frequency shift |
| $N(\cdot)$ | Displacement function |
| $P$ | Position of the point target |
| $R_{BSAR}(\cdot)$ | Bistatic SAR slant range |

| | |
|---|---|
| $R_{GR}$ | Receiver ground range |
| $R_{GT}$ | Transmitter ground range |
| $R_{Target}(\cdot)$ | Slant range modulation due to the target motion |

**Chapter 7**

| | |
|---|---|
| $\beta$ | Solid bistatic angle |
| $\Delta f_{Bi}$ | Bistatic Doppler resolution |
| $\Delta f_{Mono}$ | Monostatic Doppler resolution |
| $\delta$ | Angle between the bisector of the bistatic angle and the velocity vector |
| $\hat{\mathbf{\Omega}}$ | Estimated blade rotation rate |
| $\hat{f}_{mD_{max}}$ | Estimated maximum micro-Doppler shift |
| $\hat{L}_b$ | Estimated blade length |
| $\mathbf{\Omega}$ | Angular rotation rate |
| $\Phi_R\cdot$ | Phase modulation due to the target range |
| $\Phi_{mD}$ | Micro-Doppler phase modulation |
| $\sigma_b$ | Bistatic radar cross section |
| $\sigma_{b_{peak}}$ | Maximum bistatic radar cross section |
| $\theta_0$ | Initial phase |
| $A$ | Target silhouette area |
| $BW$ | Signal bandwidth |
| $f_{mD_k}$ | Micro-Doppler shift from the $k$ blade |
| $f_{mD_{max_{mono}}}$ | Maximum micro-Doppler shift for the monostatic case |
| $f_{mD_{max}}$ | Maximum micro-Doppler shift |

| | |
|---|---|
| $G_r$ | Receiver antenna gain |
| $G_t$ | Transmitter antenna gain |
| $G_{sp}$ | Processing gain |
| $k$ | Boltzmann constant |
| $L_b$ | Blade length |
| $L_{sp}$ | Processing losses |
| $P_r$ | Received power |
| $P_t$ | Transmitted power |
| $R_{R_{max}}$ | Maximum detectable range |
| $S_r$ | Received power density |
| $S_{dir}$ | Direct signal power density |
| $s_{tot}(\cdot,\cdot)$ | Total received signal |
| $T_{eff}$ | Equivalent noise temperature |
| $W_b$ | Blade width |

**Chapter 8**

| | |
|---|---|
| $\Phi_{WT_i}(\cdot)$ | Phase modulation induced by a wind turbine rotor blade |
| $\theta_g$ | Observation angle between the platform and the wind turbine |
| $\theta_t$ | Rotation angle between the rotor and the platform flight track |
| $\tilde{\mathbf{X}}$ | Reconstructed trajectory matrix |
| $f_{WT_i}(\cdot)$ | Doppler Shift induced by a wind turbine rotor blade |
| $K$ | Number of time series to be embedded |
| $L$ | Embedding length |

| | |
|---|---|
| $Y_N$ | Generic time series |

**Appendix A**

| | |
|---|---|
| $a_i$ | Series coefficient |
| $e^2$ | Square residual of the function approximation |
| $x_k$ | Chebyshev node |

# Chapter 1

# Introduction

## 1.1 Preface

From its earliest days the use of radar was oriented to detect and track targets accurately. The capability to operate in hostile weather and day and night were two great advantages of the use of electromagnetic waves that facilitated intense research and diffusion of radar system for military and civil applications.
Time delay initially measured to perform target ranging was followed by antenna directivity to measure the angle of arrival and then Doppler shift to measure target velocities.
Exploiting the Doppler shift in high resolution radar imaging was one of the most innovative applications brought to the attention of the radar community by Carl Wiley of Goodyear Aerospace in 1951. The introduced method was named ”Synthetic Aperture Radar” referring to the equivalence of the series successive acquisition with a long aperture antenna.
SAR data collected by a the radar system appears as random noise. This is due to the superposition of all the echoes received from all the scatterers in the real antenna footprint for each acquisition. In order to retrieve the information contained in the phase of the received signal a phase-sensitive processing is required to obtain a focused image. The first methods used to focus SAR images were based on optical sensors, the data were recorded on a black and white film and a laser beam was collimated and shone through the film while lenses where used to perform a real time 2D Fourier transform.

Finally diffraction gratings were used to focus the data and a last set of lenses was used to perform the inverse Fourier transform Cumming and Wong [2005]. However the use of optical processor even providing high quality and real time images had the following drawbacks: very high-quality lenses were required, a skilled operator was always needed and the automation of the process was not possible, in addition the dynamic range of the final image was limited by the black and white film.

In the late 1970s SAR data started to be digitalized and recorded on tape or disk. The first digital processor were able to process an image in 40 hours, much different from what can be done with the modern computing systems Clemente et al. [2009].

For this reason much of the research effort moved in the direction of efficient and accurate focussing algorithm, Range Doppler, Chirp Scaling, $\Omega - k$ and SPECAN are the name of the most efficient solutions achieved from the SAR community to obtain high quality images in a reasonable amount of time.

Traditional SAR systems were designed to be monostatic, the transmitting antenna is the same that receives the radar returns. However in recent years the international community has become particularly active in the case of a receiver placed on a different platform, spatially separated from the transmitter, the Bistatic SAR configuration (BSAR). This acquisition configuration introduces new challenges for the signal processing community, in particular for the focussing stage where the phase history of the acquired signal results to be strongly geometry dependent and obtain an accurate and efficient focussing algorithm becomes an hard goal to achieve.

Another successful exploitation of the Doppler effect is the micro-Doppler signature analysis Chen [2011]. The Micro-Doppler effect was originally introduced in coherent laser system to measure kinematic properties of objects such as a frequency of a vibration or its amplitude. Micro-Doppler shifts characterize the complex features of an object. Unlike the laser case, in microwave radar systems the amplitude of the observable micro-Doppler shift is much smaller due to the relatively longer wavelength. However if the product between the the displacement amplitude and its frequency is sufficiently big it is possible to observe a micro-Doppler effect. For example helicopters rotor blades or rotating antennas for air traffic control can introduce an observable effect due to their long arms.

The knowledge of micro-Doppler signature is of interest for civil and military applications. Micro-Doppler signature is the description of details of a target. For this reason, the micro-Doppler signature is a potential rich source of information that can be used for a variety of applications. Micro-Doppler can be regarded as a unique signature of the target that provides additional information about the target that is complementary to existing methods. Specific applications include the recognition of space, air, and ground targets. For example, the micro-Doppler effect can be used to identify specific types of vehicles and determine their movement and the speed of their engines. Vibrations generated by a vehicle engine can be detected by radar signals returned from the surface of the vehicle. For example, from micro-Doppler modulations in the engine vibration signal, one can distinguish whether it is a gas turbine engine of a tank or the diesel engine of a bus Chen [2011]. The outfield measurement of ground targets indicates that micro-Doppler signatures have great significance for vehicle recognition. Micro-Doppler signatures can also be used for human classification at a distance since radar has the advantage of detecting and identifying humans at distances in all weather conditions at day or night Chen [2011].

## 1.2 Motivation

The aim of this thesis is to explore new signal processing techniques and models which can be used to improve the resolution of frequency domain monostatic SAR focussing algorithms, increasing the accuracy of bistatic SAR focussing algorithms and the analysis of micro-Doppler signature from SAR platforms and radar. The objectives of the research presented in this thesis are: the development of an high resolution monostatic SAR focussing approach for range-Doppler algorithms; the increasing of the accuracy of the bistatic point target spectrum model for bistatic SAR focussing; the development of a model for the micro-Doppler signature from bistatic SAR; a feasibility study for a passive bistatic radar for helicopters classification; the effect of wind turbines in SAR images and the application of signal processing techniques to extract it from the data. The thesis will address the enhancements, modifications, and inventions required to achieve high quality SAR images and exploitation of the micro-Doppler signatures.

## 1.3 Contribution

The research detailed in this thesis includes original contributions to the field of monostatic SAR, bistatic SAR, micro-Doppler analysis in Bistatic SAR, micro-Doppler analysis from passive radars, effect of micro-motions on SAR images and micro-Doppler extraction. These contributions are as follows:

1. Two new Fractional Fourier Transform (FrFT) based SAR processing algorithms are presented namely the Fractional Range Doppler Algorithm and the enhanced Fractional Chirp Scaling Algorithm that are shown to improve the well established Range Doppler Algorithm and Chirp Scaling Algorithm for SAR processing. The performance of the algorithms are assessed using simulated and real Radarsat-1 data sets. The results confirm that the FrFT based SAR processing methods provide enhanced resolution yielding both lower side-lobes effects and improved target detection;

2. A new approach to the approximation of the slant range function using Chebyshev polynomials in order to obtain a polynomial representation that can be used in the method of series reversion to obtain a more accurate version of the point target spectrum. The proposed approach replaces the coefficients of the polynomial Taylor series expansion of the bistatic slant range function with the ones obtained using the Chebyshev polynomial approximation. The obtained coefficients are then used to obtain an analytical formulation of the bistatic point target spectrum. Compared to the Legendre approximation, proposed in literature, the Chebyshev polynomials allow us to obtain a least squares approximation of the slant range function that includes the property of a bounded maximum error thus minimizing the so called Runge effect. In addition the mathematical and computational complexity is reduced;

3. The Chebyshev approach is applied to the bistatic point target spectrum based on the 2D Principle of Stationary Phase. In the proposed approach the Chebyshev approximation replaces the coefficients of the polynomial Taylor series expansion of the azimuth-range frequency coupling term. The obtained coefficients

are then used to obtain an analytical formulation of the bistatic point target spectrum. The new approach is shown to provide a more accurate approximation reducing the phase error. The accuracy improvement is shown to yield a more accurate spectrum that can be exploited in bistatic SAR focussing algorithms, improving their accuracy and efficiency;

4. The model for vibrating micro-Doppler signature for a Bistatic SAR system with fixed receiver is analysed and compared to the signature obtained in a monostatic SAR system. The micro- Doppler effect is derived for a vibrating target in the bistatic SAR. The corresponding bistatic factor is shown to be a function of the bistatic acquisition geometry. Also, the effect of the target vibration on the focused image is shown to be influenced by the acquisition geometry. The derived model is useful for micro-Doppler classification. Simulations for 94 GHz and 10 GHz are given and the results confirm the derived model;

5. A novel passive bistatic radar (PBR) using Global Navigation Satellite Systems (GNSS) operating in the near forward scattering zone is presented. The analysis focuses on the case of helicopters rotor blades where the Doppler shift is relatively high and a relatively large wavelength is useful in reducing the maximum Doppler shift. The power budget analysis for this kind of configuration and target is analysed. It is demonstrated the possibility of detecting these kind of targets and to measure their micro-Doppler signatures. The theoretical analysis is supported with simulations that demonstrate the effectiveness of the proposed configuration for micro-Doppler signature analysis for helicopter rotor blades;

6. The effect on SAR images introduced by rotating wind turbines is modelled and analysed. The results show that an image can appear corrupted and that smearing and ghost echoes can possibly hide details of the images that can be distant from the wind turbine. The effect for different aspect angles and rotating blade velocities are analysed through simulations.

7. A micro-Doppler signature extraction method based on the Singular Spectrum Analysis is applied to extract the target micro-Doppler features from the received

SAR and PBR signals. The effectiveness of the proposed approach is confirmed through simulations even in low Signal to Clutter Ratio (SCR);

## 1.4 Thesis organization

The remainder of this thesis is divided into eight chapters, the organization of which is explained as follows: Chapter 2 provides an overview of synthetic aperture radar imaging techniques for monostatic and bistatic SAR. It starts with the SAR processing geometry. Then the frequency domain algorithms for monostatic SAR focussing are introduced. The fractional Fourier transform based CSA is introduced and discussed. Following the bistatic SAR focussing algorithms are presented with particular attention to the bistatic point target spectra obtained with the method of series reversion and the 2D principles of stationary phase.

Chapter 3 reviews the micro-Doppler effect. First the basic concepts of the micro-Doppler effect in radar are introduced. The micro-Doppler effect in radar imaging systems is then reviewed providing an overview of the state of the art in the field.

Chapter 4 introduces the first novelty in this thesis. The Fractional Range Doppler Algorithm and the enhanced Fractional Chirp Scaling Algorithm. The algorithms are described and their performances are compared with the traditional RDA and CSA respectively on both simulated and real data.

Chapter 5 focusses on the frequency domain processing for bistatic SAR imaging. The chapter derives two improved bistatic point target spectra using the Chebyshev approximation. The bistatic point target spectrum using the Method of Series Reversion is improved by replacing the Taylor approximation of the bistatic slant range function with its Chebyshev polynomial approximation. The bistatic point target spectrum using the 2D principle of stationary phase is improved by replacing the Taylor approximation of the range-azimuth frequency coupling terms with its Chebyshev approximation. The new models are tested with simulated data.

Chapter 6 derives the model for the micro-Doppler signature in bistatic Synthetic Aperture Radar. First the fixed receiver geometry is introduced, then the signal model is derived. The analysis concentrates on the different effect of the geometry on the fo-

cussed image and on the micro-Doppler signatures. The derived model are tested and confirmed by simulations.

Chapter 7 introduces a novel passive bistatic radar concept using a GNSS illuminator of opportunity for micro-Doppler analysis in the case of helicopters rotor blades. The system geometry and the signal model are introduced, then the analysis focus on the system requirements for the micro-Doppler analysis. The forward scattering enhancement is introduced to support the power budget analysis. Simulation results concludes the chapter.

Chapter 8 describes advanced micro-Doppler analysis and extraction. The chapter starts analysing the effect of wind turbines on SAR images. The effect is analytically described and the derived model is confirmed through simulations. Then the chapter describes the application of the singular spectrum analysis for the extraction of the micro-Doppler signatures from the clutter. The technique has been applied to simulated SAR data and to the data coming from the PBR scenario described in chapter 7.

Chapter 9 includes a summary and conclusions of this thesis are presented, along with a discussion of its limitations and suggestion of potential areas for further future work. The appendix contains theoretical material about the Chebyshev polynomial approximation which would impede the flow of the thesis. A list of the author's publications is also provided.

# Chapter 2

# Monostatic and Bistatic SAR Imaging

## 2.1 Introduction

Synthetic Aperture Radar (SAR) is an imaging radar system for earth observation from satellite and airborne manned/unmanned platforms. It is currently operational in recently launched polar-orbiting platforms such as TerraSAR-X, RadarSAT-2 and Cosmo-SkyMed as well as in numerous other missions. Applications are diverse including disaster observation and management, mapping of renewable resources, geological mapping, snow/ice mapping and strategic surveillance of military sites. Moreover, the scientific community is more and more oriented to a wide range of applications where the first step is the production of a SAR image Cumming and Wong [2005]. Obtaining optimum resolution from raw SAR data involves sophisticated signal processing techniques especially using high resolution sensors (like TerraSAR-X and Cosmo-SkyMed) where the feature of the smaller scatterers increase in importance. In this chapter the basics of SAR imaging are be introduced. The discussion focusses on imaging algorithms in the range-Doppler domain for monostatic SAR. The analysis concentrates on the Range Doppler Algorithm (RDA) and on the Chirp Scaling Algorithm (CSA). The Fractional Fourier Transform based CSA is then introduced. The understanding of the processing steps of these three algorithms is important since they are exploited in the derivation of the Fractional RDA and Enhanced Fractional CSA (Chapter 4).

The discussion then moves on the case of transmitter and receiver located on different

positions, the bistatic SAR case. The focussing problem in the bistatic SAR case is described and the different approaches for the development of an accurate focussing strategy in the frequency domain are analysed. In particular two models for the bistatic point target spectrum (BPTS) are analysed in detail: the BPTS based on the Method of Series Reversion (MSR) and the BPTS derived using the 2D Principle of Stationary Phase (2D PSP). These two models are important for the understanding of this thesis since their improvement is obtained using the Chebyshev approximation (Chapter 5).

## 2.2 SAR processing geometry

The basic geometry of the SAR processing application is shown in Figure 2.1. The

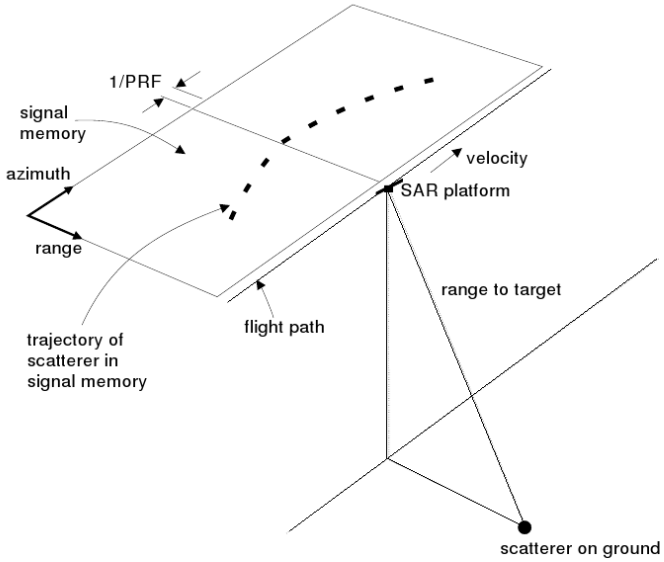


Figure 2.1: SAR processing geometry

sensor transmits a pulse and receives the echoes in a direction approximately perpendicular to the direction of travel. The received signal is digitized and stored in the memory of the signal processor as a two dimensional array of samples. One dimension of the array represents the distance in the slant range direction between the sensor and the target and is commonly referred to as the *range* direction. The other dimension represents the along-track or *azimuth* direction. Each line of data with common azimuth index represents data collected during one pulse repetition interval.

In essence, the processing of SAR data is a two-dimensional space-variant convolution.

When the received data is viewed as a superposition of returns from point scatters, the processing problem consists of compressing the target response that is spread out in both range and azimuth to a single point. As the range and azimuth time scales are so different, the range and azimuth directions can be treated separately during processing. In each dimension the data is convolved with a matched filter. In azimuth, the situation is complicated due to the returned signal from a single point target appears in a number of range cells during the time that it is illuminated by the radar. The energy corresponding to a target needs to be collected into one range cell before it can be compressed using the matched filter Cumming and Wong [2005].

In order to process SAR data to its full inherent resolution with reasonable computing resources, an algorithm is required that is both accurate and efficient. The range-Doppler domain focussing algorithms satisfies these requirements and are discussed in the next section.

## 2.3 Range Doppler Algorithm and Chirp Scaling Algorithm

The Range Doppler Algorithm (RDA) is a simple and efficient algorithm used to focus SAR data. It was first developed by MacDonald Dettwiler and Associates (MDA) and the Jet Propulsion Lab (JPL) in 1979 for the processing of SEASAT data Bamler et al. [1993]; C.Wu [1976, 1977]. It is a very flexible algorithm and widely used. This algorithm takes advantage of the approximate separability of processing in range and azimuth direction, allowed by the large difference in the time scales of the range and azimuth data. In addition efficient range cell migration correction (RCMC) is performed in the so called range-Doppler domain which is the ideal reference plane to correct the hyperbolic behaviour of the target trajectories Cumming and Wong [2005]. The RDA is actually one of the most used algorithms in both research and commercial fields due to its effectiveness and relative simplicity. RDA processors have been developed in the Gamma Remote Sensing Modular SAR processor Werner et al. [2000] and in the REA processor Eon. In addition many research groups work with the RDA and the interest on this algorithm is growing especially in the field of the parallel SAR

processing Clemente et al. [2009]; di Bisceglie et al. [2010]; Giancaspro et al. [2002]. The algorithm is designed to achieve block processing efficiency, using frequency domain operations in both range and azimuth, while maintaining the simplicity of the one-dimensional operations. Block processing efficiency is also achieved for the RCMC operation because it is done in the range time and azimuth frequency domain. This domain is called the "range Doppler" domain, since azimuth frequency is synonymous with Doppler frequency. The algorithm is called the Range Doppler Algorithm (RDA), because the fact that RCMC is performed in this domain and it is the most distinguish feature of the algorithm. Energy from point targets, at the same range but separated in azimuth, is transformed to the same location in the azimuth frequency domain. Therefore, correction of one target trajectory in this domain effectively corrects a family of target trajectories that have the same slant range of closest approach. This is a key feature of the algorithm, which allows RCMC to be implemented efficiently in the range Doppler domain.

To obtain an efficient implementation all matched filter convolutions are performed as multiplies in the frequency domain. Matched filtering and RCMC depend on range varying parameters.

The RDA also distinguishes itself among frequency domain algorithms by its capability to explicitly accommodate range variation of parameters with relative ease. This is another key feature of the algorithm. Moreover all operations are performed with one-dimensional data arrays, hence achieving processing simplicity and efficiency.

The core steps in the algorithm are shown in Figure 2.2 and are described below.

1. **Range Compression**

   Range Compression is obtained multiplying data in the range frequency domain with the range reference function in range direction, so first an FFT is performed on the data in the range direction; then the multiplication with the reference function is performed. To complete the range compression an IFFT is needed to report range direction data in the time domain;

2. **Azimuth FFT**

   An FFT is done in the azimuth direction, obtaining data in the range-Doppler

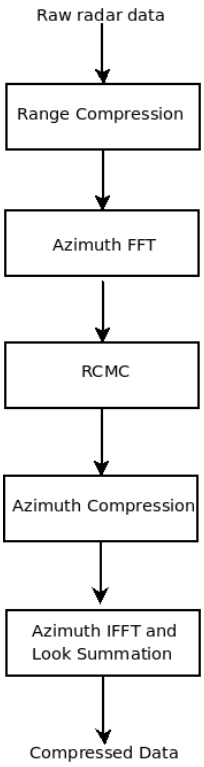


Figure 2.2: Range-Doppler SAR processing algorithm

domain;

3. **Range Cell Migration Correction (RCMC)**
   Range cell migration correction is performed by a shift and interpolation operation that lines up the target trajectories;

4. **Azimuth Compression**
   Azimuth compression is accomplished multiplying data with the azimuth reference function in azimuth direction;

5. **Azimuth IFFT**
   An IFFT in the azimuth direction completes the formation of the image, at this stage detection and look summation can be done.

The CSA was developed to specifically eliminate the interpolation step used for the RCMC Raney et al. [1994]. It is based on the scaling principle applying a frequency modulation to a chirp-encoded signal to achieve a shift or scaling of the signal. The chirp scaling algorithm presents two main advantages, the first one is the possibility

to implement the RCMC with a phase multiplication and the second one is that the secondary range compression (SRC) can be made azimuth frequency dependent.

The chirp scaling algorithm requires only Fast Fourier Transforms (FFTs) and complex vector multiplications and can process SAR data collected in either stripmap or spotlight mode Cumming and Wong [2005]. The algorithm operates in both range-Doppler domain and the 2-D frequency domain. The sequence of core steps of the CSA is shown in Figure 2.3. To obtain the SAR focused image the CSA performs the

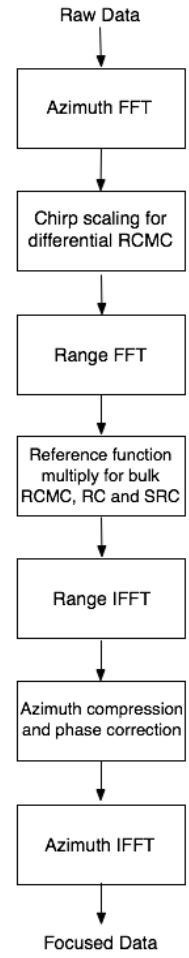


Figure 2.3: Chirp Scaling SAR processing algorithm

following steps:

1. **Azimuth FFT**, using Fast Fourier Transforms to bring the data to the range–Doppler domain.

2. **Chirp Scaling**, in order to equalize the range migration of all targets trajectories a

phase shift is applied along the constant azimuth frequency lines.

3. **Range FFT**, in this step the FFTs in the range direction bring the data in the 2-D frequency domain.

4. **Range Compression, SRC, and bulk RCMC**, are performed through a phase multiplication with a reference signal.

5. **Range IFFT**, to bring the data again in the range–Doppler domain the Inverse Fast Fourier Transfoms are used in the range direction.

6. **Azimuth compression**, a phase multiplication is performed to compress the data along the azimuth direction, in addition a phase correction is applied using a range-varying reference signal.

7. **Azimuth IFFT**, in order to obtain the focused image in the 2-D time domain the Inverse Fast Fourier Transforms are used in the azimuth direction.

## 2.4 SAR Focussing Based on the Fractional Fourier Transform

In A. S. Amein and J. J. Soraghan [2006]; Amein and Soraghan [2007] the Fractional Fourier Transform (FrFT) was applied to the SAR Chirp Scaling Algorithm Raney et al. [1994] to form the Fractional Chirp Scaling Algorithm (FrCSA). In the resulting FrCSA the fractional Fourier transform was used in place of the Fourier transform obtaining a fractional representation of the received signal in both azimuth and range directions. Some good results in terms of enhanced resolution were reported, however this algorithm did not take care of the shift variant problem introduced by the use of the fractional Fourier transform. This approach used the design of a matched filter in the Fractional domain in order to reduce the mismatch due to the approximations introduced in the signal spectrum analysis. However in the FrCSA the shift variant property Bultheel and Martinez [2002] of the FrFT introduced a modulation effect that cannot be removed from the received signal. It means that each echo in the fractional domain exhibits a different modulation due to its delay and thus a mismatch results when performing the matched filtering in the FrCSA.

### 2.4.1 Fractional Fourier Transform

A Fourier transformation (FT) maps a one-dimensional time signal $x(t)$ into a one-dimensional frequency function $X(f)$, the signal spectrum. The Fourier transform operator can be visualized as a change in representation of the signal corresponding to a counter clockwise rotation of the axis by an angle $\pi/2$. Although the Fourier transform provides the spectral content of the signal, it fails to indicate the time location of the spectral components, which is of great importance when non-stationary or time-variant signals are considered. In order to describe and analyse such signals, time-frequency representations (TFRs) are used. A TFR maps a one-dimensional time signal into a two-dimensional function of time and frequency. The fractional Fourier transform (FrFT) which belongs to the class of linear TFRs was introduced by Namias in 1980 Namias [1980], then rediscovered in optics Alieva et al. [1994]; D. Mendlovic and H.M. Ozaktas [1993]; Mendlovic and Ozaktas [1993]; Ozaktas et al. [2001] and introduced to the signal processing community by Almeida in 1994 Almeida [1994]. The fractional Fourier transform, which is a generalization of the ordinary Fourier transform, can be considered as a rotation by an arbitrary angle in the time-frequency plane or a decomposition of the signal in terms of chirps. It also serves as an orthonormal signal representation for chirp signals. The fractional Fourier transform is also called rotational Fourier transform or angular Fourier transform Kutay et al. [1997]. The fractional Fourier transform is computed using the angle of rotation in the time-frequency plane as the fractional power of the ordinary Fourier transform. Letting $x(u)$ be an arbitrary signal, its $a^{th}$-order FrFT is defined as Ozaktas et al. [2001]:

$$\mathbf{X}_a(u) = \int K_a(u, u')x(u')du' \tag{2.1}$$

where $a$ is the fractional transformation order (corresponding to a rotation angle $\theta = a\frac{\pi}{2}$ with $a \in \mathcal{R}$) and $K_a(u, u')$ is the FrFT kernel and is defined as Ozaktas et al. [2001]:

$$K_a(u,u') = \begin{cases} A_0 \exp\{j\pi[(u^2+u'^2)\cot\theta - 2uu'\csc\theta]\} \\ \text{if } \theta \text{ is not a multiple of } \pi \\ \delta(u-u') \text{ if } \theta \text{ is a multiple of } 2\pi \\ \delta(u+u') \text{ if } \theta+\pi \text{ is a multiple of } 2\pi \end{cases} \tag{2.2}$$

where $A_0 = \frac{e^{j\frac{\theta}{2}}}{\sqrt{j\sin\theta}}$

Equation (2.2) shows that for angles that are not multiples of $\pi$, the computation of the FrFT corresponds to the following steps:

1-A product by a chirp;

2-A Fourier transform (scaled by $\csc\theta$);

3-Another product by a chirp;

4-A product by a complex amplitude factor.

In summary, the FrFT is a linear transform, continuous in the angle $\theta$, which satisfies the basic conditions for it to be meaningful as a rotation in the time-frequency plane. The fractional Fourier transform is able to process linear chirp signals better than the ordinary Fourier transform Ozaktas et al. [2001]. This is because a linear chirp signal forms a particular diagonal line in the time-frequency plane, and therefore, there exists an order of transformation in which such signals become compact. Chirp signals are not compact in the time or frequency domain. Thus the signal can be easily extracted in an appropriate (or optimum) fractional Fourier domain whereas in many cases it is not possible to separate the signal and noise in the spatial or frequency domain Borden [2000].

The general linear chirp formula is given as, $\exp j2\pi(at^2+bt+c)$, where $k$ is the chirp rate parameter. The matching process can be described using a geometrical representation through a plot of the instantaneous frequency of the signal, $\phi'(t) = 2at+b$, as shown in Figure 2.4. The optimum transformation angle required to match the chirp rate $a$ is defined as Capus and Brown [2003]:

$$\theta_{opt} = -\frac{2}{\pi}\tan^{-1}\left(\frac{1}{2a}\right) \tag{2.3}$$

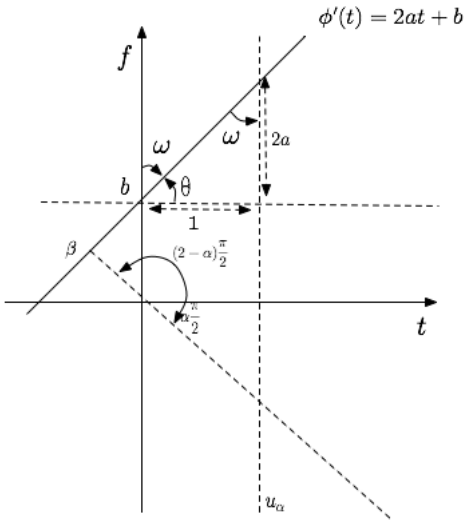


Figure 2.4: Geometrical representation of the fractional space

For a time-frequency discretized signal then 2.3 becomes:

$$\theta_{opt} = -\tan^{-1}\left(\frac{F_s^2/N}{2k}\right) \tag{2.4}$$

where $F_s$ is the sampling frequency and the number of samples is represented by $N$. Figure 2.5-a shows the time domain plot of a linear chirp with duration of 1 second and chirp rate of 20 $[1/s^2]$ sampled at 400 Hz. Figure 2.5-b shown the magnitude of the FrFT of the linear chirp for a range of orders from -1 to 1. It is observed from Figure 2.5-b that the degree of compactness on the FrFT varies with the order. The most compact output occurs for $a = -0.9365$, in agreement with the value computed from (2.4). The magnitude of the FrFT with optimum order for the linear chirp is shown in Figure 2.5-c.

### 2.4.2 Fractional CSA

The Fractional CSA was the first attempt to use the advantages of the FrFT to focus monostatic SAR data A. S. Amein and J. J. Soraghan [2006]; Amein and Soraghan [2007]. The algorithm derives directly from the CSA and is described by the block diagram in Figure 2.6. This algorithm involves the development of a model for transformation optimization in order to obtain the proper rotation angle (required for the

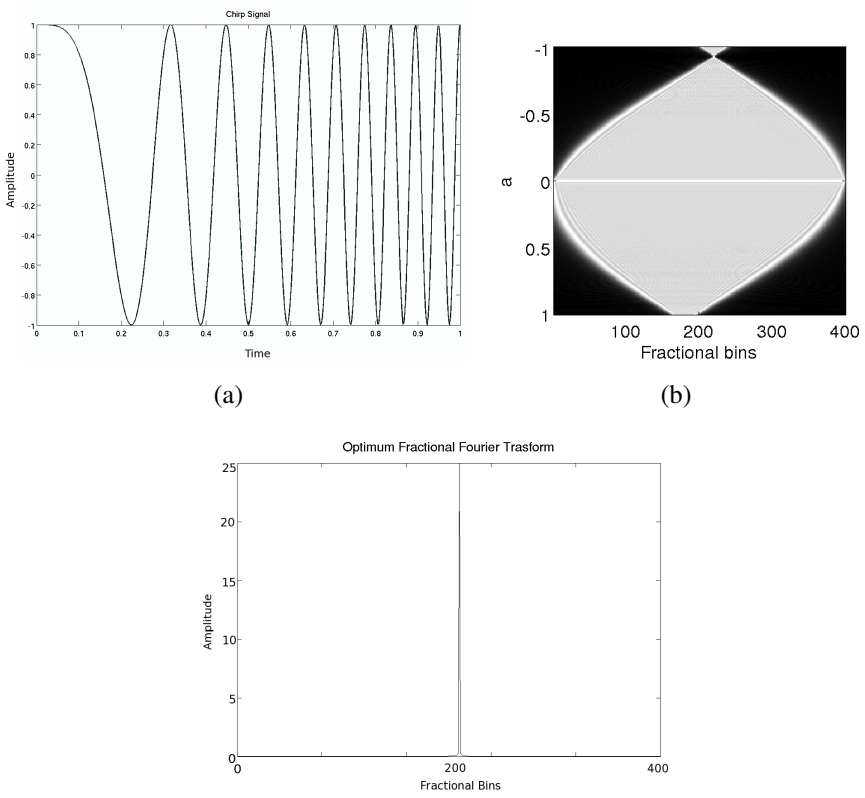


Figure 2.5: (a) Chirp signal, (b) the FrFT for different values of $a$ (c) the optimum fractional Fourier Transform

received chirped signal and all reference signals used in the algorithm). The algorithm uses a local optimization procedure (LOP) that investigates all possible rotation angles and selects the optimum value that is stored and used throughout the algorithm. The resulting FrCSA replaced all the FFTs modules in the conventional CSA with FrFTs, as illustrated in Figure 2.6. One of the most important steps in the FrFT computation is in range transformation processing and its fractional correlator-based range matched filter. It is indeed this new module that gives the FrCSA its improvement to the FFT-based CSA in handling signals, particularly at the far end of the scene.

To obtain the SAR focused image the FrCSA performs the following steps:

1. **Transformation optimization**, the idea of the transformation optimization operation is that the FrFT parameter (or the angle of rotation ) is used to tune the transform to provide an optimal response to a given linear chirp signal. When the axis rotation is matched to the chirp rate of the signal, the magnitude response reaches its maximum. This enables the FrCSA to adapt itself for any sudden change or severe non-linearity in

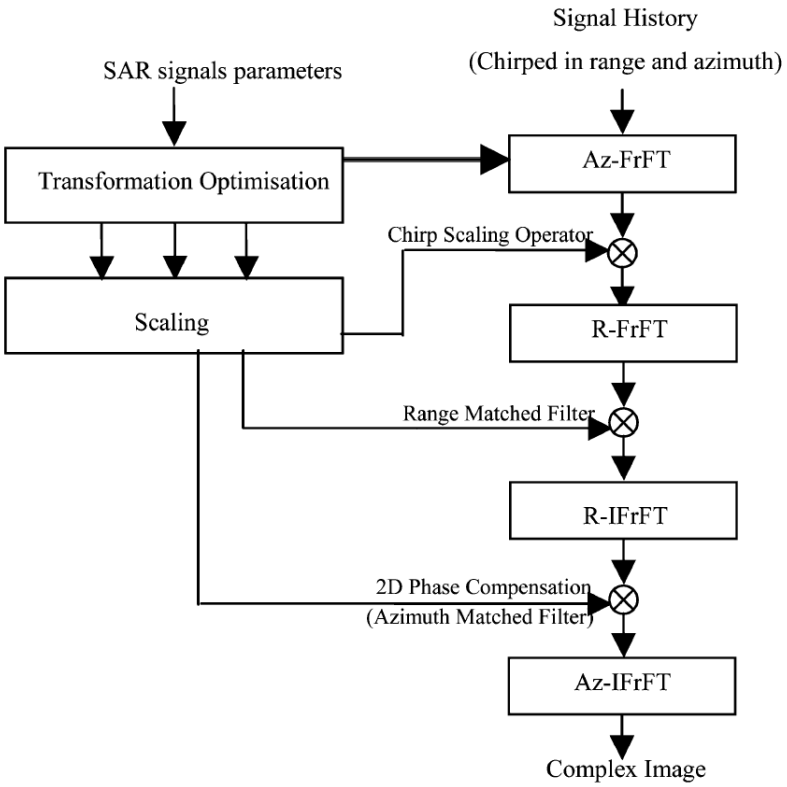


Figure 2.6: Fractional Chirp Scaling SAR processing algorithm

the flight path as it will alter the required appropriate orders of transformations for each range bin thus tuning the transformation for optimal response. The same, of course, is done for range-FrFT.

2. **Azimuth Fractional Fourier Transform**, the first FrCSA operation computes the azimuth FrFT of the signal history, transforming the data into the fractional azimuth-frequency/range-time domain. The CSA/FrCSA equalizes range curvature in the azimuth -frequency (fractional frequency) domain rather than azimuth-position (data collection) domain. In the azimuth-position domain, range curvature is a function of both the broadside range and azimuth coordinates of a scatterer. In the azimuth-frequency domain, however, range curvature does not depend on the azimuth coordinate of a scatterer.

3. **Chirp Scaling Operation**, the second step of the FrCSA procedure performs the chirp-scaling operation described by Papoulis A.Papoulis [1981], that modifies the generalized range chirp rate. An appropriate choice for it will allow the elimination of

the differential range curvature, i.e., differential range cell migration (RCM).

4. **Range FrFT**, the third step in the FrCSA procedure takes the range FrFT of the range-fractional Frequency signal to obtain the 2D-fractional frequency domain signal.

5. **2-D Matched Filtering**, The fourth step is the 2-D matched filtering. This process multiplies the 2D-fractional frequency domain signal by the conjugate of a 2-D reference function. This matched filtering step removes the common range chirp from the signal to prepare for range compression. The matched filter also removes the remaining constant range curvature bulk RCM that results after the differential range curvature correction in the chirp scaling operation.

6. **Range Inverse FrFT**, the fifth step in the FrCSA is the evaluation of the range inverse FrFT to have the signal back in the range-fractional frequency domain.

7. **2-D phase compensation**, the signal is multiplied by the conjugate of a residual phase function to remove the two remaining range-dependent phase terms.

8. **Inverse azimuth FrFT**, a 1-D inverse FrFT compresses the resulting signal in azimuth obtaining the final image.

## 2.5 Bistatic SAR frequency domain focussing algorithms

Bistatic SAR operates with a separate transmitter and receiver introducing new characteristics compared to traditional monostatic SAR systems Cherniakov [2008]. Some of the advantages of the bistatic configuration include i) the reduction of vulnerability of the system in military applications with the ability of having the transmitter located at save distances from a hostile area ii) the capability for the bistatic system to be employed for imaging in the flight direction or backwards in flight assistance systems iii) reduction of costs iv) measurement of the bistatic clutter characteristic and v) the reduction of the dihedral and polyhedral effects in urban areas improving the images quality. However the bistatic flight configuration poses two critical technological challenges. The first involves synchronization of the transmitter and the receiver both in space and time. Good solutions for this issue were developed in C.Gierull

et al. [2006] Krieger and Marwan [2006]. The second critical challenge of the bistatic SAR configuration is the requirement for slant range function approximation which is significantly different from the monostatic case. The bistatic slant range function is characterized by the sum of two hyperbolas Cherniakov [2008] rather than a single hyperbola in the monostatic case. This double squared root function makes the derivation of a signal spectrum model for focussing algorithms in the frequency domain much more challenging than in the monostatic case. The simplest configuration is when both transmitter and receiver have the same velocity and parallel flight paths, while a more complicated configuration exists when the platforms have different velocities and non parallel flight paths. Figure 2.7 illustrates an example of a bistatic configuration that comprises separate transmitter and receiver where it is assumed that the transmitter and receiver platforms have different trajectories and velocities.

As in the monostatic case the area to be imaged is a collection of point scatterers

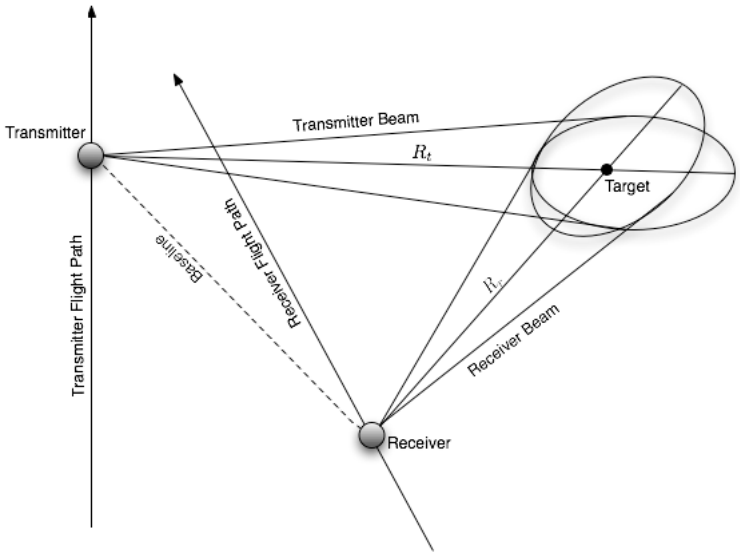


Figure 2.7: Acquisition geometry for bistatic SAR

Cumming and Wong [2005]. This implies that it is sufficient to analyse the scene using the response of an arbitrary point scatterer and then consider the superposition of the echoes to obtain the focused image. Under the assumption that the platforms generally fly with constant velocities and in a linear path, the instantaneous slant range,

$R(\eta)$, may be written as:

$$R(\eta) = \sqrt{V_T^2\eta^2 + R_{Tcen} - 2V_T\eta R_{Tcen} sin\theta_{sqT}} + \sqrt{V_R^2\eta^2 + R_{Rcen} - 2V_R\eta R_{Rcen} sin\theta_{sqR}} \tag{2.5}$$

where $\eta$ is the slow (along track) time, $V_T$ and $V_R$ are the platform velocities, $R_{Tcen}$ and $R_{Rcen}$ are the range distances for $\eta = 0$, $\theta_{sqT}$ and $\theta_{sqR}$ are the squint angles for the transmitter and the receiver respectively. Equation (2.5) converts to the monostatic case when the velocities, positions and flight paths for both the platforms are identical. The monostatic and bistatic slant range functions for 5 point scatterers with the same range but different azimuth position is shown in Figure 2.8-a and 2.8-b respectively. The parameters of the simulated configurations are shown in Table 2.1. In Figure 2.8-a the

Table 2.1: Monostatic and Bistatic simulated configurations. Note: for the monostatic case only the Tx parameters must be considered.

| | |
|---|---|
| *Tx Velocity* | 170 m/s |
| *Rx Velocity* | 100 m/s |
| *Range distance of the Tx from the scene centre at* $\eta = 0$ | 1400 m |
| *Range distance of the Rx from the scene centre at* $\eta = 0$ | 1100 m |
| *Transmitter Squint angle* | 3 deg |
| *Receiver Squint angle* | 2 deg |

hyperbolic shape of the monostatic slant range function can be clearly seen, in Figure 2.8-b the slant range function of the bistatic case is no longer a hyperbola. Instead it is a flat-top hyperbola which changes in shape depending on the position of the scatterer. The minimum of this slant range function is related to the point of stationary phase, hence the stationary points change with the slant range. This is an important aspect to be taken into consideration for the derivation of bistatic point target spectrum making hard the derivation of it in a closed form. In the case of a transmitted linear frequency modulated chirp signal the received bistatic signal model an be written as:

$$s(\tau,\eta) = A_0 w_r\left(\tau - \frac{R(\eta)}{c}\right) w_{az}(\eta) \exp\left\{-j\frac{2\pi f_0 R(\eta)}{c} + j\pi K_r\left[\tau - \frac{R(\eta)}{c}\right]^2\right\} \tag{2.6}$$

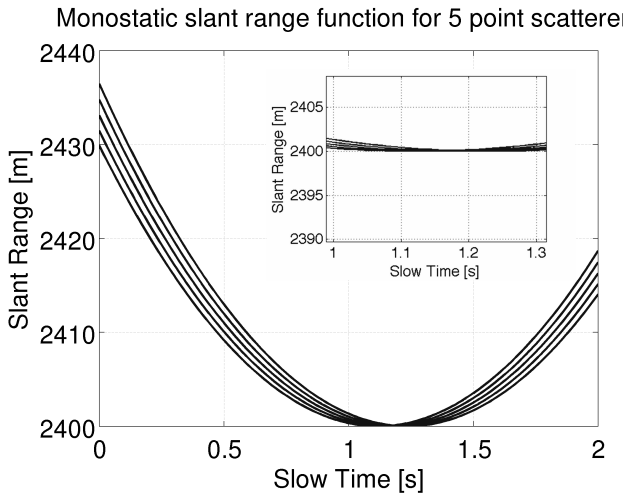


(a) Monostatic case

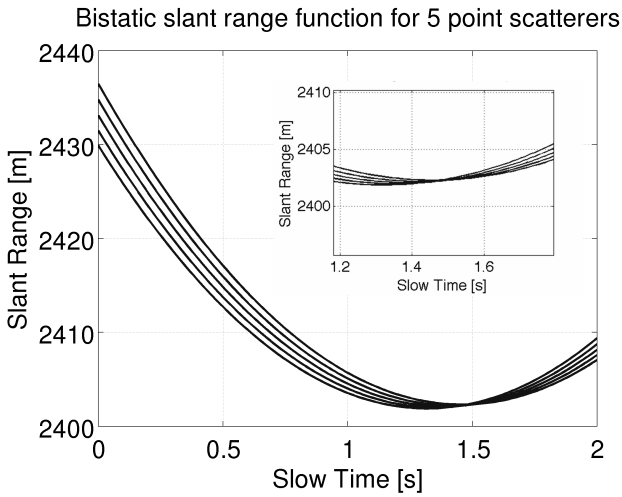


(b) Bistatic case

Figure 2.8: Slant range for different point scatterers for the monostatic and the bistatic case.

where $\tau$ is the fast time, $A_0$ is the complex backscatterer coefficient, $f_0$ is the carrier frequency $K_r$ is the range chirp rate, $w_r(.)$ is the range envelope and $w_{az}(.)$ is the composite antenna pattern of the transmitter and receiver. The only differences between the expression of the signal model in the bistatic and monostatic case are the slant range function and the composite antenna footprint.

In order to achieve processing efficiency also for the Bistatic SAR case the use of frequency domain algorithms is recommended. However it has been shown from several authors Bamler and Boerner [2005]; Loffeld et al. [2003]; Neo [2007] that the bistatic case cannot be focused by simply assuming an equivalent monostatic in the middle of

the baseline, specially for configuration with an appreciable baseline separation. Due to the existence of a double squared root function in the range equation of the bistatic case it is difficult to obtain a simple analytical solution that expresses the bistatic point target spectrum. It means that without an analytical expression of the bistatic point target spectrum equivalent bistatic algorithms are difficult to derive. Thus the necessity to design new bistatic focussing algorithms to cope with the peculiarities of this acquisition geometry.

Frequency domain focussing algorithms for bistatic SAR can be divided in three families:

- Algorithms based on numerical methods to solve the double square root function;
- Algorithms that use a pre-processing stage to transform the bistatic data to an equivalent monostatic data, making then possible the application of traditional monostatic focussing algorithms;
- Algorithms that use an approximate point target spectrum and use this analytical formulation to derive the steps required to perform the focussing of the image.

### 2.5.1 Numerical Methods

In the numerical methods the double square root is solved numerically, the first approach has been to exploit the $\Omega - K$ algorithm Cumming and Wong [2005], this algorithm processes the raw signal in the 2-D frequency domain. However the function to be exploited in the original algorithm is an analytical function, in the bistatic case it is not available then in Bamler and Boerner [2005] was proposed a focussing algorithm that replaces the analytical transfer function with a numerical one. The main limitation of this approach is that the numerical version of the transfer function is available for the azimuth-invariant case while the computational cost increases when the bistatic degree of the data increases. In addition, performances, accuracies and limitation of the algorithm are strongly dependent on the geometry and cannot be predicted, while these aspects could be evaluated with an analytical method.

### 2.5.2 Pre-processing methods

The aim of pre-processing methods is to convert bistatic data in monostatic data. The simplest approach to converting a bistatic configuration to a monostatic equivalent is to replace the two platforms with a monostatic platform right in the middle of the baseline. Despite its simplicity, this method is inadequate in scenarios where there is an appreciable baseline separation. The use of hyperbolic range functions with a modified velocity is another technique that can be used. Such techniques have been used to accommodate orbital curvature in monostatic configurations through the use of an effective radar velocity. These methods are valid for satellite-based cases where there is usually no appreciable squint. In addition pre-processing techniques have been shown to be suitable for bistatic configurations where the baseline is fixed so that the azimuth invariance property holds. The most interesting and accurate pre-processing method uses the so-called Rocca's "smile operator" and was introduced D'Aria et al. [2004]. It is applicable in cases where both platforms are travelling on the same flight path with a constant baseline. The Dip MoveOut (DMO) method introduced in D'Aria et al. [2004] transforms bistatic acquisitions into monostatic ones. This processing technique derives from the field of of seismic reconstruction, where a typical source is accompanied by thousands of geophone receivers. However, this method has a restrictive geometric configuration, i.e., it can only focus the bistatic configuration where both transmitter and receiver are flying in along the same track with the same velocity. Thus, limiting its usage.

### 2.5.3 Analytical Point Target Spectrum

The derivation of an analytical PTS for the bistatic SAR case is still an open problem and has seen different authors working to find a close and *exact* form of the bistatic PTS. A point target spectrum known as the Loffeld's Bistatic Formula (LBF) was derived in Loffeld et al. [2003]. This spectrum was used to derive a few bistatic algorithms. The accuracy of these algorithms is limited by the accuracy of the analytical spectrum. The LBF is characterized by two phase therms: a quasi-monostatic and a bistatic phase terms. This aspect suggests a possible two-step focussing approach: the

removal of the bistatic deformation followed by the application of a quasi-monostatic focussing step. In this way the use of the LBF can be seen as a pre-processing technique.

Two other remarkable approaches have been developed obtaining excellent results Neo et al. [2007]; Wang et al. [2011]. In Neo [2007]; Neo et al. [2007] the bistatic PTS has been derived using the method of series reversion while in Wang et al. [2011] the two dimensional Principle of Stationary Phase (PSP) has been applied in order to derive a more accurate and robust spectrum model. These two approaches will be analysed in details in the next sections since they are the basis of the novelties developed for the bistatic focussing aspect of our work (Chapter 5).

#### 2.5.3.1 Method of Series Reversion

In the bistatic PTS obtained using the Method of Series Reversion Morse and Feshbach [1953]; Neo [2007] the starting point is the range compressed signal:

$$s_{rc}(\tau,\eta) = \rho\left(\tau - \frac{\hat{R}(\eta)}{c}\right) w_{az}(\eta)\exp\left\{-j\frac{2\pi f_0 \hat{R}(\eta)}{c}\right\} \tag{2.7}$$

where $\hat{R}(\eta) = R_{Tcen} + R_{Rcen} + k_1\eta + k_2\eta^2 + k_3\eta^3 + k_4\eta^4\ldots$ is the Taylor series expansion of the bistatic slant range function, and $k_i$ are the coefficients of the Taylor series. $R_{Tcen}$ and $R_{Rcen}$ are the range from the transmitter/receiver to an arbitrary point target at azimuth time $\eta = 0$. From this signal, in order to apply the MSR the Linear Range Cell Migration (LRCM) and the linear phase term of $\hat{R}(\eta)$ must be removed, then the signal becomes:

$$s_1(\tau,\eta) = \rho\left(\tau - \frac{R_1(\eta)}{c}\right) w_{az}(\eta)\exp\left\{-j\frac{2\pi R_1(\eta)}{\lambda}\right\} \tag{2.8}$$

where $R_1(\eta)$ is the slant range approximation obtained using the Taylor series expansion, without the linear term:

$$R_1(\eta) = R_{cen} + k_2\eta^2 + k_3\eta^3 + k_4\eta^4\ldots \tag{2.9}$$

with $R_{cen} = R_{Tcen} + R_{Rcen}$.

The coefficients $k_i$ are obtained from:

$$k_i = \frac{1}{i!}\left(\frac{dR_T^i(\eta)}{d\eta^i} + \frac{dR_R^i(\eta)}{d\eta^i}\right)\Bigg|_{\eta=0} \tag{2.10}$$

Applying the range FT to (2.8) produces:

$$S_1(f_\tau, \eta) = W_r(f_\tau) w_{az}(\eta) \exp\left\{-j2\pi \frac{(f_0 + f_\tau)R_1(\eta)}{c}\right\} \tag{2.11}$$

where $W_r(.)$ is the spectral shape of the transmitted pulse and $f_0$ is the center frequency. Next the azimuth Fourier transform is applied and computed employing the method of stationary phase must be used, the phase of the signal is:

$$\frac{d\Phi(\eta)}{d\eta} = 2k_2\eta + 3k_3\eta^2 + 4k_4\eta^3 + \left(-2\pi\frac{f_0 + f_\tau}{c}\right) + 2\pi f_\eta \tag{2.12}$$

where $f_\eta$ is the azimuth frequency. Then applying the method of stationary phase on (2.12) the following relation can be found

$$\left(-\frac{c}{f_0 + f_\tau}\right) f_\eta = 2k_2\eta + 3k_3\eta^2 + 4k_4\eta^3 \tag{2.13}$$

MSR is applied to (2.13) obtaining an expression of $\eta$ in terms of $f_\eta$:

$$\eta(f_\eta) = A_1\left(-\frac{c}{f_0 + f_\tau} f_\eta\right) + A_2\left(-\frac{c}{f_0 + f_\tau} f_\eta\right)^2 + A_3\left(-\frac{c}{f_0 + f_\tau} f_\eta\right)^3 \tag{2.14}$$

where

$$\begin{aligned} A_1 &= \frac{1}{k_2} \\ A_2 &= -\frac{3k_3}{8k_2^3} \\ A_3 &= -\frac{9k_3^2 - 4k_2k_4}{16k_2^5} \end{aligned} \tag{2.15}$$

At this point an expression of the two dimensional spectrum can be obtained

$$S_1(f_\tau, f_\eta) = W_r(f_\tau) W_{az}(f_\eta) \exp\left\{-j2\pi f_\eta \eta(f_\eta)\right\} \exp\left\{-j2\pi \frac{(f_0 + f_\tau) R_1(\eta(f_\eta))}{c}\right\} \tag{2.16}$$

where $W_{az}(.)$ represents the shape of the Doppler spectrum. To obtain the two dimensional point target spectrum the LRCM and the linear phase therm must be reintroduced into $s_1(\tau, \eta)$

$$\begin{aligned} s(\tau, \eta) &= s_1\left(\tau - \frac{k_1 \eta}{c}, \eta\right) \exp\left\{-j2\pi \frac{f_0 k_1}{c} \eta\right\} \\ &= p_r\left(\tau - \frac{R_1(\eta) + k_1 \eta}{c}\right) w_{az}(\eta) \exp\left\{-j2\pi\left(\frac{f_0 R_1(\eta)}{c} + \frac{f_0 k_1 \eta}{c}\right)\right\} \end{aligned} \tag{2.17}$$

to obtain the 2D point target spectrum the skew and shift properties of the FT (2.18) are applied

$$\begin{aligned} & g(\tau, \eta) \leftrightarrow G(f_\tau, f_\eta) \\ & g(\tau, \eta) \exp(-j2\pi f_k \eta) \leftrightarrow G(f_\tau, f_\eta + f_k) \\ & g(\tau - k\eta, \eta) \leftrightarrow G(f_\tau, f_\eta + k f_\tau) \end{aligned} \tag{2.18}$$

so the 2D point target spectrum is:

$$\begin{aligned} S_{2df}(f_\tau, f_\eta) &= S_1\left[f_\tau, f_\eta + (f_0 + f_\tau)\frac{k_1}{c}\right] \\ &= W_r(f_\tau) W_{az}\left(f_\eta (f_0 + f_\tau)\frac{k_1}{c}\right) \exp j\Phi_{2df}(f_\tau, f_\eta) \end{aligned} \tag{2.19}$$

where

$$\begin{aligned} \Phi_{2df}(f_\tau, f_\eta) \approx & -2\pi\left(\frac{f_0 + f_\tau}{c}\right) R_{cen} + 2\pi \frac{c}{4k_2(f_0 + f_\tau)}\left(f_\eta + (f_0 + f_\eta)\frac{k_1}{c}\right)^2 \\ & + 2\pi \frac{c^2 k_3}{8k_2^3 (f_0 + f_\tau)^2}\left(f_\eta + (f_0 + f_\eta)\frac{k_1}{c}\right)^3 \\ & + 2\pi \frac{c^3(9k_3^2 - 4k_2 k_4)}{64 k_2^5 (f_0 + f_\tau)^3}\left(f_\eta + (f_0 + f_\eta)\frac{k_1}{c}\right)^4 \end{aligned} \tag{2.20}$$

Then the phase term in (2.20) is the starting point for bistatic focussing algorithms as the bistatic RDA and NLCSA Neo et al. [2008]; Wong et al. [2008].

#### 2.5.3.2 2-D Principle of Stationary Phase

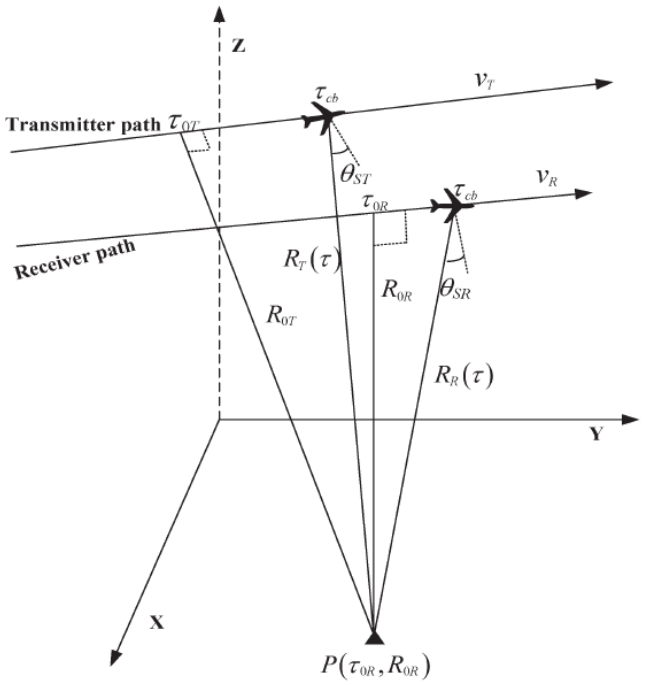


Figure 2.9: Geometry considered in the derivation of the PTS in Wang et al. [2011]

The PTS proposed in Wang et al. [2011] is probably the most accurate and robust PTS able to work in the azimuth variant case. It is derived using the 2-D principle of stationary phase which is first applied in the SAR community. The resulting PTS contains two hyperbolic range-azimuth coupling terms and thus is very similar to the monostatic PTS. It presents the same characteristics of the monostatic PTS besides an additional azimuth scaling therm. This aspect makes it suitable for bistatic SAR processing the wide range of monostatic SAR focussing algorithms. The derivation of the PTS requires more details then those used for the derivation of the PTS using the MSR described in Section 2.5.3.1, for this reason the geometry in Figure 2.9 is introduced. The 3-D coordinate system has the $x-y$ plane defining the surface of the Earth and the $z-$ axis pointing away from the Earth. The starting point for the derivation of the PTS is the received echo from a point target located in $(\tau_{0R}, R_{0R})$

after the demodulation given by

$$g(\tau, t, \tau_{0R}, R_{0R}) = \sigma(\tau_{0R}, R_{0R}) s_l \left( t - \frac{R_R(\tau) + R_T(\tau)}{c} \right) \times \exp\left[ -j2\pi \frac{R_R(\tau) + R_T(\tau)}{\lambda} \right] w(\tau - \tau_{cb}) \tag{2.21}$$

where $\tau_{0R}$ is the zero Doppler time of the receiver; $\tau$ is the slow time; $t$ is the fast time; $R_{0R}$ is the closest slant range from the receiver and the point target $P(\tau_{0R}, R_{0R})$; $\sigma(\tau_{0R}, R_{0R})$ is the reflectivity profile for the point target in $(\tau_{0R}, R_{0R})$; $s_l$ is the transmitted signal; $R_R$ and $R_T$ are the receiver and transmitter slant ranges; $c$ is the speed of light; $\lambda$ is the radar wavelength and $w(\tau - \tau_{cb})$ is the composite azimuth antenna pattern centred on azimuth time $\tau_{cb}$. The composite antenna pattern can be approximated as the multiplication of two rectangular functions: $W_T[(\tau - \tau_{cb})/T_{sc}]W_R[(\tau - \tau_{cb})/T_{sc}]$, where $T_{sc}$ is the composite time of target in azimuth. The instantaneous slant ranges are defined as:

$$\begin{aligned} R_R(\tau) &= \sqrt{R_{0R}^2 + (\tau - \tau_{0R})^2 v_R^2} \\ R_T(\tau) &= \sqrt{R_{0T}^2 + (\tau - \tau_{0T})^2 v_T^2} \end{aligned} \tag{2.22}$$

where $v_T$ and $v_R$ are the transmitter and receiver velocities, $\tau_{0T}$ is the zero Doppler time of the transmitter and $R_{0T}$ is the closest slant range from the transmitter. Performing the 2-D Fourier Transform to (2.21) gives

$$G(f_\tau, f, \tau_{0R}, R_{0R}) = \sigma(\tau_{0R}, R_{0R}) S_l(f) \int w(\tau - \tau_{cb}) \times \exp\left[ -2\pi(f + f_0) \frac{R_R(\tau) + R_T(\tau)}{c} \right] \exp(-j2\pi f_\tau \tau) d\tau \tag{2.23}$$

where $S_l$ is the spectrum of the transmitted signal. In Wang et al. [2011] the limitation of the double square root term in (2.23), which does not allow the direct application of

the PSP, is solved by the use of a Fourier decomposition.

$$
\begin{aligned}
W_R\left[\frac{\tau-\tau_{cb}}{T_{sc}}\right]\exp\left[-2\pi\frac{f+f_0}{c}R_R(\tau)\right] &= \int W_R\left[\frac{\tilde{\tau}_R(f_{\tau R})-\tau_{cb}}{T_{sc}}\right] \\
&\times \exp[-j\Phi_R(f_{\tau R},f)]\exp[j2\pi f_{\tau R}\tau]df_{\tau R} \\
W_T\left[\frac{\tau-\tau_{cb}}{T_{sc}}\right]\exp\left[-2\pi\frac{f+f_0}{c}R_T(\tau)\right] &= \int W_T\left[\frac{\tilde{\tau}_T(f_{\tau T})-\tau_{cb}}{T_{sc}}\right] \\
&\times \exp[-j\Phi_T(f_{\tau T},f)]\exp[j2\pi f_{\tau T}\tau]df_{\tau T}
\end{aligned}
\tag{2.24}
$$

where $f_{\tau R}$ and $f_{\tau T}$ are the two azimuth frequency variables and represents the contributions of the range equations of the receiver and transmitter to the instantaneous Doppler frequency $f_\tau = f_{\tau R} + f_{\tau T}$. $\Phi_R$ and $\Phi_T$ are defined as

$$
\begin{aligned}
\Phi_R(f_{\tau R}) &= 2\pi f_{\tau R}\tau_{0R} + 2\pi\frac{R_{0R}}{c}\sqrt{(f+f_0)^2-\left(\frac{cf_{\tau R}}{v_R}\right)^2} \\
\Phi_T(f_{\tau T}) &= 2\pi f_{\tau T}\tau_{0T} + 2\pi\frac{R_{0T}}{c}\sqrt{(f+f_0)^2-\left(\frac{cf_{\tau T}}{v_T}\right)^2}
\end{aligned}
\tag{2.25}
$$

$\tilde{\tau}_R(f_{\tau R})$ and $\tilde{\tau}_T(f_{\tau T})$ are the individual time-Doppler correspondences of the receiver and transmitter,

$$
\begin{aligned}
\tilde{\tau}_R(f_{\tau R}) &= \tau_{0R} - \frac{cR_{0R}}{v_R^2}\frac{f_{\tau R}}{\sqrt{(f+f_0)^2-\left(\frac{cf_{\tau R}}{v_R}\right)^2}} \\
\tilde{\tau}_T(f_{\tau T}) &= \tau_{0T} - \frac{cR_{0T}}{v_T^2}\frac{f_{\tau T}}{\sqrt{(f+f_0)^2-\left(\frac{cf_{\tau T}}{v_T}\right)^2}}
\end{aligned}
\tag{2.26}
$$

Substituting (2.24) and (2.26) into (2.23) yields:

$$
\begin{aligned}
G(f_\tau,f,\tau_{0R},R_{0R}) =& \sigma(\tau_{0R},R_{0R})S_l(f)\int\exp(-j2\pi f_\tau\tau) \\
&\times\left[\int\int W_R\left[\frac{f_{\tau R}-f_{DcR}}{K_{aR}T_{sc}}\right]W_T\left[\frac{f_{\tau T}-f_{DcT}}{K_{aT}T_{sc}}\right]\right. \\
&\times\exp(j2\pi f_\tau\tau)\exp\{-j[\Phi_R(f_{\tau_R},f)+\Phi_T(f_{\tau T},f)]\} \\
&\left.\times df_{\tau R}df_{\tau T}\right]d\tau
\end{aligned}
\tag{2.27}
$$

In (2.27) $f_{DcR}$ and $f_{DcT}$ are the Doppler centroids while $K_{aR}$ and $K_{aT}$ are the azimuth modulation rate defined as:

$$\begin{aligned} f_{DcR} &= \frac{v_R \sin\theta_{SR}}{c/(f+f_0)} \qquad f_{DcT} = \frac{v_T \sin\theta_{ST}}{c/(f+f_0)} \\ K_{aR} &= \frac{v_R^2 \cos^3\theta_{SR}}{\lambda R_{0R}} \qquad K_{aT} = \frac{v_T^2 \cos^3\theta_{ST}}{\lambda R_{0T}} \end{aligned} \tag{2.28}$$

where $\theta_{SR}$ and $\theta_{ST}$ are the squint angles of the receiver and the transmitter at the composite beam center crossing time. To (2.27) the 2D PSP can be applied letting the first partial derivative of the phase of (2.27) be zero and obtaining the points $f_{\tau R}$ and $f_{\tau T}$ of stationary phase leading to the bistatic PTS.

$$\begin{aligned} \Psi_B(f_\tau, f, R_{0R}) =& \pi\frac{f^2}{K_r} + 2\pi(f_{\tau R}\tau_{0R} + f_{\tau T}\tau_{0T}) \\ &+ 2\pi\left[\frac{R_{0R}}{c}\sqrt{(f+f_0)^2 - \left(\frac{cf_{\tau R}}{v_R}\right)^2}\right. \\ &\left. + \frac{R_{0T}}{c}\sqrt{(f+f_0)^2 - \left(\frac{cf_{\tau T}}{v_T}\right)^2}\right] \end{aligned} \tag{2.29}$$

where $K_r$ is the modulation rate of the transmitted frequency modulated signal. The expression in (2.29) can be additionally developed using the geometric image transformation Franceschetti and Lanari [1999] obtaining

$$\begin{aligned} \Psi_B(f_\tau, f, R_{0R}) =& \pi\beta_a\tau_{0R}f_\tau + 2\pi(p_{01} + p_{11}R_{0R})k_T f_\tau + \\ & 2\pi\left[\frac{R_{0R}}{c}F_R + \frac{R_{0T}}{c}F_T\right] + \bar{\Phi}_{RCM}(f) + \Phi_{Res}(\tau_{0R}, R_{0R}) \end{aligned} \tag{2.30}$$

where the coefficients $p_{ij}$ are obtained using the geometrical image transformation of $\tau_{0T}$ to obtain it as a function of $\tau_{0R}$ and $R_{0R}$. $\beta_a$ is the scaling factor in the azimuth domain defined as $\beta_a = k_R + p_{12}k_T$ , with $k_R = K_{aR}/(K_{aR} + K_{aT})$ and $k_T = K_{aT}/(K_{aR} + K_{aT})$ denoting the receiver and transmitter azimuth modulation rate. $\bar{\Phi}_{RCM}(f)$ and $\Phi_{Res}(\tau_{0R}, R_{0R})$ are a component of the RCM and the residual phase.

The expression of $\bar{\Phi}_{RCM}(f)$ is:

$$\bar{\Phi}_{RCM}(f) = 2\pi\frac{R_{0T}}{c}\frac{\mu_{T1}\mu_{T2}}{D_T}f + 2\pi\frac{R_{0R}}{c}\frac{\mu_{R1}\mu_{R2}}{D_R}f \tag{2.31}$$

while that of $\Phi_{Res}(\tau_{0R}, R_{0R})$ is

$$\begin{aligned}\Phi_{Res}(\tau_{0R}, R_{0R}) = &- 2\pi\frac{(k_T v_R \sin\theta_{SR} - k_R v_T \sin\theta_{ST})}{\lambda} \\ &\times (p_{10} + p_{11}R_{0R} + p_{12}\tau_{0R}) \\ &+ 2\pi\frac{(k_T v_R \sin\theta_{SR} - k_R v_T \sin\theta_{ST})}{\lambda}\tau_{0R}\end{aligned} \tag{2.32}$$

where :

$$\begin{aligned}D_R =& \sqrt{1-\mu_{R1}^2} \qquad D_T = \sqrt{1-\mu_{T1}^2} \\ \mu_c =& \frac{k_T v_R sin\theta_{SR} - k_R v_T sin\theta_{ST}}{\lambda} \\ &\times (p_{01} + p_{11}R_{0R} + p_{12}\tau_{0R}) \\ &+ 2\pi\frac{k_T v_R sin\theta_{SR} - k_R v_T sin\theta_{ST}}{\lambda} \\ \mu_{R1} =& \frac{\lambda}{v_R}(k_R f_\tau + \mu_c) \qquad \mu_{R2} = \frac{\lambda}{v_R}\mu_c \\ \mu_{T1} =& \frac{\lambda}{v_T}(k_T f_\tau - \mu_c) \qquad \mu_{T2} = -\frac{\lambda}{v_T}\mu_c\end{aligned} \tag{2.33}$$

To represent the PTS in a series of power of the range frequency and separate the different components of the range-azimuth coupling a Taylor series approximation of the hyperbolic frequencies coupling variables is introduced.

$$\begin{aligned}F_R(f) &= \sqrt{(f+f_0)^2 - \left(\frac{cf_{\tau_R}}{v_R}\right)^2} \\ F_T(f) &= \sqrt{(f+f_0)^2 - \left(\frac{cf_{\tau_T}}{v_T}\right)^2}\end{aligned} \tag{2.34}$$

As stated before the expression of $F_R$ and $F_T$ must be expanded in a power series to separate the different contributions. In Wang et al. [2011] the Taylor series is used on

(2.34) yielding:

$$F_R(f) \approx D_R f_0 + \frac{(1-\mu_{R1}\mu_{R2})}{D_R} f - \frac{(\mu_{R1}-\mu_{R2})^2}{2 f_0 D_R^3} f^2$$
$$F_T(f) \approx D_T f_0 + \frac{(1-\mu_{T1}\mu_{T2})}{D_T} f - \frac{(\mu_{T1}-\mu_{T2})^2}{2 f_0 D_T^3} f^2 \tag{2.35}$$

Then substituting (2.35) in (2.30) it is possible to obtain a form of the PTS useful to develop focussing algorithms.

$$\Psi_B(f_\tau, f, R_{0R}) = \Phi_{RC}(f_\tau, f) + \Phi_{RCM}(f_\tau, f, R_{0R}) + \Phi_{AC}(f_\tau, R_{0R}) + \Phi_{AS}(f_\tau) \tag{2.36}$$

with:

$$\Phi_{RC}(f_\tau, f) \approx \pi \frac{f^2}{K_r} - \pi \frac{f^2}{K_{SRC}} \tag{2.37}$$

$$\Phi_{RCM}(f_\tau, f, R_{0R}) = \frac{2\pi}{c}\left[\frac{R_{0R}}{D_R} + \frac{R_{0T}}{D_T}\right] f \tag{2.38}$$

$$\Phi_{AC}(f_\tau, R_{0R}) = 2\pi(p_{01} + p_{11} R_{0R}) k_T f_\tau + \frac{2\pi}{\lambda}(R_{0R} D_R + R_{0T} D_T) \tag{2.39}$$

$$\Phi_{AS}(f_\tau) = 2\pi \beta_a \tau_{0R} f_\tau \tag{2.40}$$

$$\frac{1}{K_{SRC}} = \left[R_{RR}\frac{(\mu_{R1}-\mu_{R2})^2}{c f_0 D_R^3} + R_{RT}\frac{(\mu_{T1}-\mu_{T2})^2}{c f_0 D_T^3}\right] \tag{2.41}$$

$R_{RR}$ and $R_{RT}$ are the reference slant range of the transmitter and the receiver respectively.

The spectrum in (2.30) is the main result in Wang et al. [2011] that resulted to be accurate and was tested with real data.

## 2.6 Conclusion

In this chapter the basics of SAR imaging have been introduced. The Range Doppler Algorithm and the Chirp Scaling Algorithm have been described in detail. In addition the Fractional Fourier Transform and the FrCSA algorithm have been described. These three algorithms are important since they are exploited in the derivation of the Fractional RDA and Enhanced Fractional CSA (Chapter 4).

The focussing problem in the bistatic SAR case has been described and the different approaches for the development of an accurate focussing strategy have been analysed. In particular two models for the bistatic point target spectrum have been discussed in detail: the BPTS based on the Method of Series Reversion and the BPTS derived using the 2D Principle of Stationary Phase. These two models are important for the understanding of this thesis since their improvement obtained using the Chebyshev approximation is presented in Chapter 5.

# Chapter 3

# The Micro-Doppler Effect

## 3.1 Introduction

The micro-Doppler effect was originally introduced in coherent *laser* radar systems. Laser detection and ranging systems (LADAR) transmit an electromagnetic wave at optical frequencies and receive the reflected light wave from an object to measure its range, velocity and other properties. This kind of system has great sensitivity to phase changes thanks to the coherence between the returned signal and the transmitted one. As a consequence, jointly with the high working frequency, very small vibrations of the object cause high Doppler shifts, thus easy to be detected. Analysing this phenomenon in microwave radar systems the nature of the detectable micro motion changes due to the longer wavelength used by the system. However the term *micro-motion* relates to the additional motion present within a target different from its bulk body motion. For example rotating propellers, helicopter rotor blades, walking humans.

*Micro-motions* can contribute with frequency modulations around the main Doppler shift that are commonly referred to as micro-Doppler (m-D) modulations. Chen Chen [2011]; Chen et al. [2006] modelled the radar m-D phenomenon and simulated m-D signatures for various targets, such as rotating cylinders, vibrating scatterers and personnel targets. The authors also showed that an effective tool in extracting the m-D signature is the time-frequency analysis of the received signal, leading to additional information on the target that can be used for classification and recognition. Micro-Doppler can be regarded as a unique signature of the target that provides addi-

tional information about the target that is complementary to existing methods for target recognition. Specific applications include the recognition of space, air, and ground targets. For example, the m-D effect can be used to identify specific types of vehicles and determine their movement and the speed of their engines. Vibrations generated by a vehicle engine can be detected by radar signals returned from the surface of the vehicle. For example, from m-D modulations in the engine vibration signal, one can distinguish whether it is a gas turbine engine of a tank or the diesel engine of a bus Chen [2011]. Another application is the use of m-D signature for human identification making possible the identification of humans on different weather or light conditions. In particular, specific components of m-D gait signature can be related to parts of the body for identification purposes Tahmoush and Silvious [2009]. Recently effective signature extraction techniques have been developed and tested on real data Bjorklund et al. [2012]; Molchanov et al. [2011a, 2012, 2010, 2011b]; Smith et al. [2010a, 2006, 2010b] providing features leading to classification results with a high level of confidence. These results could probably be improved if a multistatic m-D signature is used Smith et al. [2008] where the self occlusion problem of the target is avoided.

In this chapter, we review the basics of radar micro-Doppler introducing the formalism and the study of canonical cases. The chapter then focusses on the review of recent advances in radar based m-D analysis from radar imaging systems : Synthetic Aperture Radar and Inverse Synthetic Aperture Radar. The understanding of the analysis of micro-Doppler from SAR systems is important since in Chapter 6 the micro-Doppler effect from Bistatic SAR is modelled and analysed.

## 3.2 Micro-Doppler Effect in Radar

The mathematics of the micro-Doppler effect from radar can be derived from introducing micro-motion to the conventional Doppler analysis. In this section the basics of the micro-Doppler effect for the case of vibrating and rotating point targets are introduced. The understanding of these cases are fundamental for the understanding and the derivation of the micro-Doppler effect in more complex and realistic cases. In Figure 3.1 the geometry used to analyse the micro-Doppler induced by a vibrating target is shown

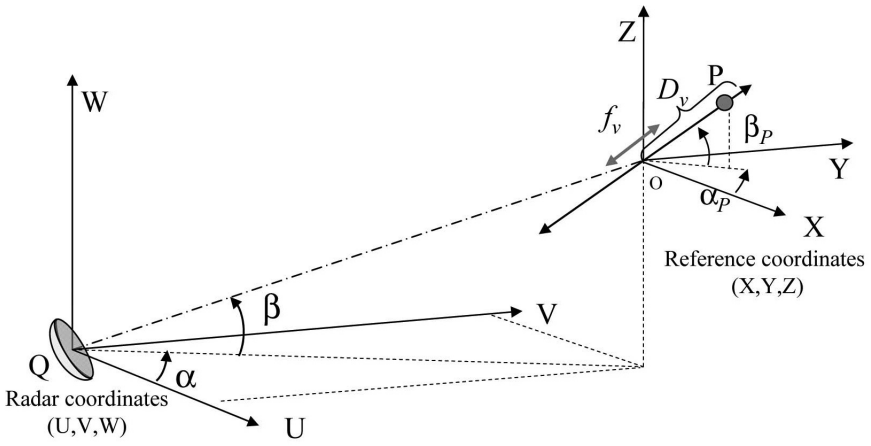


Figure 3.1: Geometry for the radar and a vibrating point target

Chen [2011]. The target located in $P$ vibrates with frequency $f_v$ and displacement $D_v$, thus having a displacement function of the kind $D(t) = D_v \sin 2\pi f_v t cos\beta \cos \alpha_p$ (assuming $\alpha = 0$ and $\beta_p = 0$) Chen [2011]. Calling $R_0$, the distance between the radar and the target initial position of the target $O$. Then the range function varies with time due to the target micro-motion $R(t) = R_0 + D(t)$. The radar received signal becomes

$$s(t) = \rho \exp\left\{ j \left[ 2\pi f_0 t + 4\pi \frac{R(t)}{\lambda} \right] \right\} = \rho \exp\left\{ j[2\pi f_0 t + \Phi(t)] \right\} \tag{3.1}$$

where $\rho$ is the backscattering coefficient $f_0$ is the carrier frequency, and $\lambda$ is the carrier wavelength. Substituting the $R(t)$ in (3.1) the received signal can be expressed as:

$$s(t) = \rho \exp\left\{ j \frac{4\pi R_0}{\lambda} \right\} \exp\{ j2\pi f_0 t + D_v \sin(w_v t) cos\beta \cos \alpha_p 4\pi/\lambda \} \tag{3.2}$$

where $w_v = 2\pi f_v$. From (3.2), the derivative of the second phase term leads to the expression of the micro-Doppler shift.

$$f_{mD} = \frac{w_v D_v}{\pi \lambda} \cos \beta \cos \alpha_p cos(w_v t) \tag{3.3}$$

In Figure 3.2-a and -b are shown the results simulated for a 10 GHz radar with a PRF of 2000 Hz. Given $D_v = 0.01$ m, $f_v = 2$ Hz, $\alpha_p = 30°$ , $\beta_p = 30°$ , and the center of the vibration at ($U = 1000$ m, $V = 5000$ m, $W = 5000$ m), the theoretical result, Figure 3.2-a, of the micro-Doppler modulation is identical to the simulated results

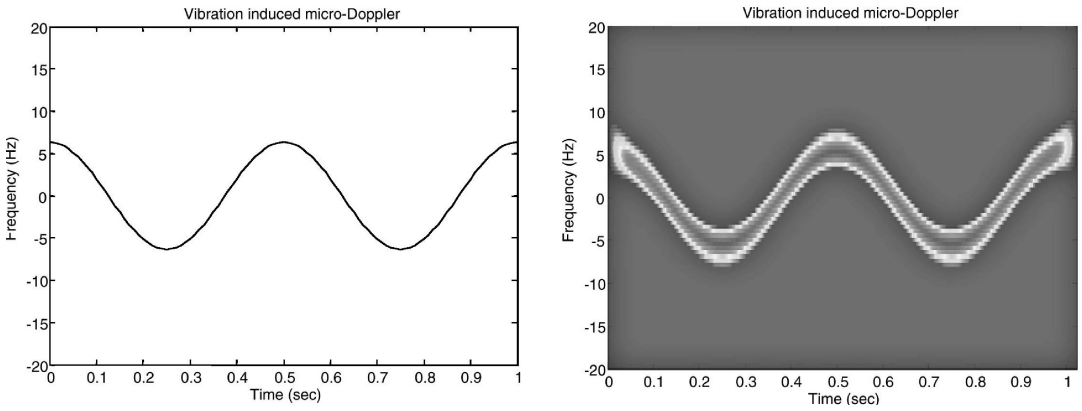


(a) (b)

Figure 3.2: (a) Theoretical and (b) time-frequency representation of the micro-Doppler from a vibrating point target

Figure 3.2-b Chen et al. [2006].

The geometry of the radar and a 3-dimensional rotating target is depicted in Figure 3.3. The radar coordinate system is defined by $(U, V, W)$; the target local coordinate system is defined by $(x, y, z)$; and the reference coordinate system $(X, Y, Z)$ is parallel to the radar coordinates $(U, V, W)$ and located at the origin of the target local coordinates. The azimuth and elevation angle of the target with respect to the radar coordinates (U, V, W) are $\alpha$ and $\beta$ respectively. Assume the target rotates about its axes $x$, $y$, and $z$ with an angular velocity vector $\vec{\omega} = (\omega_x, \omega_y, \omega_z)^T$ or a scalar angular velocity $\Omega = ||\vec{w}||$. The corresponding initial rotation matrix is $\mathcal{R}_{Init}$ Chen et al. [2006]. If a point scatterer $P$ is initially located at $\vec{r_0} = (x_0, y_0, z_0)^T$ in the local coordinates $(x, y, z)$, then viewing from the reference coordinates system $(X, Y, Z)$ the point scatterer $P$ will move to $\mathcal{R}_{Init} \cdot \vec{r_0}$ through rotating along the unit vector $\vec{\omega}' = (\omega'_x, \omega'_y, \omega'_z)^T$. Defining $\hat{\omega}'$ as the skew symmetric matrix, the rotational micro-Doppler shift can be obtained as Chen et al. [2006]

$$f_{mD} = \frac{\Omega}{\pi\lambda}[\hat{\omega}'(\hat{\omega}' \sin(\Omega t) + I \cos(\Omega t))\mathcal{R}_{Init} \cdot \vec{r_0}]_{radial} \tag{3.4}$$

where $I$ is the identity matrix of size $3 \times 3$. The micro-Doppler signature in the time-frequency domain is a sinusoidal function of $\Omega$ with an initial phase and amplitude depending on the initial position and the initial Euler angles $(\theta, \phi, \psi)$ of the point scat-

terer. Assume that the radar operates at 10 GHz and a target, located at ($U = 1000$

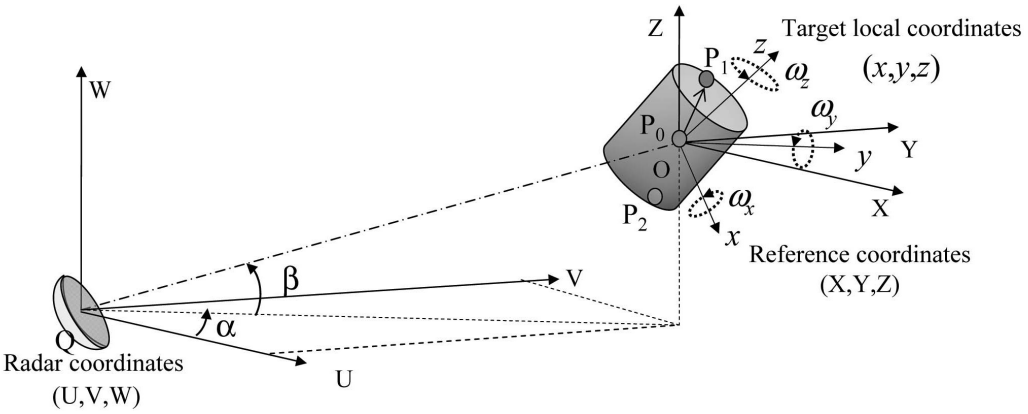


Figure 3.3: Geometry for the radar and a rotating target

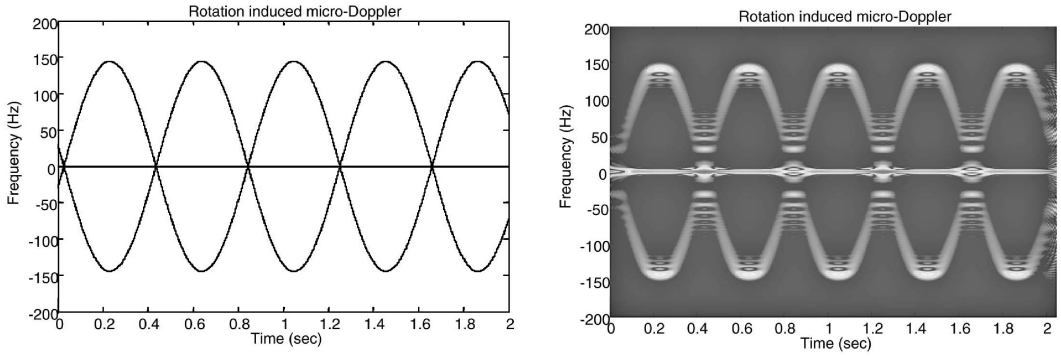


(a) (b)

Figure 3.4: (a) Theoretical and (b) time-frequency representation of the micro-Doppler from a rotating target

m, $V = 5000$ m, $W = 5000$ m), is rotating along the $x$, $y$, and $z$ axes with an initial Euler angles ($\theta = 30°, \phi = 20°, \psi = 20°$) and angular velocity $\vec{\omega} = [\pi, 2\pi, \pi]^T$ rad/s. Suppose the target has three strong scatterer centres: scatterer $P_0$ (the center of the rotation) is located at ($x = 0$ m, $y = 0$ m, $z = 0$ m); scatterer $P_1$ is located at ($x = 1.0$ m, $y = 0.6$ m, z =$0.8$ m); and scatterer $P_2$ is located at ($x = -1.0$ m, $y = -0.6$ m, $z = -0.8$ m). The theoretical micro-Doppler modulation calculated by (3.4) is shown in Figure 3.4-a. The micro-Doppler of the center point $P_0$ is the line at the zero frequency, and micro-Doppler modulations from the point $P_1$ and $P_2$ are the two sinusoidal curves about the zero frequency. Given a radar PRF of 1000 pulse/s and 2048 pulses transmitted during 2.05 s of dwell time, the simulated micro-Doppler

modulation signature is shown in the Figure 3.4-b, which is identical to the theoretical analysis. The rotation period can be obtained from the rotation angular velocity as $T = 2\pi/||\vec{\omega}|| = 0.8165$ s and is verified by both the theoretical and simulated results.

## 3.3 Micro-Doppler in radar imaging systems

Radar Imaging techniques such as Synthetic Aperture Radar (SAR), Inverse Synthetic Aperture Radar (ISAR) and Bistatic Synthetic Aperture Radar (BSAR) are well established and useful techniques to acquire high-resolution images of an area of interest from both airborne or space borne sensors. The amount of information provided from these systems is extremely high and its exploitation is still a growing field of research. For example, automatic target recognition based on the reflectivity images is a field of research with great interest and presenting many signal processing and design challenges Novak et al. [1998].

The extraction of m-D signatures from radar imaging systems for target classification purposes is an emerging technique. The research in this field provided interesting developments and results in the last years. This section will review the advances in the exploitation of the radar imaging platform for m-D analysis, showing that from this kind of sensors a significant advantage can be taken if the m-D information can be extracted.

### 3.3.1 Synthetic Aperture Radar

Synthetic Aperture Radar provides high resolution images of static ground scenes. The observed scenes may contain moving targets. As a result the processed image will change depending on the kind of target motion. Vibrating and rotating targets are two canonical cases that are often present within a scene. Rotating radar search antennas, wind turbines and vehicles that vibrate due to the engine are typical targets that exhibit micro-motions and related m-D characteristics. It is often possible to observe these micro-motions from a SAR. The analysis of the m-D features has been modelled and experimentally characterised for different type of targets, configurations and working frequencies over the last last decade.

In Ruegg et al. [2007] and Sparr and Krane [2003b] a derived signal model of the received baseband SAR signal from a target with m-D frequency $f_{mD}$ was shown to be:

$$s_b(t,T) = s(t,T)e^{-j(2\pi f_{mD}(T))t} \tag{3.5}$$

where $s(t,T)$ is the echo from a stationary target, $t$ is the fast time and $T$ is the slow time. For a vibrating target with vibrating amplitude $A_v$ and vibrating frequency $w_v$, the resulting m-D is:

$$f_{mD_{vib}(T)} = \frac{-2A_v w_v \sin(w_v T)}{\lambda_c} \tag{3.6}$$

where $\lambda_c$ is the carrier wavelength Ruegg et al. [2007]; Sparr and Krane [2003b]. This result is principally due to the cosine behaviour of the target in the radial direction. For a rotating target the motion presents a cosine and a sine component in quadrature leading to the following m-D frequency shift:

$$f_{mD_{rot}(T)} = \frac{2rw_r}{\lambda_c}(\sin(w_r T)\cos(\Theta(T)) + \cos(w_r T)\sin(\Theta(T)) \tag{3.7}$$

where $r$ is the rotating radius, $w_r$ is the rotating frequency and $\Theta(T)$ is the instantaneous aspect angle Ruegg et al. [2007].

In Sparr and Krane [2003b], the analysis method was also investigated, using quadratic time-frequency methods obtaining high time-frequency resolution representations. To test the Adaptive Optimal Kernel (AOK) real APY-6 SAR datasets were used to analyse the ground target oscillations. AOK was demonstrated to be effective in dealing with the problem of the selection of the sufficiently short time window to resolve properly the time frequency distribution of oscillating targets. In Figure 3.5, the experimental result using AOK analysis of a reflector with $2.0$ Hz vibrating frequency is shown Sparr and Krane [2003b]. The m-D signature varies between 70 and 85 Hz with a $2.5$ Hz oscillation peak-to-peak and a period of $0.5$ sec. This information introduces a modulation frequency of $2.0$ Hz in accordance with the ground truth. However, in the plot the resulting amplitude of the vibration is $1.5$ mm while the ground truth was of $8$ mm.

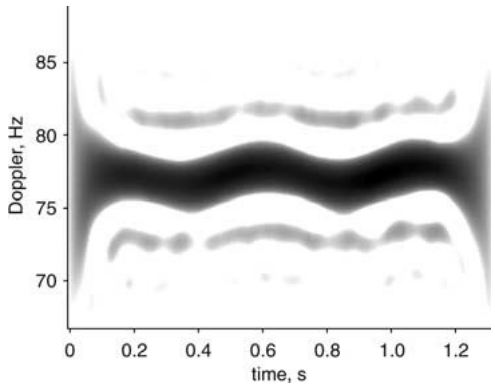


Figure 3.5: Time frequency signature of oscillating reflector analysed using the AOK method showing a feature oscillating between 70 Hz and 85 Hz with a 2.5 Hz oscillation peak-to-peak with a 0.5 seconds of periods. These values links to the ground truth Sparr and Krane [2003b].

In Sparr and Krane [2003b] this error is not analysed in depth. Figure 3.6-a shows the

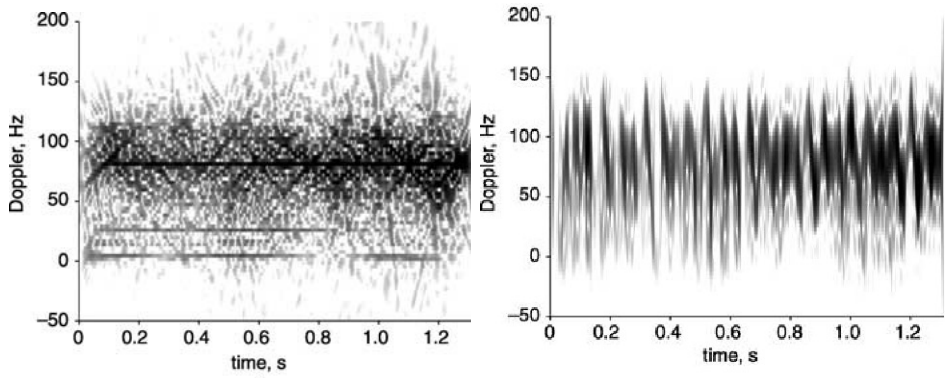


(a) (b)

Figure 3.6: Time frequency signature of oscillating reflector analysed using the AOK method. Two distributions are given with two different lengths of the time window used in the AOK analysis Sparr and Krane [2003b].

result obtained by using a window made of 256 samples, the same length used to obtain the result in Figure 3.5. Figure 3.6-b shows the result obtained with a window size of 16 samples. These results show that a longer window length results in a more-or-less stationary spectrum (which can be quite noisy), whereas a smaller window length produces a single instantaneous frequency with complicated time variations. From the results a modulation period of 0.5 seconds with a peak-to-peak deviation of 120 Hz has been estimated. These values correspond to a modulation frequency of 20 Hz with an amplitude of 7 mm, in agreement with the ground truth. This work was one of the

first m-D analysis of real data showing the feasibility of detecting m-D signatures to be exploited for target recognition purposes.

Silverstein and Hawkins Silverstein and Hawkins [2004] analytically derived the m-D signature of rotating objects in Synthetic Aperture Radar and highlighted differences with the vibrating case. They pointed out that the order required in the approximation of the expansion of the phase history needed to be greater than first order in the case of a rotation, while for the vibrating case a first order approximation was sufficient. The main reason was that in a rotational target the motion was large compared to the wavelength so a numerical analysis was required.

In Sparr [2005] Sparr presented the results of an experiment with a target moved along a trajectory in the azimuth direction, with oscillations superimposed in the range direction. Time frequency analysis methods were applied to the obtained datasets to show that m-D signatures can be exploited to distinguish targets with micro-motions from stationary targets. Experimental results are shown in Figure 3.7. Figure 3.7-a shows

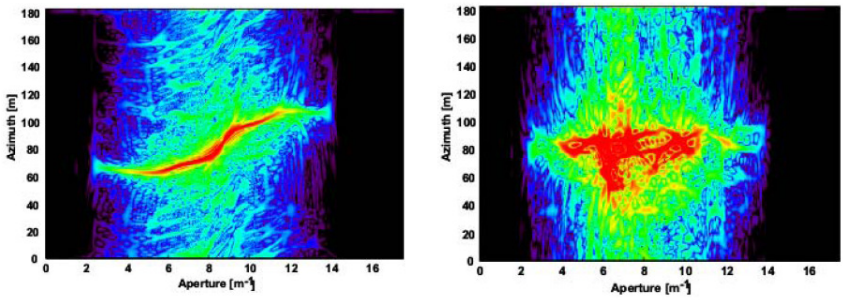


(a) (b)

Figure 3.7: Time frequency analysis of a) the moving target with micro-motions and b) a stationary building from Sparr [2005].

the time-frequency analysis results of a moving target with a radial micro-motion. In this figure the sinusoidal-like signature due to the micro-motion is evident. Figure 3.7-b shows the signature of a building. In this result only the stationary component due to the edge of the building and that of the multipath component can be seen.

The m-D effect from rotating and vibrating targets in millimetre-Wave SAR was analysed in Ruegg et al. [2007]. The very small wavelength facilitates the observation of very small vibrations such as those of a truck. Results for both simulated and real vibrating and rotating targets were presented in Ruegg et al. [2007]. The smoothed

pseudo Wigner Ville Distribution (PWVD) was used to provide a high resolution time-frequency representation. For real data, where the presence of noise affects the signal, the Gabor distribution was preferred. In Figure 3.8 the WVD of experimental data

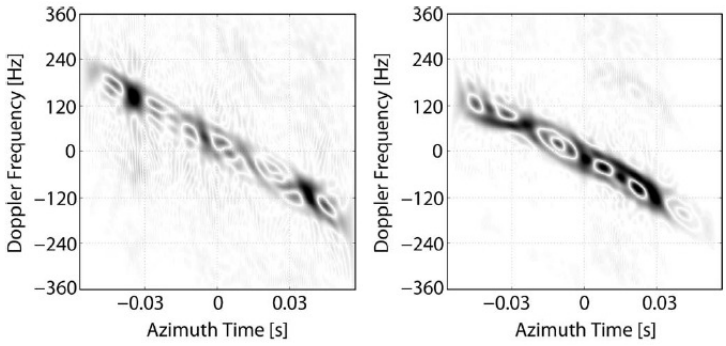


(a) (b)

Figure 3.8: Time-frequency representation (WVD) of the Doppler spectrum for (a) a static truck and (b) a vibrating truck Ruegg et al. [2007].

Ruegg et al. [2007] is shown. The dataset consists of data acquired over two trucks; Figure 3.8-a refers to the static truck, while Figure 3.8-b refers to the case of the truck with the engine switched on vibrating at 32 Hz and with a static second harmonic at 64 Hz. The plot of the static truck shows two very prominent areas around $\pm 150$ Hz. In Ruegg et al. [2007] this effect was justified by the space between the cab and the trailer of the truck which acted as corner reflector. In this case no pattern can be clearly recognised other than fluctuations due to the truck geometry. For the vibrating truck, Figure 3.8-b, a m-D pattern appears where a periodic signature with a period of 0.03 seconds corresponding to the 32 Hz of vibration of the truck. However, this feature is difficult to extract due to the strong return from the truck geometry.

The effect on SAR images was also analysed Chen et al. [2006]; Ruegg et al. [2007]. In this case if the micro-motion appears in the azimuth direction then this will cause smearing of the target. If the phase modulation is in the range direction then this causes an effect in SAR images known as paired echoes. The result of this effect will be the appearance of ghost targets in the cross-range direction on both sides of the original target. The target vibration can then introduce an infinite series of paired echoes $k$ because, when considering (3.6), the received signal (3.5) may be expressed as a series of expansion of Bessel functions of the first kind of order $k$ Chen et al. [2006]; Ruegg

et al. [2007]:

$$J_k(B) = \frac{1}{2\pi}\int_{-\pi}^{\pi} e^{j(B\sin(w_v T)-kw_v T)}d(w_v T), \tag{3.8}$$

where $B = A_v(4\pi/\lambda_c)$ and $J_k(B)$ decreases with increasing $k$. Thus the received signal can be written as:

$$s_b(t,T) = s(t,T)\sum_{k=-\infty}^{\infty} J_k(B)e^{jkw_v T}. \tag{3.9}$$

These ghost targets can appear stronger than the original target thus leading to incorrect interpretations of the focussed image that can mask other targets of interest.
From Ruegg et al. [2007], focussed simulated 94-GHz SAR data are presented in Figure 3.9. In Figure 3.9-a the simulated targets are vibrating at 30 Hz while in Figure 3.9-b they are vibrating at 50 Hz. Vibration amplitudes from left to right are 10, 1, 0.1, 0.01, and 0.001 mm for both cases. Targets with very large vibrations clearly show multiple and very densely spaced paired echoes in accordance with (3.9).

The most relevant recent work on monostatic SAR m-D was presented in Li et al. [2011]. In this paper, it was pointed out that in most of the previous work the targets were assumed to be point scatterers and that this assumption may not always agree with reality. The effect of micro-motions using distributed scatterers and localized scatterer model was addressed in this paper. Also more accurate and complex micro-motion models are introduced for rotating, vibrating sinusoidal moving and rocking targets, providing a good set of tools for the analysis in SAR. Two novel models for the phase history of the received echoes described in Li et al. [2011] includes: 1) A sawtooth expansion for a more accurate model of the phase modulation introduced by micro-motions and 2) a Generalized Paired Echoes Principle (PEP) to model the effect on the focussed image the general cases like a rocking ship.
An analysis of the effect on focussed images was also reported in Li et al. [2011] with the distinction of different micro-motions and their amplitude and frequency characteristics. The effect on different imaging algorithms was reported showing that the focussing algorithm plays a key rule in the final effect on the image.

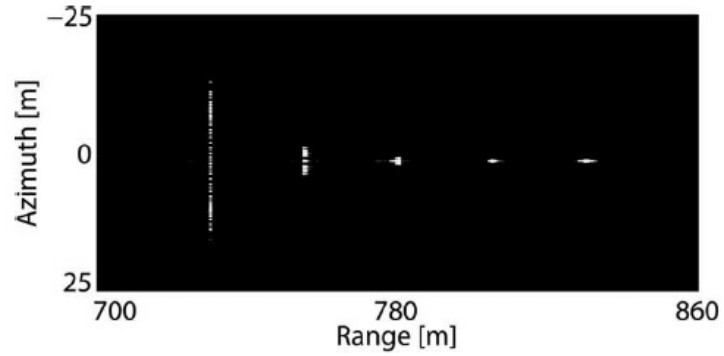


(a)

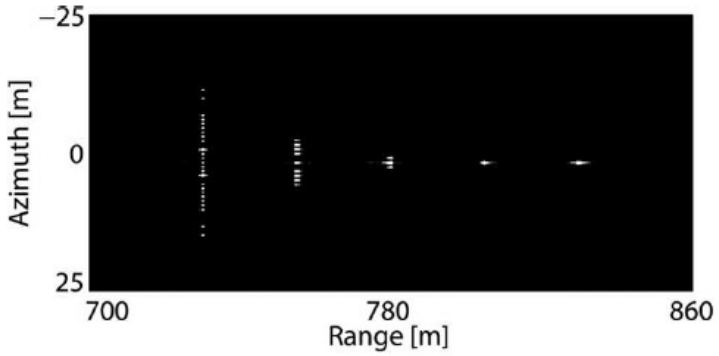


(b)

Figure 3.9: Focused 94-GHz SAR images, each with five simulated targets vibrating at (a) 30 Hz and (b) 50 Hz. Vibration amplitudes from left to right are 10, 1, 0.1, 0.01, and 0.001 mm for both images Ruegg et al. [2007].

The effect on images becomes stronger in the case of extended objects, as for examples wind turbines. Wind power is certainly one of the most economical and sustainable energy sources. In recent decades the number of wind turbines placed on hills, plains and off-shore continues to increase. For example in the UK a target has been set that 15% of energy should be generated by renewable sources by 2020. Wind farms are now a regular feature of the landscape in many countries, consisting of groups of individual wind turbines in a regular or near-regular array, located on land or at sea.

A typical wind turbine is made up of three components: the tower, the blades and the rotor. While the tower is a static object providing a zero Doppler return to the radar, the blades rotate introducing a Doppler shift to the scattered signals, then the signature of the turbine results to be time varying. This aspect can introduce an interference factor in radar systems generating undesired returns that i.e. can lead to false alarms in an air control system Perry and Biss [2007]. This contrast of technology causes problems on

both sides, the radar community has to deal with signals corrupted by this new component that changes the classic radar environment, while on the energy production side it reduces the areas where wind farms can be placed without interfering with strategical radar systems. For these reason detailed studies on the wind turbines effect in different radar systems and scenarios and moreover the mitigation of their effect on radar system can produce critical benefits to both the energy and radar communities.

The effect of wind turbines has been studied in the case of weather radars Gallardo-Hernando et al. [2011] where the wind turbines may cause the misidentification of thunderstorm features and meteorological algorithms errors. In Kong et al. [2011] the wind turbine radar cross section were characterized by laboratory measurement analysing a scaled wind turbine model and its interaction with a radar system. The effect of a new type of wind turbine on radar systems was analysed in Griffiths et al. [2011] showing possible advantages using a fitted mesh grid on the turbine.

On particular interest is the case of radar imaging system illuminating a wind turbine, when the wind turbine is active and is introducing Doppler effects in the backscattered echoes smearing and ghost echoes could appear in the focussed images. The effect of vibrating and rotating targets on SAR images has been studied in Ruegg et al. [2007] for the monostatic SAR case and in Chapter 6 for the bistatic SAR case, however only simple targets were considered and the focus of the papers was more on the signatures than on the effect on the images. In Li et al. [2011] the effect of micro-motions in SAR imagery has been analysed for targets with different kind of motions with simulated target injected in real dataset. Chapter 8 will analyse the case of the effect of wind turbines on the SAR images.

### 3.3.2 Inverse SAR

In Inverse Synthetic Aperture Radar imaging the radar platform is stationary and the target is moving with the assumption of a quasi-constant linear motion. Other target motions will produce errors in the final focussed image. The Doppler resolution is inversely related to the total time of coherently processed pulses. If the duration of the coherent processing interval (CPI) is too long, then uncompensated motion could

affect the image producing smearing in the Doppler dimension, affecting the Doppler resolution too.

Specific analysis and experiments about the analysis of wheels and pedestrian in ISAR was presented in Ghaleb et al. [2008]. The analysis first focussed on the model of the m-D effect from wheels of civil vehicles, demonstrating (with both simulated and real data) the possibility of extracting all the information required to correctly identify size, position, aspect angle and rotating frequency of a rotating wheel. The analysis then considered the case of the pedestrian, where an analysis of the features characterizing walking/running was reported. The paper demonstrated also the possibility to obtain information of the gait of the pedestrian using of time-frequency analysis on both simulated and real data.

In the last decade, however, the interest of the ISAR community moved from the analysis of the m-D signatures to the most challenging problem of the compensation of the micro-motions in order to obtain good focussed ISAR images. In Chen et al. [2009] a good review of the m-D analysis in ISAR was presented. Methods for analysing, visualizing, exploiting m-D signatures were reviewed in conjunction with examples of models for rigid and non-rigid body motions. Finally, Chen et al. [2009] introduces perspective in ISAR m-D exploitation.

The problem of extracting the modulation due to the micro-motion from the received signal has been addressed using various signal processing approaches. In Bin et al. [2007] a Chirplet decomposition method to separate the rotating and vibrating micro-Doppler from the target body echo was presented. The Wigner-Ville distribution was used for the time-frequency analysis exploiting the specific properties of the Gauss-Chirplet, in particular the absence of cross-terms. Different Chirplet bases are used to project the received echo in different Chirplet domains obtaining the separation of the body echoes from the micro-motion echoes on both simulated and real data. Fulin and Mingyuan in Fulin and Mingyuan [2010] proposed the use of the Singular Spectrum Analysis (SSA) to separate the m-D components from the rigid body components. SSA was used to decompose the original received signal in low frequency signal, quasi-periodic signals and noise. The SSA was applied to the range compressed signal. In this case the rigid body is represented by a singular eigenvalue in the eigenvalue spec-

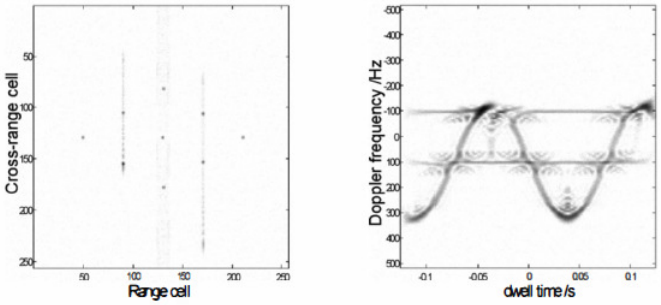


Figure 3.10: a) Simulated ISAR image and b) the time-frequency distribution of range cell 89 Fulin and Mingyuan [2010].

trum. This aspect is very helpful for the separation of the contributions. Results using the SSA based method from Fulin and Mingyuan [2010] are shown in Figure 3.10 and Figure 3.11. It is clear how the micro-motion modulation affects the resulting focussed image, Figure 3.10-a, and how selecting the correct components it is possible to obtain a clean image, Figure 3.11-d.

The next part of this review will focus on the imaging techniques used to mitigate the effect of micro-motions. In Zhu et al. [2010] a novel imaging method of birds was proposed, wherein a technique to remove the flapping spectrogram from the data firstly by the variety of moving average values of the cross-correlation coefficients of the high-resolution range profiles, and then removing the flapping spectrogram. In addition genetic algorithms and minimum waveform entropy were used for phase compensation. The effectiveness of the technique was demonstrated by simulations.

A real time imaging technique is proposed in Thayaparan et al. [2010]. The proposed technique used a time-frequency s-method based on the relationship between the short time Fourier transform and the Wigner Distribution. The s-method was tested on simulated data of a Boeing-717, a MIG-25, a Delta Wing and a Canadian Coast Guard Vessel providing good results in terms of motion compensation and computational efficiency.

The Complex Valued Empirical Mode Decomposition (CEMD) was proposed in Bai et al. [2008] to remove the micro-motion due to rotating parts in a target. The CEMD is able to identify rotating intrinsic mode functions (IMFs) for this reason was selected

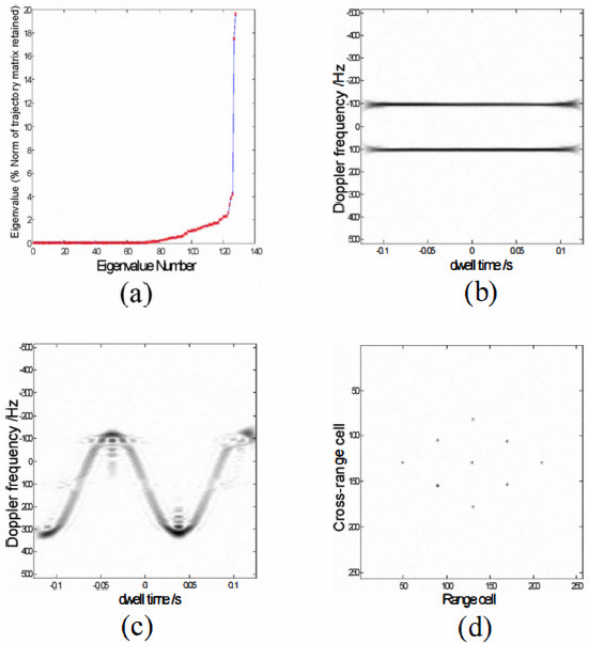


Figure 3.11: a) The singular spectrum of the $89^{th}$ cell, b) the time frequency distribution of the reconstruction signal, c) the time-frequency distribution of the residual signal and d) the cleaned ISAR image after the SSA Fulin and Mingyuan [2010]

as good technique to separate the different motion components. The technique was tested on both simulated and real datasets. In Figure 3.12 the results presented in Bai et al. [2008] are reported. The results refer to the application of the CEMD based technique to real data of a AN-26 plane. Figure 3.12-a shows the spectrogram of the echo in range cell 131. It can be seen that the m-D occupies the whole spectrum due to the frequency modulation of turbo blades. Figure 3.12-b shows the Range Doppler image of the data before the CEMD processing, while in Figure 3.12-c shows the same image after the CEMD processing. The last plot, Figure 3.12-d shows the normalized autocorrelation coefficient for the m-D in range cell 131, from this figure the rotation rate of 20 Hz can be estimated Bai et al. [2008].

In Bai et al. [2011] another approach for ISAR imaging of targets with rotating parts was presented. The authors proposed a data-recording model for two-dimensional (2D) ISAR imaging of rotating parts. The real-valued inverse Radon transform was then applied to image formation in the range-slow time domain. The rotating parts are imaged using complex-valued inverse Radon transform. The authors started from the assumption that for wide-band radar, the m-D signal induced by a rotating scatterer

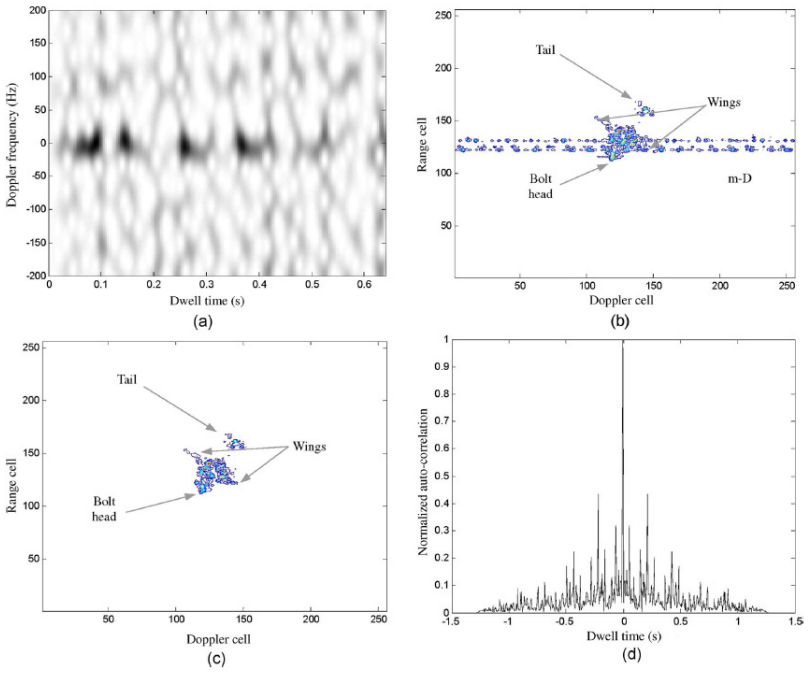


Figure 3.12: Image for measured data. (a) Spectrogram for range cell 131. (b) Image of raw data. (c) Image of the main body. (d) Normalized autocorrelation of m-D in range cell 131. Bai et al. [2008]

has sinusoidal modulus and phase in the range-slow time domain, which is equivalent to the Radon transform of its distribution function. Therefore, it can heuristically perform the inverse Radon transform to reconstruct the image. The authors then proposed two methods for ISAR imaging of rotating parts. In the range-slow time domain, the first method executes real-valued inverse Radon transform (RIRT) to echo modulus directly, while the second one applies complex-valued inverse Radon transform (CIRT) to the complex echoes. Because it performs coherent integration, the CIRT method achieves a higher spatial resolution than the RIRT method. The approach was tested on real AN-26 Plane data, which has a turbo engine on each side of the airframe. Figure 3.13-a shows the range Doppler image obtained from the echoes where the m-D strips due to the turbines can be observed. After the application of the m-D separation using chirplet decomposition the focussed image is seen to be less noisy as shown in Figure 3.13-b; Figure 3.13-c and Figure 3.13-d show the results of the focussed turbines using the RIRT algorithm. The four blades can be easily identified proving the effectiveness of the approach Bai et al. [2011].

In Ben-yu et al. [2010] an alternative view of m-D is given. Here the m-D was in-

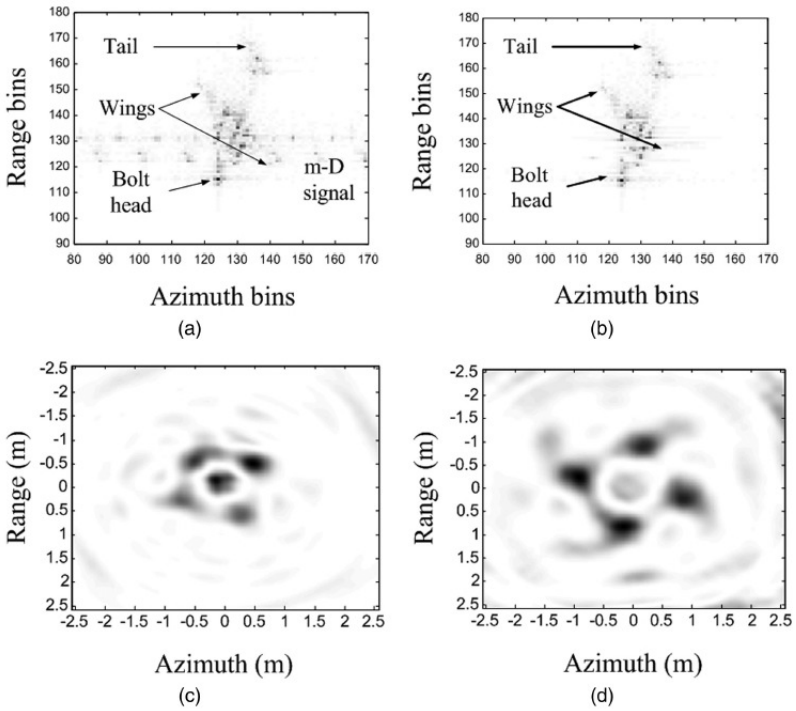


Figure 3.13: Image of AN-26 plane. (a) Image of the data with m-D. (b) Image of the data with the radon based approach. (c) Image of the first turbo. (d) Image of the second turbo. Bai et al. [2011]

troduced specifically for ISAR deception Jamming in order to reduce the efficiency of target recognition techniques. In the method proposed in Ben-yu et al. [2010] the intercepted radar signal is modulated by a template of false targets. The proposed method requires the interception of the radar pulse transmitted by the ISAR and extraction of the phase informations. Then an image synthesis system produces the required modulation for the false-target and the false-echo is transmitted to the ISAR. In Figure 3.14-a and Figure 3.14-b the resulting ISAR images without and with a 3 dB jamming are shown. The target is still visible in the focussed image. However, its recognition would be more difficult because the ghost echoes would lead a target recognition system to identify the target as an airplane with a turbine. The technique proposed in Ben-yu et al. [2010] is interesting but further analysis and experiments will be probably required to prove its usefulness.

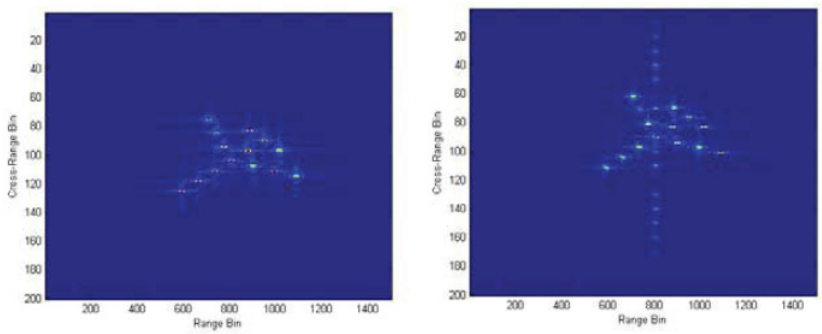


(a) (b)

Figure 3.14: ISAR image: a) without jamming b) with micro-motion jamming Ben-yu et al. [2010]

## 3.4 Conclusion

In this chapter, the basics of radar micro-Doppler have been introduced, the mathematical formalism and the study of canonical vibrating and rotating cases have been described. The recent advances in radar based m-D analysis from radar imaging systems have been introduced. Micro-Doppler from Synthetic Aperture Radar and Inverse Synthetic Aperture Radar are two novel field of research introducing interesting advantages. The presented review indicated how the information produced from the micro-motions of a target can affect the return to a SAR/ISAR platform. This family of radar systems provide the advantage to analyse the target reflectivity image of the target jointly with its micro-motion features. The radar imaging community could then take advantage of this complementary source of information for example to remove uncertainty in automatic target recognition systems. Micro-Doppler analysis from SAR systems is important since in Chapter 6 the micro-Doppler effect from Bistatic SAR is modelled and analysed, while the effect of wind turbines on SAR images will be analysed in Chapter 8.

## 3.5 Summary of the literature review

In Chapter 2 and Chapter 3 the review of the literature in the field of monostatic and bistatic SAR imaging and in the field of micro-Doppler signature analysis and extraction was performed.

The monostatic SAR focussing is a well addressed problem in literature with different approaches in both the time and frequency domain to achieve high resolution and efficient processing. The use of the Fractional Fourier transform has been introduced in A. S. Amein and J. J. Soraghan [2006]; Amein and Soraghan [2007] in order to obtain enhanced resolution. However this approach resulted to be not robust with respect to the azimuth variant property of the FrFT introducing errors in the correct image focussing.

Despite the monostatic case, bistatic SAR focussing is a challenging field of research. This is due to the geometry dependence of the received signal that makes difficult to obtain an accurate and efficient focussed image. The challenge becomes harder in the more general bistatic configuration: the azimuth-variant one. Neo [2007] and Wang et al. [2011] introduced the two most accurate bistatic point target spectrum to perform efficient frequency domain focussing of bistatic SAR images in the general configuration. However both models introduces approximations in order to get a signal model that can be then used focussing algorithms. Our contribute in this field deals mainly with these approximations improving the accuracy and the efficiency of the algorithms.

The micro-Doppler effect is a relatively new research field with growing interest in the last years. The potentiality of the exploitation of the information contained in the micro-Doppler signature is remarkable, however models, experiments and algorithms are still required. In particular only few works have been performed in the field of the micro-Doppler from radar imaging systems and most of them were limited to derive models and test them. As it is a new field of research different problems arise like: 1) the effect of the clutter that can bury the micro-Doppler signature; 2) the requirement of accurate models for different systems like bistatic SAR platforms and passive radar; 3) the study of the effect of micro-Doppler shifted signals on radar images from point or extended targets.

On these research threads will focus our attention in this thesis proposing new models and solutions for the exploitation of the micro-Doppler signatures.

# Chapter 4

# Fractional RDA and Enhanced Fractional CSA

## 4.1 Introduction

In this chapter two novel algorithms using the FrFT are derived. As mentioned in Section 2.4 the FrCSA suffered of a shift variance issue associated with the FrFT, this problem is addressed and resolved through the development of a new FrFT based Range Doppler Algorithm (FrRDA) and an enhanced version of the FrCSA called the enhanced FrCSA (eFrCSA). In the proposed approaches the conventional matched filter is removed and a new FrFT based process is developed. Unlike the FrCSA, the eFrCSA uses just the chirp compression property of the fractional Fourier transform for image focussing. The remainder of this chapter is organized as follows. Section 2 develops the new FrRDA and the eFrCSA. Section 3 presents a comparison of the new algorithms to the RDA and the CSA on simulated data sets and on real Radarsat-1 data.

## 4.2 FrRDA and eFrCSA

The basis of the new fractional Fourier Transform Based SAR processing algorithms developed is the fact that the optimum Fractional Fourier transform for a linear chirp signal allows us to obtain good resolution in the time-frequency domain. For exam-

ple two different chirp signals that overlap in time and frequency can be distinguished using the FrFT Capus and Brown [2003]. The two dimensional chirp behaviour Cumming and Wong [2005] of the received SAR signal allows us to exploit the potential of the fractional Fourier transform for SAR processing. In our approach the matched filter within the RDA and the CSA are replaced with an optimum FrFT and time-mapping operation to form the FrRDA and the eFrCSA. These two operations are needed in both the range and azimuth directions.

*Fractional order estimation*

The compression is performed through the use of the optimum transformation angles for both the range and azimuth directions. The optimum transformation is computed using (2.4). Adapting this equation for the range and azimuth LFM signals yelds:

$$\begin{aligned} \theta_{opt_{rg}} &= -\tan^{-1}\left(\frac{F_s^2/(N)}{2k_{rg}}\right) \\ \theta_{opt_{az}} &= -\tan^{-1}\left(\frac{PRF^2/(PRF \times dur)}{2k_{az}}\right) \end{aligned} \tag{4.1}$$

where $F_s$ is the sampling frequency in the range direction and $PRF$ is the receiver Pulse Rate Frequency. $N$ is the number of valid samples in the range direction while $dur$ is the duration of the acquisition that multiplied by the $PRF$ gives the number of samples in the azimuth direction. $k_{rg}$ and $k_{az}$ represent the range and azimuth chirp rate respectively.

*Time-mapping operation*

The fractional Fourier transform is shift variant Bultheel and Martinez [2002] and thus an issue exists with the time location and the correct spatial localization of point scatterers. This issue is due to the effect introduced in the fractional domain in terms of compression of the samples spacing by a factor $|\cos(\theta_{opt})|$ where $\theta_{opt}$ is the optimum transformation angle used in the FrFT. This means that in order to have the same

number of samples in the image and the same time position obtained using a traditional focussing technique a *time mapping* operation is required. This operation comprises the computation of the total amount of samples that lie in the interval $[\tau_{start}, \tau_{stop}]$, where $\tau_{start}$ and $\tau_{stop}$ are the start and the stop sampling times of the linear chirp respectively.

Using the FrFT to compress a linear chirp signal into a compact form reduces the number of samples that lies in the interval $[\tau_{start}, \tau_{stop}]$ compared to the original number of samples. It is observed that the resulting sampling period in the fractional domain is equal to the original sampling period multiplied by a factor $\frac{1}{|\cos(\theta_{opt}|}$. Consequently in order to obtain the original number of samples upsampling and interpolation operations are required.

The optimum fractional Fourier transform forms a compact support of the linear chirp signals. Uncorrelated noise is present for all time and frequencies, because for such noise no linear relationship between time and frequency is present. This implies that the noise will be mismatched with the selected fractional domain and spread over the entire domain as illustrated in Figure 4.1-a. As indicated a subset of the fractional bins will contain the useful signal, this subset is shown by the dashed lines in Figure 4.1-a. The mapping procedure described above is used on Figure 4.1-a to produce Figure 4.1-b. This implies that a certain number $M$ of samples (234 in the case showed in Figure 4.1-a) of the noise will be outside the limit $[\tau_{start}, \tau_{stop}]$ after the fractional Fourier transform. This implies that from an $N$-sample FrFT of the received signal, $N - M$ points will be mapped into $N$ points in the time domain. Thus the time mapping operation includes an inherent noise filtering process that does not affect parts of the compressed linear chirp relative to the received echoes (in the example in Figure 4.1 the SNR is increased of 0.2 dB). As indicated in 4.1-b the result now lie in the fractional / time domain and no inverse fractional Fourier transform or Fourier transform is required. In the case of the linear chirps the removed M samples in this process will contain only noise.

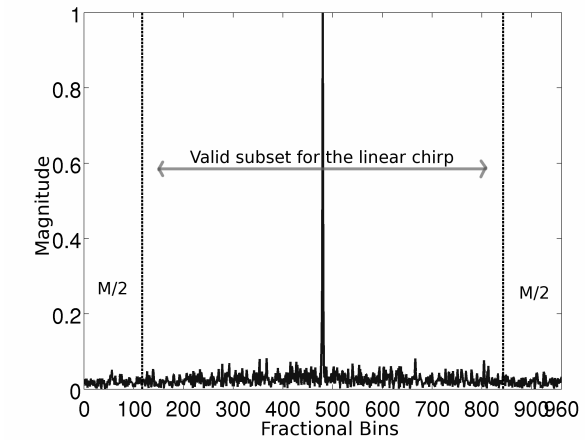


(a) Optimum FrFT of a chirp signal before the time projection, the dashed lines represent the limit in terms of samples used in the time-projection

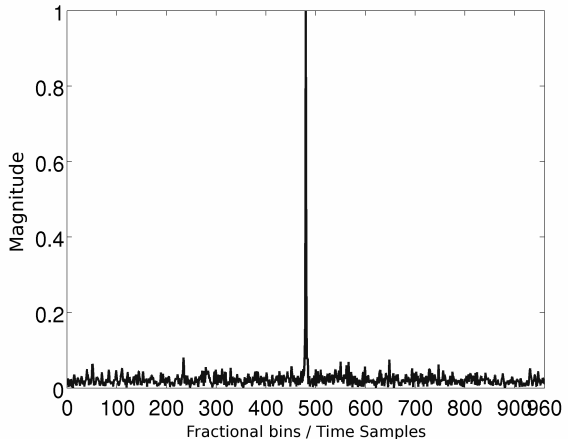


(b) FrFT of a chirp signal after the time projection

Figure 4.1: Example of the noise power in the time-projection operation.

### 4.2.1 Fractional Range Doppler Algorithm (FrRDA)

The core steps of the proposed FrRDA algorithm are described below:

**1. Azimuth FFT:** The first step is the azimuth FFT to carry the data in the range-Doppler plane.

**2. RCMC:** As in the traditional RDA in the range-Doppler domain RCMC is performed to correct the target trajectories. This operation must be performed before the azimuth correction in order to bring the correct amount of energy in each range gate. Two implementations of this operation are possible, the first one is a range interpolation in the range-Doppler domain and the second involves the assumption that the

Range Cell Migration is range invariant, at least over a finite range region, in this case the RCMC can be implemented using an FFT, linear phase multiply, and IFFT technique Cumming and Wong [2005].

**3. Azimuth FrFT:** A fractional Fourier transform across the range gates is used to perform the azimuth compression. The rotation angle to be used in this FrFT must take care that data lies already in the range-Doppler plane, in this case the signal results to have already been rotated by an angle $\frac{\pi}{2}$. Thus the rotation angle to be applied must be $\theta_{az} = -(\frac{\pi}{2} - \theta_{opt_{az}})$, where $\theta_{opt_{az}}$ is computed using (4.1). Since the received signal in the azimuth direction is the superposition of LFM signals coming from each scatterer, the FrFT of each range gate will produce a series of peaks, one for each scatterer on ground.

**4. Azimuth time mapping:** A time mapping of a factor $\frac{1}{|\cos\theta_{az}|}$ is needed in order to obtain a correct time spacing between the different point scatterers, where $\theta_{az}$ is the rotation angle for the azimuth gates. A resampling step and a linear interpolation are needed to obtain the correct number of samples of the linear chirp in the image plane.

**5. Range FrFT:** The fractional Fourier transform across the azimuth gates is used to perform the range compression step, in this case the transformation order used is the optimum transformation order computed from (4.1). As in the azimuth direction, the range received signal is the superposition of LFM signals weighted for the scatterers intensities and will results in a series of peaks, one for each scatterer on ground.

**6. Range Time Mapping:** A range time mapping of a factor $\frac{1}{|\cos(\theta_{opt_r})|}$ is needed in order to obtain a correct time spacing between the different point scatterers, $\theta_{opt_r}$ is the optimum rotation angle for the azimuth gates. After this operation a resampling and a linear interpolation are also required.

Unlike the traditional RDA the FrRDA uses azimuth processing before the range processing. In the time mapping operation some numerical errors can be present. The RCMC is then anticipated in the processing in order to prevent the propagation of the errors from the time mapping interpolation. However in case of dechirped signal the fractional azimuth processing can still be performed.

### 4.2.2 Enhanced Fractional Chirp Scaling Algorithm (eFrCSA)

The main difference between the new eFrCSA and the FrCSA proposed in A. S. Amein and J. J. Soraghan [2006]; Amein and Soraghan [2007] is now described. In the FrCSA the fractional Fourier transform was used to obtain a model of the fractional spectrum of the received signal in both azimuth and range directions. Based on this spectrum model two matched filters were designed to focus the image, then the inverse Fractional Fourier transform was applied in both directions to get the image in the image plane.

The eFrCSA does not work on a fractional domain based spectrum model. Instead it exploits the LFM compression property of the FrFT in order to focus the image in both azimuth and range directions. A novel mapping process is used in the eFrCSA.

The core steps in the proposed enhanced Fractional Chirp Scaling Algorithm (eFrCSA) are described below Clemente and Soraghan [2010]:

**1. Azimuth FFT:** The first step in the algorithm is the Fourier transform in the azimuth direction in order to obtain the data in the range-Doppler domain.

**2. Chirp Scaling and phase correction:** in this step the range migration is equalized and the phase shift is applied along the constant azimuth frequency lines, in addition the range-varying reference signal is multiplied to correct the residual phase.

**3. Range FFT:** the FFTs in the range directions transform the data into the 2-D frequency domain.

**4. SRC and bulk RCMC:** are performed through a phase multiplication with a phase function as in Raney et al. [1994].

**5. Range FrFT and Time Mapping:** The fractional Fourier transform across the azimuth gates is used to perform the range compression step. The rotation angle to be used in these FrFT must take care that the data lies into the 2-D frequency plane, then $\theta_{rg} = -(\frac{\pi}{2} - \theta_{opt_{rg}})$. This process produces a series of peaks due to the overlap of echoes coming from each scatterer on ground in the range direction. As in the FrRDA case a range time mapping of a factor $\frac{1}{|\cos(\theta_{opt_{rg}})|}$ is required in order to obtain a correct time spacing between the different point scatterers.

**6. Azimuth FrFT and Time Mapping:** A fractional Fourier transform across the range gates is used to perform the azimuth compression. The rotation angle to be used

in these FrFTs must take care that data lies in the range-Doppler plane in a similar fashion as the FrRDA. The FrFT will produce a peak for each scatterer in the azimuth direction, each one of this weighted by the reflectivity of the scatterers. Finally a time mapping of a factor $\frac{1}{|\cos\theta_{az}|}$ is needed in order to obtain a correct time spacing between the different point scatterers.

### 4.2.3 Algorithm complexity

As indicated in section 2.4.1 the FrFT comprises a chirp multiplication followed by a chirp convolution and by another chirp multiplication. Therefore the FrFT complexity is calculated as $2N$ (required for 2 chirp multiplications) plus $N\log_2 N$ (required for 1 convolution using the FFT). This is approximated as $N\log_2 N$. This complexity is comparable with the computational complexity of a matched filter.

In comparing the computational complexity of the RDA and the FrRDA we can consider that the RCMC and the azimuth FFTs as common operations to both the algorithms while the range FFTs/IFFTs, the range compression multiplication, the azimuth IFFTs and the azimuth compression multiplication are replaced with the range and azimuth FrFTs and related time mappings.

In the case of the CSA and the eFrCSA the azimuth FFTs, the chirp scaling operation, the range FFTs, the RCMC, SRC and the residual phase correction multiplication are common to both the algorithms while the range IFFTs, the azimuth compression and azimuth IFFTs are replaced with the range and azimuth FrFTs and time mapping.

The FrRDA and the eFrCSA have a higher computational complexity principally due to the time mapping operations, indeed the complexity of the FrFTs are comparable with the amount of operations needed to perform the matched filtering in the traditional algorithms. This additional complexity depends on what kind of interpolation is used in the time mappings. In the proposed algorithms linear interpolation has been used due to the fact that in real SAR systems the resulting amount of points to synthetize in the time mapping operation is relatively small, and therefore the computational cost of the algorithm is not significantly increased. However increasing complexity of the algorithms can be overcome using parallel versions of the algorithms. The FrFTs and the time mapping operations are one-dimensional operations and that can be easily paral-

lelized thus decreasing the required time consumption Clemente et al. [2009],di Bisceglie et al. [2010]. The relative complexity between FrRDA and eFrCSA is similar to the relative complexity between RDA and CSA Hughes et al. [1996]. In both cases the computational complexity of the matched filtering process is increased through the use of the FrFT and time mapping stages. Consequently the FrRDA will have less computational complexity providing less accurate results than the new eFrCSA.

## 4.3 Algorithm testings

Simulated and real data are used to investigate the performance of the FrRDA and eFrCSA relative to the conventional RDA and CSA in order to demonstrate the capability of the proposed approach for improved SAR data image construction.

### 4.3.1 Results from simulated data

Table 4.1 defines the parameters of the working SAR configuration that is used to generate simulated raw SAR data for testing the new algorithms against traditional approaches. The results have been obtained with the RDA and the Fractional RDA for a single point scatterer in the scene, with and without noise. From these simulation

| | |
|---|---|
| **PRF** | 1600 Hz |
| **Carrier Frequency** | 4.5 GHz |
| **Pulse Duration** | 40 $\mu$s |
| **Flight Duration** | 1 s |
| **Pulse Bandwidth** | 20 MHz |
| **Platform Velocity** | 7000 m/s |

Table 4.1: SAR simulation parameters

the resulting gain using the FrRDA in terms of resolution is measured at $2.76\%$ in the range direction while in the azimuth direction is measured at $37.21\%$.

In Table 4.2 the SideLobe Level (SLL), the Peak SideLobe Ratio (PSLR) and the Integrated SideLobe Ratio (ISLR) over 10 sidelobes are presented. The SLL is defined as the level of the first side lobe while the PSLR and the ISLR are defined as following:

$$PSLR = 10\log\frac{\text{maximum sidelobe power}}{\text{main lobe power}}$$

$$ISLR = 10\log\frac{\text{total power in sidelobes}}{\text{main lobe power}}$$

From the results in Table 4.2 it is noted that the the FrRDA introduces advantages in

| | **SLL [dBs]** | **PSLR [dBs]** | **ISLR [dBs]** |
|---|---|---|---|
| **RDA-Range gate** | -14.74 | -16.73 | -11.93 |
| **FrRDA-Range gate** | -17.18 | -23.42 | -16.65 |
| **RDA-Azimuth gate** | -21.21 | -20.60 | -17.48 |
| **FrRDA-Azimuth gate** | -21.15 | -19.97 | -18.76 |

Table 4.2: Measured SLL, PSLR and ISLR values for the RDA and the FrRDA

the focussing in the azimuth direction in terms of sidelobes level reduction, however the same advantages are not evident in the range direction where only the ISLR value is improved.

In Table 4.3 the measured SNR values for different simulated scatterer configurations are shown. The simulated reflectivity profiles are a single point scatter, two close point scatterers, a $3 \times 3$ matrix of 9 point scatterers and an extended object with the shape of an airplane (shown in Figure 4.2). In these cases the simulated SNR on the simulated received signal was $-6$ dBs and the resulting average SNR is obtained using different configurations of point scatterers from 100 simulations. The results obtained using the reflectivity profile shown in Figure 4.2-a shows that the FrRDA effectively improves the SNR in the image respect to the RDA, as can be seen in Figures 4.2-b and -c, confirming the measured results in Table 4.3. Additionally less blurred bounds of the extended objects are observed. From Table 4.3 it is observed that the fractional approach enhances the SNR in the resulting image in the case of single and multiple point scatterers and for extended objects. The signal power is computed using a focused noiseless scene, while the resulting noise power is computed subtracting the result from the noiseless focused data from the noisy data. Further simulated data were performed using the same simulation parameters as in Table 4.1 for testing the performance of the eFrCSA. The resulting resolution gain obtained using the eFrCSA

| Scatterers | Single | Couple | Multiple | Airplane (ext. obj.) |
|---|---|---|---|---|
| **RDA [dBs]** | -33.27 | -43.71 | -34.54 | -29.81 |
| **FrRDA [dBs]** | -32.86 | -40.27 | -32.95 | -28.68 |
| **Improvement [dBs]** | 0.41 | 3.44 | 1.59 | 1.13 |

Table 4.3: SNR values for different simulated datasets

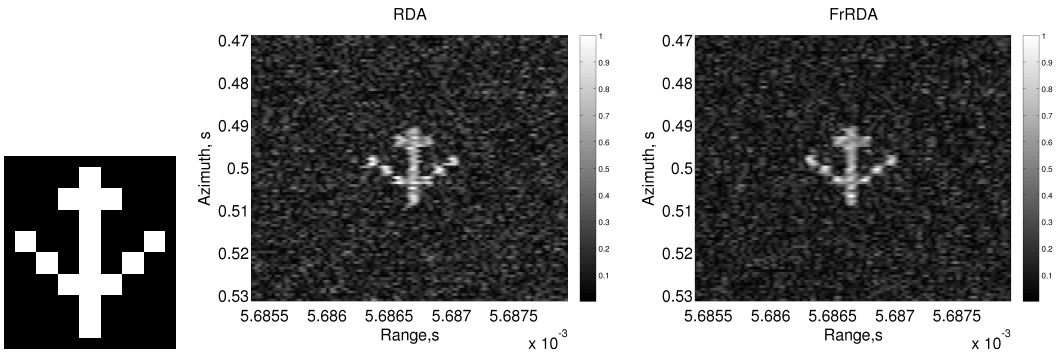


(a) Reflectivity Profile (b) RDA (c) FrRDA

Figure 4.2: Simulated reflectivity profile and result obtained with the RDA and FrRDA for the extended object.

with respect to the CSA is measured $9.09\%$ in azimuth resolution and $13.29\%$ in range resolution. The resolution gain provided by the FrCSA with respect to the CSA is of $15.79\%$ for the range direction, while in the azimuth direction the CSA actually provides better performance with a resolution $5.48\%$ better than the FrCSA A. S. Amein and J. J. Soraghan [2006]; Amein and Soraghan [2007].

The improvement in the focussing quality, using the eFrCSA, can be measured using the Side Lobe Level (SLL) the Peak Side Lobe Level (PSLR) and the Integrated Side Lobe Level (ISLR) which are given in Table 4.4 the SLL, the PSLR and the ISLR over 10 sidelobes. From the results in Table 4.4 it is noted that the the eFrCSA introduces

| | SLL [dBs] | PSLR [dBs] | ISLR [dBs] |
|---|---|---|---|
| **CSA-Range gate** | -14.01 | -16.30 | -10.84 |
| **eFrCSA-Range gate** | -23.52 | -24.29 | -18.97 |
| **CSA-Azimuth gate** | -16.18 | -15.17 | -12.81 |
| **eFrCSA-Azimuth gate** | -26.01 | -23.09 | -20.58 |

Table 4.4: Measured SLL, PSLR and ISLR values for the CSA and the eFrCSA

advantages in the focussing in the range and azimuth direction in terms of sidelobes level reduction. In addition, comparing the performances obtained with the FrRDA in

Table 4.2 with the performances obtained with the CSA in Table 4.4 it is evident that the FrRDA improves the RDA approaching that of the CSA.

The eFrCSA compared to the FrCSA also has an advantage in terms of focussing quality. Using the same simulations in Amein and Soraghan [2007], the performances in terms of SLL, PSLR and ISLR for the CSA and the FrCSA are given in Table 4.5. Table 4.5 demonstrates that the FrCSA has not the same capability to improve the CSA

| | SLL [dBs] | PSLR [dBs] | ISLR [dBs] |
|---|---|---|---|
| **CSA-Range gate** | -22.01 | -21.15 | -22.36 |
| **FrCSA-Range gate** | -20.94 | -23.24 | -23.01 |
| **CSA-Azimuth gate** | -13.34 | -16.71 | -13.10 |
| **FrCSA-Azimuth gate** | -14.21 | -16.89 | -13.32 |

Table 4.5: Measured SLL, PSLR and ISLR values for the CSA and the FrCSA in Amein and Soraghan [2007]

of the eFrCSA.

### 4.3.2 Results from real data

The FrRDA and the eFrCSA have been tested on real data from the Radarsat-1 platform Radarsat-1. The analysed dataset is a portion of the pass contained in Cumming and Wong [2005]. The results are compared with the RDA, the CSA and with the results obtained using the Gamma Modular SAR Processor (MSP) Werner et al. [2000] . The Gamma MSP is an accurate range-Doppler SAR processor, in particular it incorporates features like the Doppler ambiguity estimation and the secondary range migration for the RADARSAT platform that are generally not included in the standard RDA. For this reason the results obtained with this processor are very accurate and are used as ground truth to verify the performances of our algorithms.

The analyzed area processed with the Gamma MSP is shown in Figure 4.3. In Figure 4.4 a zoom of the Tsawwassen ferry terminal area processed with the RDA and the FrRDA is illustrated. In the FrRDA the results are seen to contain less blurred bounds, more accurate detail separation and more clear detection of the different extended objects in the analysed area, as highlighted by the red arrows. In this result the

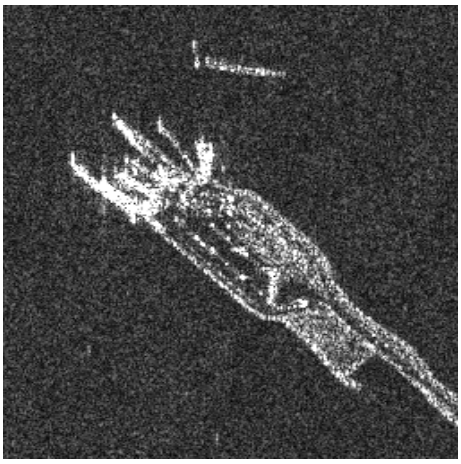

Figure 4.3: The Tsawassen ferry terminal in Vancouver, Radarsat image processed with Gamma MSP

improvement of the sidelobe level in the FrRDA is evident, reducing the target masking. These results are confirmed by comparing them to Figure 4.3 from the Gamma MSP.

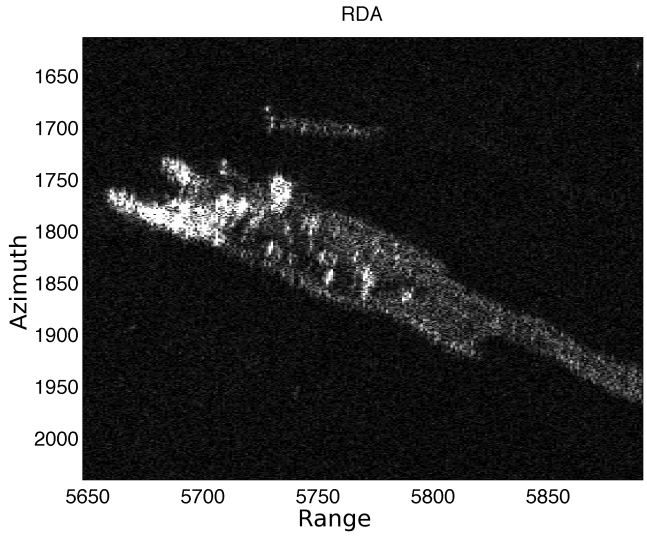


(a) RDA

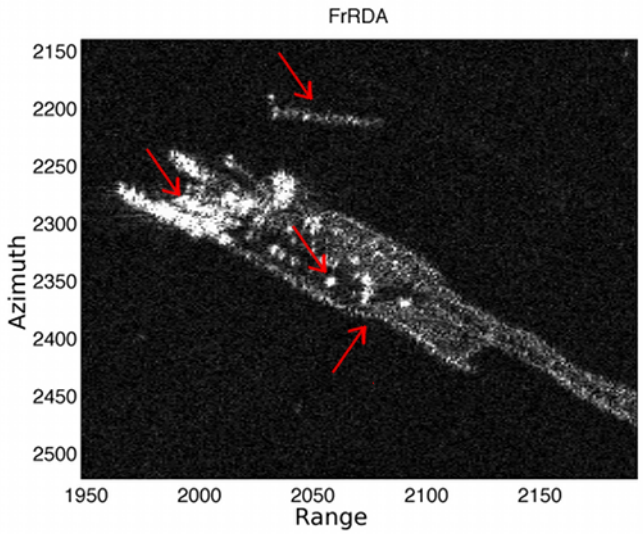


(b) FrRDA

Figure 4.4: Portion of the Tsawwassen ferry terminal area processed with the RDA and the FrRDA.

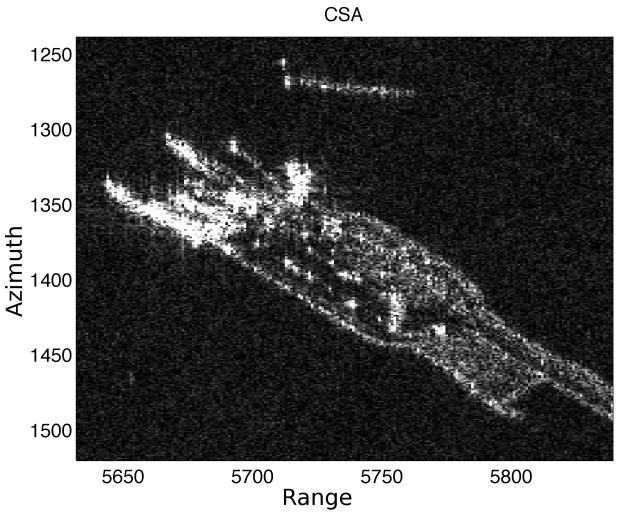


(a) CSA

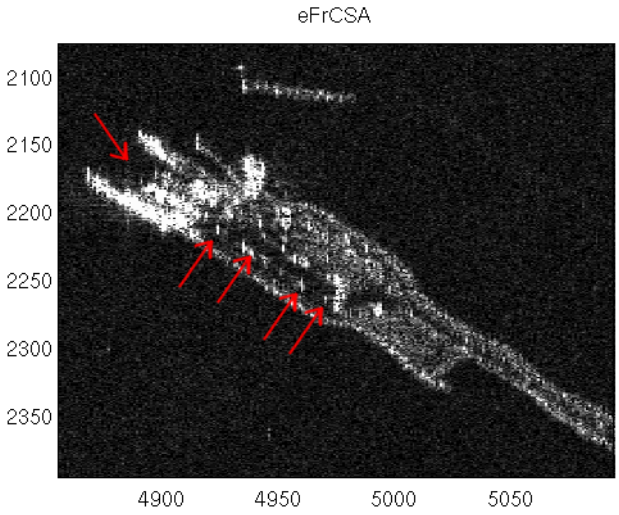


(b) eFrCSA

Figure 4.5: Portion of the Tsawwassen ferry terminal area processed with the CSA and the eFrCSA.

The results of processing the Tsawwassen ferry terminal area processed with the CSA and the eFrCSA is shown in Figure 4.5. In this case there are smaller differences between the two results, the eFrCSA provides better focussing of the small scatterers as seen in the top-left area of the image, with the presence of larger extended objects. The execution time of the algorithms using a Dell Optiplex 760 with an Intel Core 2 Quad CPU at 3.0 GHz with 4 GByte of RAM were measured. To process a $4000 \times 4000$ samples the RDA required 10.2 seconds while the FrRDA took 15.4 seconds. For the

same dataset the CSA required 11.03 seconds while the eFrCSA took 16.3 seconds. These timing results are in accordance with the computational complexity analysis described in Section 4.2.3.

## 4.4 Conclusion

In this chapter two new SAR focussing algorithms have been presented using the Fractional Fourier Transform applied to the Range Doppler Algorithm and to the Chirp Scaling algorithm. The FrFT and a time-mapping operation are used to replace the matched filter used in the RDA and CSA. The resulting FrRDA and eFrCSA algorithms use the property of the Fractional Fourier Transform to resolve chirp signals to increase the resolution of the point scatterers in the scene. The two proposed algorithms have been developed directly from the RDA and the CSA. The algorithms use the fractional Fourier transform to replace the matched filtering in the conventional algorithms.

The proposed approach has been tested with simulated data and real Radarsat-1 data. For both the proposed algorithms the proposed approach showed to improve the quality of the impulse response both in terms of side lobes and resolution. The simulation results indicate that the fractional Fourier transform approach provides superior point scatterers responses and provides more accurate reflectivity profile in the case of extended objects, enhancing the resolution, the signal to noise ratio and generally decreasing the sidelobes. For the FrRDA the sidelobes in the azimuth direction appeared to be higher than the RDA but in this dimension the resolution gain was appreciable. In addition the performances provided by the FrRDA have been shown to be comparable with those from the CSA. The algorithms have been tested with real Radarsat-1 data, the results have been compared with the RDA, the CSA and those obtained with the Gamma MSP.

The FrRDA provides superior results to the RDA in the case of real data providing better accuracy, less blurred results and a higher capability of detection. The eFrCSA provides an improvement in terms of resolution with respect to the CSA especially for extended objects.

# Chapter 5

# Bistatic PTS using Chebyshev Approximation

## 5.1 Introduction

In this chapter we present a new approach using the Chebyshev polynomial approximation J.Mason [1996] to improve the bistatic point target spectrum (BPTS). The new approach is applied on two existing BPTSs replacing in both the less accurate (at parity of approximation order) Taylor approximation.

In the first case the bistatic slant range function approximation is replaced using the Chebyshev one in order to obtain a polynomial representation that can be used in the Method of Series Reversion Neo [2007]; Neo et al. [2007]. The coefficients obtained with the Chebyshev approximation are replaced in the power series of the bistatic slant range function leading to a more accurate application of the method of series reversion obtaining better results in terms of phase accuracy of the spectrum.

In the second case a similar approach is used in order to improve the 2D PSP based PTS Wang et al. [2011] replacing the Taylor expansion. The improvements using the Chebyshev polynomial approximation are obtained replacing the Taylor approximation in the decoupling of the range-azimuth frequency components. The proposed approach replaces the coefficients of the polynomial Taylor series expansion of the azimuth-range frequency coupling term with the ones obtained using the Chebyshev polynomial approximation. The obtained coefficients are then used to obtain an ana-

lytical formulation of the bistatic point target spectrum as in Wang et al. [2011]. In Section 2.5.3.1 and Section 2.5.3.2 the analytical development of the two BPTS are reported while in Appendix A the theory of the Chebyshev polynomial approximation is introduced. The remainder of the chapter is organized as follows. In section II the new method of using Chebyshev polynomials to approximate the slant range function is developed. Section III presents comparative results that indicate the superior performance obtained to those obtained using the conventional approximation method Neo [2007]; Neo et al. [2007]. In section IV the new method of using Chebyshev polynomials is developed deriving the new bistatic Point Target Spectrum based on the 2D PSP Wang et al. [2011]. Section V presents comparative results that indicate the superior performance obtained to those obtained using the original method Wang et al. [2011].

## 5.2 Slant Range Approximation for the MSR BPTS

Weierstrass theorem Rivlin [2003] suggests that polynomial approximation of a continuous function in an interval $[a, b]$ can be always performed. A common approach in obtaining an approximating polynomial is to minimize the square residual for the approximation of a function. This minimization finds a solution for the least squares problem, which is solved using an interpolating polynomial family of orthogonal polynomials. The use of this kind of polynomial approximation facilitates convergence to the target function as the approximation order increases. The orthogonal Chebyshev polynomials allow us to obtain an approximation which minimizes the error in the sense of the least squares Rivlin [2003] and the infinity norm. Compared to the Legendre approximation, proposed in Wang and Li [2010], the Chebyshev polynomials allow us to obtain a least squares approximation of the slant range function that includes the property of a bounded maximum error thus minimizing the so called *Runge effect* J.Mason [1996]. In addition the mathematical and computational complexity is reduced. In general the Chebyshev polynomials offer closer approximation to the minimax polynomial which represent the polynomial with the smallest maximum deviation from the true function Mason [1993]. It Abutheraa and Lester [2007] it was shown that the use of Chebyshev polynomials to approximate functions outperforms

the Taylor series expansion. For these reasons Chebyshev approximation was chosen to replace the Taylor series. The properties of the Chebyshev polynomials lead to a better approximation of the phase history of the signal allowing the design of a more accurate matched filter to improve the image quality.

In this section the Chebyshev approximation is used to represent the double squared root range function of the bistatic SAR geometry. The Chebyshev approximation is stopped at the $4^{th}$ order for the computation of $R(\eta)$ in (2.5). In this way our analysis is comparable with that in Neo [2007]; Neo et al. [2007], in order to show that using the Chebyshev polynomial, with the same order of the expansion, results in better approximation of the slant range function. In addition the uncompensated phase error should be limited to be within $\pm\pi/4$, in order to keep good image quality, and the $4^{th}$ order approximation can guarantee this condition for a large family of acquisition configurations for the approach used in Neo [2007]; Neo et al. [2007]. The order can be reduced to the $3^{rd}$ in the cases where the phase error is already within the limits of $\pm\pi/4$, while if the specific application would require a higher phase accuracy the order of the approximation can be increased. The resulting polynomial approximation of $R(\eta)$ is:

$$\hat{R}_{Cheb}(\eta) = \sum_{k=0}^{n} c_k T_k(\eta) - frac12c_0 + c_1 T_1(\eta) + c_2 T_2(\eta) + c_3 T_3(\eta) + c_4 T_4(\eta) = 8c_4\eta^4 + 4c_3\eta^3 + \eta^2(2c_2 - 8c_4) + \eta(c_1 - 3c_3) - \frac{1}{2}c_0 - c_2 + c_4 \quad (5.1)$$

where $T_i$ are the Chebyshev polynomials of the first kind and $c_i$ are the Chebyshev coefficients computed on the Chebyshev nodes J.Mason [1996]. There are four kind of Chebyshev polynomials and the first kind is used in this work. However all the four kinds of Chebyshev polynomials share the same properties and could be used with similar quality of the approximation Mason [1993].

The coefficients in (5.1) can be grouped as follows:

$$g_0 = -\frac{1}{2}c_0 - c_2 + c_4 \quad g_1 = c_1 - 3c_3$$
$$g_2 = 2c_2 - 8c_4 \quad g_3 = 4c_3 \quad g_4 = 8c_4 \quad (5.2)$$

Now 5.1 can be written as:

$$\hat{R}(\eta)_{Cheb} = g_4\eta^4 + g_3\eta^3 + g_2\eta^2 + g_1\eta + g_0 \tag{5.3}$$

Equation (5.3) is the Chebyshev approximation in polynomial form of the bistatic slant range function. The fundamental difference between this new approximation in (5.3) to that reported in Neo [2007]; Neo et al. [2007] is that the coefficients for the spectrum are now computed starting from the coefficients $g_i$, which are obtained with the Chebyshev approximation rather than the Taylor approximation. The 2D point target spectrum Neo [2007]; Neo et al. [2007] is derived using the formulation in (5.3). Starting from the Fourier transform of the range compressed signal (2.11), in order to obtain the 2D point target spectrum, the principle of stationary phase is applied. In this the approximated version of the slant range function replaces the phase term of the azimuth Fourier transform. This yields a power series expression that links the slow time with the Doppler frequency. Inverting the power series using the method of series reversion produces the desired 2D point target spectrum in accordance with the description in Section 2.5.3.1. The resulting 2D point target spectrum is:

$$S_{2df}(f_\tau, f_\eta) = W_r(f_\tau)W_{az}\left(f_\eta + (f_0 + f_\tau)\frac{g_1}{c}\right)\exp j\Phi_{2df}(f_\tau, f_\eta) \tag{5.4}$$

where

$$\begin{aligned}\Phi_{2df}(f_\tau, f_\eta) \approx &- 2\pi\left(\frac{f_0 + f_\tau}{c}\right)g_0 \\ &+ 2\pi\frac{c}{4g_2(f_0 + f_\tau)}\left(f_\eta + (f_0 + f_\eta)\frac{g_1}{c}\right)^2 \\ &+ 2\pi\frac{c^2 g_3}{8g_2^3(f_0 + f_\tau)^2}\left(f_\eta + (f_0 + f_\eta)\frac{g_1}{c}\right)^3 \\ &+ 2\pi\frac{c^3(9g_3^2 - 4g_2g_4)}{64g_2^5(f_0 + f_\tau)^3}\left(f_\eta + (f_0 + f_\eta)\frac{g_1}{c}\right)^4\end{aligned} \tag{5.5}$$

and $g_i$ ,$i = 0, 2, \cdots, 4$, are the coefficients of the Chebyshev polynomial approximation given in (5.2).

In the proposed approach the computational cost to compute the coefficients $g_i$ is reduced to the evaluation of the slant range function in the Chebyshev nodes and a

sum over $n$ real value multiplication values, where $n$ is the approximation order. The computation of the coefficients in the Taylor based approach are stopped at the $4^{th}$ order. This requires the evaluation of 4 trigonometric functions, 2 square roots and about 60 multiplications, while for the Chebyshev approach the required computations is 8 square roots and about 60 multiplications. For this reason the computational cost of both approaches are comparable. If the order of the approximation is increased the Taylor based approach increases its complexity more than the Chebyshev approach. This is due to the higher number of terms required in the computation of the coefficients. Furthermore considering the computational burden required in the entire image formation process that includes all the Fast Fourier Transforms, matched filters, chirp scaling or range cell migration correction, autofocus, etc. then the time required to approximate the range history is negligible.

## 5.3 Results

Azimuth invariant and azimuth variant configurations are characterized by a fixed or varying baseline between the transmitter or the receiver respectively. Generally it is difficult to keep the configuration azimuth invariant and the case of azimuth variant configurations is the most frequent. In the performance analysis both configurations were simulated. In the first test (azimuth invariant) a point scatterer in the centre of the scene (azimuth sample = 1000, range sample = 182) is simulated. From the two-dimensional spectrum of the range compressed received signal the value of $\Phi_{2df}(f_\tau, f_\eta)$ is compensated obtaining the point target response of the bistatic SAR system. The improvement in the quality using the Chebyshev approach is measured using the Side Lobe Level (SLL), the Peak Side Lobe Ratio (PSLR) and the Integrated Side Lobe Ratio (ISLR). The SLL is defined as the level of the first side lobe while the PSLR and the ISLR are defined as follows:

$$PSLR = 10\log\frac{\text{maximum sidelobe power}}{\text{main lobe power}}$$

$$ISLR = 10\log\frac{\text{total power in sidelobes}}{\text{main lobe power}}$$

The results shown in Table 5.2 are obtained measuring the impulse response in the case of a bistatic azimuth invariant configuration with paramaters given reported in Table 5.1 using the Taylor and Chebyshev coefficients for the 2D phase of the point target spectrum. The results for the range and azimuth gates using the two approaches are

Table 5.1: Bistatic simulations parameters.

| | Azimuth invariant | Azimuth variant |
|---|---|---|
| *Carrier Frequency* | 5 GHz | 5 GHz |
| *PRF* | 1000 Hz | 1000 Hz |
| *Tx Velocity* | 90 m/s | 100 m/s |
| *Rx Velocity* | 90 m/s | 70 m/s |
| *Range distance of the Tx at* $\eta = 0$ | 15000 m | 15000 m |
| *Range distance of the Rx at* $\eta = 0$ | 14500 m | 14500 m |
| *Azimuth distance of the Tx at* $\eta = 0$ | 45 m | 45 m |
| *Azimuth distance of the Rx at* $\eta = 0$ | 80 m | 80 m |
| *Pulse duration* | $6\mu s$ | $6\mu s$ |
| *Range Bandwidth* | 50 MHz | 50 MHz |

shown in Table 5.2. These results show that the proposed approach allows us to ob-

Table 5.2: Measured SLL, PSLR and ISLR values for the azimuth invariant case.

| | **SLL [dBs]** | **PSLR [dBs]** | **ISLR [dBs]** |
|---|---|---|---|
| **Taylor-Range Gate** | -14.14 | -16.54 | -10.99 |
| **Chebyshev-Range Gate** | -14.26 | -16.72 | -11.10 |
| **Taylor-Azimuth Gate** | -13.52 | -16.03 | -10.30 |
| **Chebyshev-Azimuth Gate** | -13.60 | -16.05 | -10.40 |

tain an improvement in the bulk compression in terms of power in the sidelobes. This result is due to the more accurate approximation of the slant range function with the Chebyshev approach leading to a more accurate analytical solution of the point target spectrum. A second simulation is performed using the bistatic azimuth variant configuration as specified in Table 5.1. The first result in Figure 5.1 shows the approximation of the slant range function using the Taylor and the Chebyshev polynomial. The maximum error is of $0.06$ m, while using the Chebyshev approximation the maximum error is $3.63 \times 10^{-11}$ m. These results indicate that the polynomial coefficients obtained with

the Chebyshev approach improve the accuracy of the approximation. This result has a direct impact on the accuracy of the point target spectrum. Figure 5.2 shows the phase

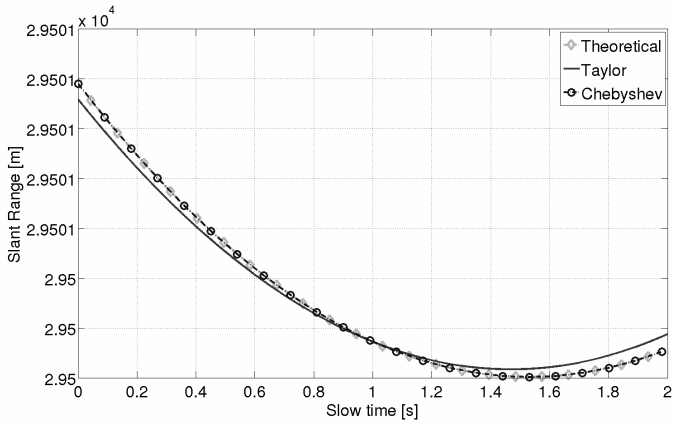


Figure 5.1: Approximations of the slant range function using Taylor and Chebyshev approximation.

error of the point target spectrum using the Taylor and the Chebyshev approximation for the bistatic configuration in Table 5.1. The configuration exhibits a moderate squint angle and the phase error are seen to be reduced by the use of the Chebyshev approximation. This implies that the Chebyshev-based approach is more robust thus facilitating the processing of a wider family of bistatic configurations. The results for the respective impulse responses obtained using this configuration are reported in Table 5.3. In this case the advantage in using the new Chebyshev approximation method approach is more pronounced compared to the azimuth invariant case. In particular in the azimuth direction the power in the mainlobe is observed to be significantly increased when using the Chebyshev approximation. This confirms the capability of the new method in handling shape variations of the slant range function, which are more evident in the azimuth variant configuration.

Table 5.3: Measured SLL, PSLR and ISLR values for the azimuth variant case.

| | **SLL [dBs]** | **PSLR [dBs]** | **ISLR [dBs]** |
|---|---|---|---|
| **Taylor-Range Gate** | -12.30 | -15.40 | -10.21 |
| **Chebyshev-Range Gate** | -14.32 | -18.04 | -12.33 |
| **Taylor-Azimuth Gate** | -13.01 | -15.31 | -9.52 |
| **Chebyshev-Azimuth Gate** | -13.42 | -15.49 | -10.12 |

By increasing the order of the approximation a problem of numerical instability can

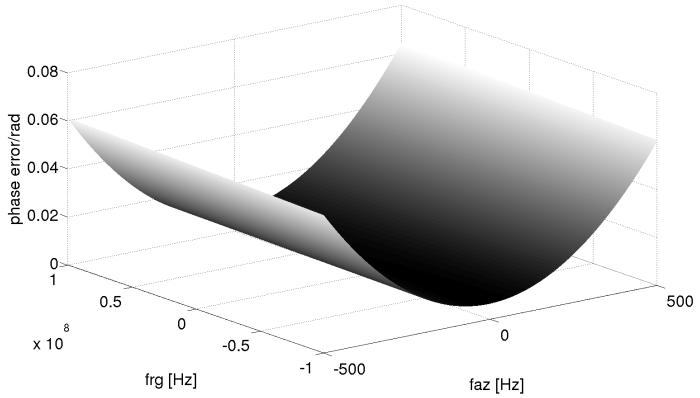


(a) Taylor approximation

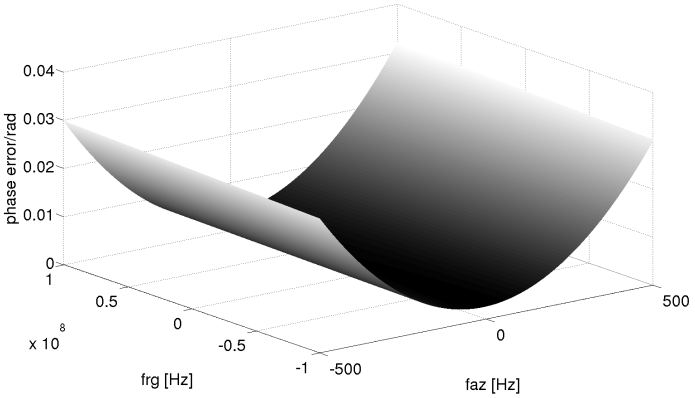


(b) Chebyshev approximation

Figure 5.2: Phase error for the azimuth variant configuration reported in Table 5.1

appear. This is due to the fact that the coefficients of the Chebyshev series become very small. This aspect has also been analyzed through simulations by comparing the perfomances of the Taylor and Chebyshev approximation for different approximation orders. The results of the measured approximation error obtained using the parameters in Table 5.1 are reported in Table 5.4 and Table 5.5: From these results it is evident that increasing the order the Chebyshev approximation reduces the capability to outperform the Taylor series approximation, this aspect is in contrast with the theoretical analysis because of the numerical instability. However the results are still much better than the Taylor series approximation.

Table 5.4: Measured maximum error for approximation order from 1 to 6

| Order | Max Error Taylor [m] | Max Error Chebyshev [m] |
|---|---|---|
| **1** | 0.564 | 0.251 |
| **2** | 0.062 | $2.97e^{-6}$ |
| **3** | 0.062 | $5.859e^{-7}$ |
| **4** | 0.062 | $3.638e^{-11}$ |
| **5** | 0.062 | $4.786e^{-7}$ |
| **6** | 0.062 | $4.786e^{-7}$ |

Table 5.5: Measured standard deviation ($\sigma$) of the error for approximation order from 1 to 6

| Order | $\sigma$ Error Taylor [m] | $\sigma$ Error Chebyshev [m] |
|---|---|---|
| **1** | 0.154 | 0.077 |
| **2** | 0.017 | $7.900e^{-7}$ |
| **3** | 0.017 | $1.806e^{-7}$ |
| **4** | 0.017 | $7.790e^{-12}$ |
| **5** | 0.017 | $1.474e^{-7}$ |
| **6** | 0.017 | $1.474e^{-7}$ |

## 5.4 Approximation of the frequency coupling term for the 2D PSP BTPS

In this section we introduce a similar approach used in Section 5.2 in order to improve the 2D PSP based PTS replacing the Taylor expansion in (2.35). We then approximate (5.6) using the Chebyshev polynomial of the first kind stopping the approximation at the second order as in (2.35):

$$F_R(f) = \sqrt{(f+f_0)^2 - \left(\frac{cf_{\tau_R}}{v_R}\right)^2}$$
$$F_T(f) = \sqrt{(f+f_0)^2 - \left(\frac{cf_{\tau_T}}{v_T}\right)^2} \tag{5.6}$$

$$F_R(f) \approx \sum_{j=1}^{2} g_{jR} T_j(f) - \frac{1}{2} g_{0R} = -\frac{1}{2} g_{0R} + g_{1R} T_1(f) + g_{2R} T_2(f) = \left(-\frac{1}{2} g_{0R} + g_{2R}\right) + g_{1R} f + 2 g_{2R} f^2 = \hat{F}_{0R} + g_{1R} f + 2 g_{2R} f^2$$

$$F_T(f) \approx \sum_{j=1}^{2} g_{jT} T_j(f) - \frac{1}{2} g_{0T} = -\frac{1}{2} g_{0T} + g_{1T} T_1(f) + g_{2T} T_2(f) = \left(-\frac{1}{2} g_{0T} + g_{2T}\right) + g_{1T} f + 2 g_{2T} f^2 \hat{F}_{0T} + g_{1T} f + 2 g_{2T} f^2 \tag{5.7}$$

the Chebyshev coefficients $g_{jR}$ and $g_{jT}$ are computed as:

$$g_{0R} = \frac{1}{3} \sum_{k=0}^{2} F_R(f_k) T_0(f_k) \quad g_{jR} = \frac{2}{3} \sum_{k=0}^{2} F_R(f_k) T_j(f_k)$$

$$g_{0T} = \frac{1}{3} \sum_{k=0}^{2} F_T(f_k) T_0(f_k) \quad g_{jT} = \frac{2}{3} \sum_{k=0}^{2} F_T(f_k) T_j(f_k) \tag{5.8}$$

where $f_k$ are the Chebyshev nodes obtained as:

$$f_k = \frac{f_{min} + f_{max}}{2} - \left[\frac{f_{max} + f_{min}}{2} cos\left(\left(\frac{2k+1}{6}\pi\right)\right)\right] \tag{5.9}$$

with $f_{min}$ and $f_{max}$ representing the maximum and the minimum of the range Doppler spectrum. The term in (2.30) that will be affected from our approximation is the third term $\chi(f, f_\tau) = \pi \left[\frac{R_{0R}}{c} F_R + \frac{R_{0T}}{c} F_T\right]$ , that becomes:

$$\chi(f, f_\tau) \approx 2\pi \left[\frac{R_{0R}}{c} \hat{F}_R + \frac{R_{0T}}{c} \hat{F}_T\right] = 2\pi \left[\frac{R_{0R}}{c} (\hat{F}_0 R + g_{1R} f + 2 g_{2R} f^2) + \frac{R_{0T}}{c} (\hat{F}_{0T} + g_{1T} f + 2 g_{2T} f^2)\right] = \frac{2\pi}{c} (R_{0R} \hat{F}_{0R} + R_{0T} \hat{F}_{0T}) + \frac{2\pi f}{c} (R_{0R} g_{1R} + R_{0T} g_{1T}) + \frac{4\pi f^2}{c} (R_{0R} g_{2R} + R_{0T} g_{2T}) \tag{5.10}$$

From (5.10) the different contributions can be separated and grouped with those remaining from (2.30) as:

$$\begin{aligned}\hat{\Phi}_{RC}(f_\tau, f) =& \frac{\pi f^2}{k_R} + \frac{4\pi f^2}{c}(R_{0R}g_{2R} + R_{0T}g_{2T}) \\ \hat{\Phi}_{AC}(f_\tau, R_{0R}) =& 2\pi(p_{01} + p_{11}R_{0T})k_T f_\tau + \frac{2\pi}{c}(R_{0R}\hat{F}_{0R} + R_{0T}\hat{F}_{0T}) \\ \hat{\Phi}_{RCM}(f_\tau, f) =& \frac{2\pi f}{c}(R_{0R}g_{1R} + R_{0T}g_{1T}) + \bar{\Phi}_{RCM}(f)\end{aligned} \tag{5.11}$$

The resulting bistatic point target spectrum is then :

$$\hat{\Psi}_B(f_\tau, f, R_{0R}) = \hat{\Phi}_{RC}(f_\tau, f) + \hat{\Phi}_{RCM}(f_\tau, f, R_{0R}) + \hat{\Phi}_{AC}(f_\tau, R_{0R}) + \Phi_{AS}(f_\tau) \tag{5.12}$$

In the next section the results on the phase error due to the approximation using Chebyshev and Taylor polynomials for airborne and space-borne configurations are shown.

## 5.5 Results

In this section we present the results obtained simulating both airborne and space-borne bistatic SAR configurations. The results refers to the resulting approximation phase error for Taylor and Chebyshev approaches. In Table 5.6 the two simulated configurations are reported, these configurations are similar to those used in Wang et al. [2011].

Table 5.6: Simulation parameters for the airborne and spaceborne configurations

| | Airborne | | Spaceborne | |
|---|---|---|---|---|
| | Transmitter | Receiver | Transmitter | Receiver |
| Carrier Frequency | 9.65 GHz | | 9.65 GHz | |
| Range Bandwidth | 2 GHz | | 600 MHz | |
| Squint Angles | $0° - 85°$ | | $0° - 45°$ | |
| Velocity | 110 m/s | 100 m/s | 7600 m/s | 7630 m/s |
| $R_0$ | 13.1 km | 23.1 km | 754 km | 666 km |

The phase error for the airborne configuration is shown in Figure 5.3. Figure 5.3-a shows the phase error using the Taylor approximation while Figure 5.3-b shows the phase error using the Chebyshev approximation. The phase error obtained with the Chebyshev polynomial approximation resulted to be smaller than that obtained using

the Taylor polynomial. The maximum error using Chebyshev resulted to be $74.6\%$ less than that using the Taylor polynomial. The average absolute phase error resulted to be of $0.002$ rad for the Taylor case while of $0.0012$ rad for the Chebyshev approximation.

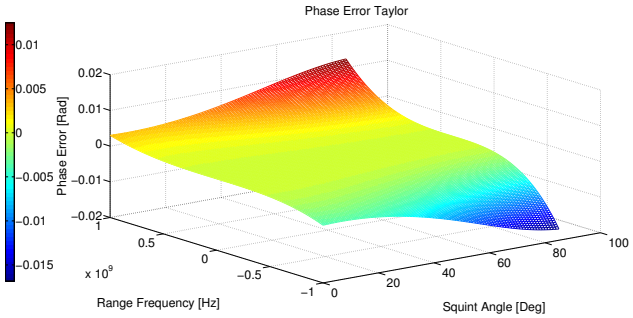


(a)

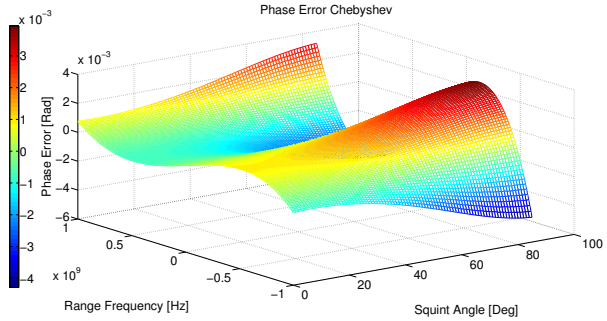


(b)

Figure 5.3: Phase Error for the airborne configuration for the a) Taylor and b) Chebyshev case.

The phase error for the spaceborne configuration is shown in Figure 5.4 Figure 5.4-a shows the phase error using the Taylor approximation while Figure 5.4-b shows the phase error using the Chebyshev approximation. The phase error obtained with the Chebyshev polynomial approximation resulted to be smaller than that obtained using the Taylor polynomial. The maximum error using Chebyshev resulted to be $75\%$ less than that using the Taylor polynomial. The average absolute phase error resulted to be of $4.16 \times 10^{-6} \quad rad$ for the Taylor case while of $2.57 \times 10^{-6} \quad rad$ for the Chebyshev approximation.

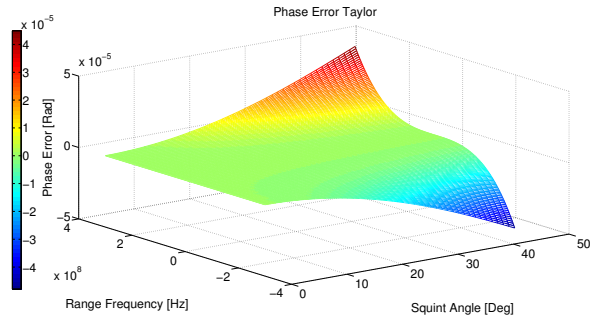


(a)

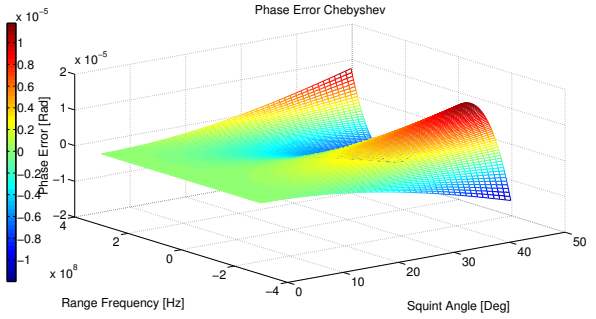


(b)

Figure 5.4: Phase Error for the spaceborne configuration for the a) Taylor and b) Chebyshev case.

With these results we can state that it will be possible to improve the overall accuracy of the bistatic focussing algorithms, in particular monostatic focussing algorithms can be generalized to the bistatic case as in Wang et al. [2011]. The main issue arising from the phase error is the constrain on the amount of data to process at the same time, in order keep an acceptable accuracy in Wang et al. [2011] the processing was constrained to be done in blocks. With our approach this constrain still exists but with the same limit in terms of error bigger blocks can be used thus improving the overall efficiency of the algorithms.

## 5.6 Conclusion

In this chapter a new polynomial Chebyshev approximation of the bistatic slant range function and of the bistatic frequency coupling terms were analytically derived. The proposed approximation is intended to replace the Taylor approximation used in Neo

[2007]; Neo et al. [2007]; Wang et al. [2011] to derive the analytical bistatic point target spectrum. The proposed approximation is easy to compute and does not increase the computational complexity with respect to the Taylor based approach. The approximation error using the Taylor and the Chebyshev polynomials has been evaluated, confirming the theoretical capability of the Chebyshev approach to minimize the norm of the error. However working with such an accurate approximation some numerical instability may occur and this aspect must be considered in the choice of the approximation order.

# Chapter 6

# Micro-Doppler signature analysis in Bistatic SAR

## 6.1 Introduction

Bistatic SAR was introduced in Section 2.5 where its advantages and issues were analysed in detail. The principles of micro-Doppler analysis and the enhances in the radar imaging field have been reviewed in Chapter 3.

To the best of the author's knowledge the study of micro-Doppler signatures from bistatic SAR has not been reported in the literature before and a model for the micro-Doppler signature was not suitable. In this chapter the vibration effect on the received echoes for a bistatic SAR system with fixed receiver is modelled. The pseudo-Wigner Ville distribution (PWVD) is used to analyse simulated data for X-band and mmW systems. The remainder of the chapter is organized as follows. In section II the bistatic SAR geometry and the received signal model are discussed. In section III the micro-Doppler effect from a vibrating target in the bistatic geometry is introduced and analysed, the effect on the focussed image of the bistatic geometry and of the limitations on the system Doppler bandwidth are investigated. Section IV presents simulation results of focussed vibrating target and PWVDs of the received echoes compared with the analytical expected signature and the signature obtained with a monostatic system.

## 6.2 Fixed Receiver Bistatic SAR Geometry

In a bistatic SAR the transmitter and the receiver can have different velocities, altitudes and flight paths, leading to the possibility of having different acquisition configurations. The simplest case is when both transmitter and receiver have the same velocity and parallel flight paths, while a more complicated configuration exists when the platforms have different velocities and non parallel flight paths. In the case of a fixed receiver configuration, only the transmitter is moving and the receiver is fixed. This configuration allows existing monostatic SAR missions to be exploited Duque et al. [2010], in addition the focussing step is easier, permitting an easier and cheaper test bench to validate new techniques to be extended in the more general bistatic configurations. For these reasons we choose to perform the first analysis in the field of the micro-Doppler effect in bistatic SAR for this configurations. The considered bistatic geometry is shown in Figure 6.1.

At the start of the acquisition (slow time $\eta = 0$) the receiver Rx is located in position

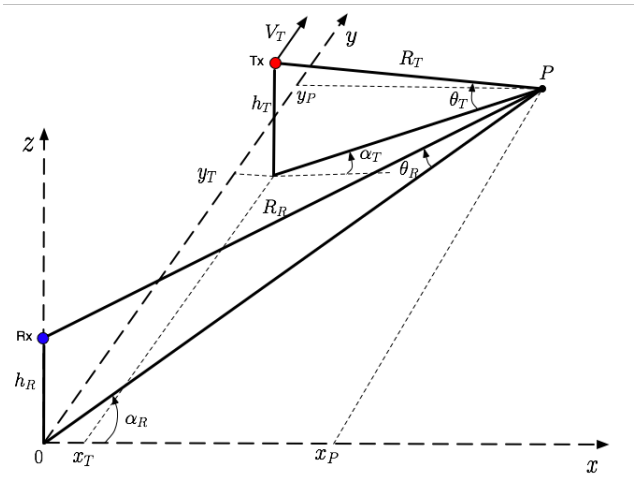


Figure 6.1: Bistatic SAR geometry with fixed receiver

$\{0, 0, h_R\}$ while the transmitter Tx is at $\{x_T, y_T, h_T\}$. A point target $P$ in the centre of the illuminated scene is located in position $\{x_P, y_P, 0\}$. The range component of the slant range between the receiver and $P$ is $X_R = x_p$, while the range component of the slant range between the transmitter and $P$ is $X_T = x_P - x_T$; the azimuth component of the slant range between the receiver and $P$ is $Y_R = y_P$, while the azimuth component of

the slant range at $\eta = 0$ between the transmitter and $P$ is $Y_T = y_P - y_T$. $\theta_R$ and $\theta_T$ represent the depression angles while $\alpha_R$ and $\alpha_T$ are the squint angle for the receiver and the transmitter respectively. The transmitter is moving with velocity $V_T$ in the $y$ direction, because of the null velocity the receiver slant range is $R_R(\eta) = \sqrt{X_R^2 + Y_R^2 + h_R^2}$ while the transmitter slant range is $R_T(\eta) = \sqrt{X_T^2 + (Y_T - \eta V_T)^2 + h_T^2}$, the bistatic slant range history is the sum of the receiver and transmitter slant range histories $R(\eta) = R_T(\eta) + R_R(\eta)$. This is an important factor for the bistatic SAR processing describing the phase history of the received signal.

## 6.3 Micro Doppler effect from vibrating targets in Bistatic SAR

The baseband model of the received bistatic signal from $P$ can be written as Neo [2007]:

$$\begin{aligned} s(\tau, \eta) =& A_0 w_r \left( \tau - \frac{R(\eta)}{c} \right) w_{az}(\eta) \\ & \exp \left\{ -j \frac{2\pi f_0 R(\eta)}{c} + j\pi K_r \left[ \tau - \frac{R(\eta)}{c} \right]^2 \right\} \end{aligned} \tag{6.1}$$

where $\tau$ is the fast time, $A_0$ is the complex backscatterer coefficient, $f_0$ is the carrier frequency $K_r$ is the range chirp rate, $w_r(.)$ is the range envelope and $w_{az}(.)$ is the composite antenna pattern of the transmitter and receiver. The micro-Doppler effect of interest generally exhibits a dynamic of the same order as the slow time, for this reason the micro-motions will not have appreciable effects in the fast time and the range compression of (6.1) can be performed without affecting the analysis. The range compressed signal then results Neo [2007]:

$$s_{rc}(\tau, \eta) = p_r \left( \tau - \frac{R(\eta)}{c} \right) w_{az}(\eta) \exp \left\{ -j \frac{2\pi f_0 R(\eta)}{c} \right\} \tag{6.2}$$

where $p_r(\tau)$ is the range envelope that includes the amplitude factor. The point target $P$ has a micro-motion radial displacement described by $N(\eta)$. For our purpose we are

assuming that the clutter and a possible constant motion of the target were removed using other processing techniques such as a space-time adaptive processing. In real systems it is likely that these effect are not removed completely.

With these assumptions the point target $P$ will still have a displacement described by $N(\eta)$ in the range direction. From Figure 6.1 the slant range history can be written as:

$$\begin{aligned} R(\eta) =& \sqrt{(X_T - N(\eta))^2 + (Y_T - \eta V_T)^2 + h_T^2} + \sqrt{(X_R - N(\eta))^2 + Y_R^2 + h_R^2} \\ =& R_T(\eta) + R_R(\eta) \end{aligned} \tag{6.3}$$

The slant range history is directly related to the phase of the received signal in the azimuth direction:

$$\Phi(\eta) = \frac{2\pi R(\eta)}{\lambda_c} \tag{6.4}$$

where $\lambda_c$ is the carrier wavelength. From the phase history in (6.4) the instantaneous frequency can be obtained. However in order to obtain an explicit expression of the different Doppler frequency components a Taylor series approximation of the slant range is applied, where for orders greater than one, the micro motion effect is assumed to be negligible. The receiver slant range become:

$$\begin{aligned} R_R(\eta) &\approx \sqrt{X_R^2 + Y_R^2 + h_R^2} - \frac{N'(\eta) X_R \eta}{\sqrt{X_R^2 + Y_R^2 + h_R^2}} \\ &\approx R_{0R} - \frac{N'(\eta)\eta X_R}{R_{0R}} \end{aligned} \tag{6.5}$$

While the transmitter slant range can be approximated with:

$$\begin{aligned} R_T(\eta) \approx& \sqrt{X_T^2 + Y_T^2 + h_T^2} - \frac{(N'(\eta)X_T + V_T Y_T)\eta}{\sqrt{X_T^2 + Y_T^2 + h_T^2}} + + \frac{V_T^2 \eta^2}{2\sqrt{X_T^2 + Y_T^2 + h_T^2}} \\ &\approx R_{0T} - \frac{(N'(\eta)X_T + V_T Y_T)\eta}{R_{0T}} + \frac{V_T^2 \eta^2}{2R_{0T}} \end{aligned} \tag{6.6}$$

Using (6.5) and (6.6) the slant range history (6.3) can be written:

$$R(\eta) \approx R_0 - \left( \frac{N'(\eta)X_R}{R_{0R}} + \frac{N'(\eta)X_T}{R_{0T}} \right) \eta - \frac{V_T Y_T \eta}{R_{0T}} + \frac{V_T^2 \eta^2}{2R_{0T}} \tag{6.7}$$

where $R_{0R}$ and $R_{0T}$ are the slant ranges for the receiver and the transmitter at the start of the acquisition, and $R_0 = R_{0R} + R_{0T}$, while $N'(\eta)$ represents the instantaneous micro-velocity of the target and the product $N'(\eta)\eta$ is the instantaneous target micro-displacement $M(\eta)$.

The expression of $R(\eta)$ in (6.7) can be separated into two components, a bistatic SAR component and a target motion component, $R(\eta) \approx R_{BSAR}(\eta) + R_{Target}(\eta)$ where:

$$R_{BSAR}(\eta) = R_0 - \frac{V_T Y_T}{R_{0T}}\eta + \frac{V_T^2 \eta^2}{2R_{0T}} \tag{6.8}$$

$$R_{Target}(\eta) = -\left(\frac{X_R}{R_{0R}} + \frac{X_T}{R_{0T}}\right) M(\eta) \tag{6.9}$$

Also the phase history can be divided into two components:

$$\begin{aligned}\Phi(\eta) =& \frac{2\pi R(\eta)}{\lambda_c} \approx \frac{2\pi(R_{BSAR}(\eta) + R_{Target}(\eta))}{\lambda_c} = \\ & \Phi_{BSAR}(\eta) + \Phi_{Target}(\eta)\end{aligned} \tag{6.10}$$

Using the derivative of (6.10) the instantaneous frequency is obtained as:

$$\begin{aligned}f_D(\eta) =& \frac{1}{2\pi}\frac{d}{d\eta}\Phi(\eta) = \frac{1}{2\pi}\frac{d}{d\eta}\Phi_{BSAR}(\eta) + \frac{1}{2\pi}\frac{d}{d\eta}\Phi_{Target}(\eta) \\ &= \frac{1}{\lambda_c}\frac{d}{d\eta}R_{BSAR}(\eta) + \frac{1}{\lambda_c}\frac{d}{d\eta}R_{Target}(\eta) \\ &= f_{BSAR}(\eta) + f_{MD}(\eta)\end{aligned} \tag{6.11}$$

The instantaneous signal frequency has then two components $f_{BSAR}(\eta)$, a bistatic SAR component and a micro-Doppler component $f_{MD}(\eta)$.

The $f_{BSAR}$ contains the Doppler centroid, the linear and the quadratic modulation term. This term is known from the geometry and does not affect the micro-Doppler frequency. It is not considered further in the analysis.

The explicit form of $f_{MD}(\eta)$ is:

$$f_{MD}(\eta) = -\frac{1}{\lambda_c}\frac{d}{d\eta}\left(\frac{X_R}{R_{0R}} + \frac{X_T}{R_{0T}}\right) M(\eta) \tag{6.12}$$

Considering a point target $P$ vibrating with a vibration:

$$M(\eta) = A_v \cos(w_v \eta) \tag{6.13}$$

where $A_v$ is the amplitude and $w_v$ is the pulsation of the vibration respectively, then the micro-Doppler frequency becomes:

$$\begin{aligned} f_{MD}(\eta) &= -\frac{1}{\lambda_c} A_v \left( \frac{X_R}{R_{0R}} + \frac{X_T}{R_{0T}} \right) \frac{d}{d\eta} \cos(w_v \eta) \\ &= \frac{1}{\lambda_c} A_v w_v \left( \frac{X_R}{R_{0R}} + \frac{X_T}{R_{0T}} \right) \sin(w_v \eta) \end{aligned} \tag{6.14}$$

Referring to Figure 6.1 the relations between the slant ranges and the angles can be written:

$$R_{GT} = \frac{X_T}{\cos(\alpha_T)} = R_{0T} \sin(\theta_T) \Rightarrow \frac{X_T}{R_{0T}} = \sin(\theta_T) \cos(\alpha_T) \tag{6.15}$$

$$R_{GR} = \frac{X_R}{\cos(\alpha_R)} = R_{0R} \sin(\theta_R) \Rightarrow \frac{X_R}{R_{0R}} = \sin(\theta_R) \cos(\alpha_R) \tag{6.16}$$

where $R_{GT}$ and $R_{GR}$ are the ground ranges for the transmitter and the receiver respectively. Equation (6.14) can be written in terms of the squint and depression angles:

$$f_{MD}(\eta) = \frac{1}{\lambda_c} A_v w_v ( \sin(\theta_R) \cos(\alpha_R) + \sin(\theta_T) \cos(\alpha_T)) \sin(w_v \eta) \tag{6.17}$$

Equation (6.17) shows that the micro-Doppler signature depends on the bistatic geometry and is different from the micro-Doppler in the monostatic geometry Ruegg et al. [2007]; Sparr and Krane [2003a]. A bistatic factor that includes the geometry dependence of the micro-Doppler signature can be defined as:

$$\rho = sin(\theta_R) \cos(\alpha_R) + \sin(\theta_T) \cos(\alpha_T) \tag{6.18}$$

Then the micro-Doppler frequency becomes:

$$f_{MD}(\eta) = \frac{1}{\lambda_c} A_v w_v \rho \sin(w_v \eta) \tag{6.19}$$

Equation (6.19) represents the micro-Doppler signature for a bistatic SAR system that is connected to the signature in the monostatic case Ruegg et al. [2007] through the following equation:

$$f_{MD}(\eta) = \frac{f_{MD_{Mono}}(\eta)\rho}{2} \tag{6.20}$$

From (6.20) it can be seen that for $\rho = 2$ the bistatic signature coincides with the monostatic one.

### 6.3.1 Effect on focussing

Using the configuration shown in Table 6.1 an example of the slant range history of a vibrating point target compared with a stationary point target is shown in Figure 6.2. The simulated point target is vibrating with a 10 Hz frequency and a 1 mm amplitude. From Figure 6.2 the effect of the vibration is evident on the range history for such a small amplitude of the vibration. The phase modulation introduced from the vibration

Table 6.1: Simulated bistatic configuration with fixed receiver for the slant range history in Figure 6.2.

| | | |
|---|---|---|
| *Tx Velocity* | 75 | m/s |
| $X_T$ | 1600 | m |
| $X_R$ | 200 | m |
| $Y_T$ | 16 | m |
| $Y_R$ | 200 | m |
| $h_T$ | 1800 | m |
| $h_R$ | 100 | m |
| *Acquisition time* | 0.5 | s |
| *Vibration amplitude* | 0.001 | m |
| *Vibration frequency* | 10 | Hz |

in the signal phase (6.10) introduces the effect known as paired echoes Chen et al. [2006]. The Doppler shift introduced by the vibration creates an infinite number of ghost targets in the focussed image and as in Chen et al. [2006] the received signal may be expanded in a series of Bessel function of the first kind.

$$J_k(B) = \frac{1}{2\pi}\int_{-\pi}^{\pi} e^{j(B\sin w_v\eta - kw_v\eta)} dw_v\eta \tag{6.21}$$

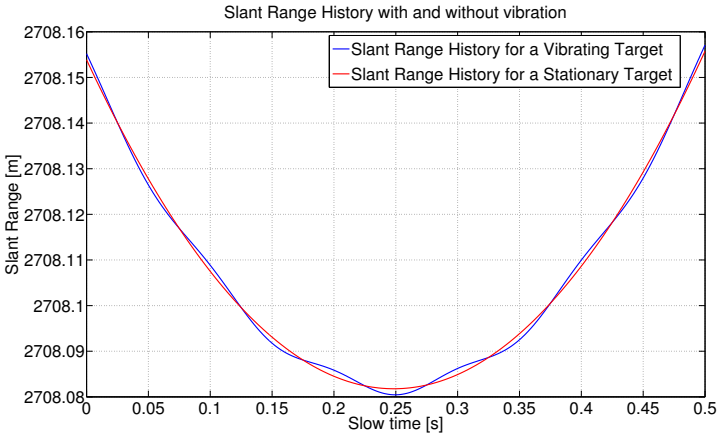


Figure 6.2: Slant range history for a vibrating target and for a stationary target.

where $B = \frac{1}{\lambda_c} A_v(sin(\theta_R)\cos(\alpha_R) + \sin(\theta_T)\cos(\alpha_T))$ and $J_k(B)$ decreases with increasing $k$. Thus the received signal can be written as:

$$s_{rc}(\tau,\eta) = p_r\left(\tau - \frac{R(\eta)}{c}\right) w_{az}(\eta) e^{-j\frac{2\pi f_0 R_{BSAR}(\eta)}{c}} \sum_{k=-\infty}^{\infty} J_k(B) e^{jkw_v\eta} =$$
$$p_r\left(\tau - \frac{R(\eta)}{c}\right) w_{az}(\eta) e^{-j\frac{2\pi f_0 R_{BSAR}(\eta)}{c}} [J_0(B) + J_1(B)e^{jw_v\eta} - J_1(B)e^{-jw_v\eta}$$
$$+ J_2(B)e^{j2w_v\eta} + J_2(B)e^{-j2w_v\eta} + J_3(B)e^{j3w_v\eta} - J_3(B)e^{-j3w_v\eta} + \cdots] \quad (6.22)$$

Unlike Chen et al. [2006] the amplitude factor of the ghost scatterers, represented by $J_k(B)$, depends on the bistatic SAR geometry. Thus depending on the particular geometry the effect on the focussed image of a particular vibrating target will be more or less evident.

### 6.3.2 Effect of the bistatic factor

In this section the effect of the bistatic configuration on the amplitude values of the induced micro-Doppler is analysed. The amplitude of the vibration can be obtained from the measured maximum of the micro Doppler signature using (6.19) as:

$$A_v = \frac{\lambda_c \max(f_{MD}(\eta))}{w_v \rho} \quad (6.23)$$

The difference between (6.23) and that in Ruegg et al. [2007] for the monostatic case is the dependence on the bistatic factor $\rho$. This dependence must be considered in the micro Doppler signature analysis in order to correctly identify the amplitude of the vibration. Different acquisition geometries induce different micro-Doppler amplitudes and thus a good knowledge of the geometry is required in order to obtain the amplitude of the vibration. In Figure 6.4-a and in Figure 6.4-b the theoretical bistatic maximum of the micro-Doppler signature for a 94 GHz and a 10 GHz system respectively for a vibrating target with $w_v = 20\pi$ rad/sec and a vibration amplitude from 0.1 mm to 10 mm are shown. The amplitude of the micro-Doppler signature depends also on the vibrating frequency $w_v$ as can be seen in (6.23). In Figures 6.5-a and 6.5-b the theoretical bistatic maximum of the micro-Doppler signature with a 94 GHz and a 10 GHz system for a vibrating target with 1 mm of vibrating amplitude and with a vibrating frequency from 1 Hz to 100 Hz are shown. For both cases the bistatic factor influences the amplitude of the micro-Doppler signature. This factor is the sum of the conic angle of the transmitter and receiver and therefore is dependent on the BSAR geometry. From both Figures 6.4 and 6.5 the bistatic factor influences the amplitude of the micro-Doppler signature, when $\rho = 2$ the curves assumes the maximum values and they coincide with the maximum micro-Doppler obtained in a monostatic case. This aspect must be considered because a certain amplitude of the micro-Doppler signature corresponds to a family of vibrating amplitudes. The correct amplitude can be obtained only with the knowledge of the bistatic factor. In addition the amplitude is also influenced by the carrier frequency. For example a 10 GHz system would not be able to detect micro-Doppler signatures generated by very small motions. Furthermore larger micro-motions will introduce aliasing if not correctly sampled in a 94 GHz system. For this reason this is an important aspect in the design and the choice of the measurement system. The bistatic factor offers an advantage in the use of a bistatic configuration with respect to the monostatic configuration for larger vibration frequencies and amplitudes. From (6.19) it is seen that the bistatic factor reduces the amplitude of the micro-Doppler signature compared with the one obtained for the same vibration in the monostatic case. This means that for vibrations introducing high Doppler shifts, running over the azimuth Doppler bandwidth in the monostatic case, the analysis of

the signature can suffer from aliasing. However as the use of a bistatic configuration reduces the micro-Doppler amplitude it is possible to keep the signature inside the azimuth Doppler bandwidth. This means that it is possible to use a smaller minimum PRF to avoid aliasing in the analysis compared to the monostatic configuration.

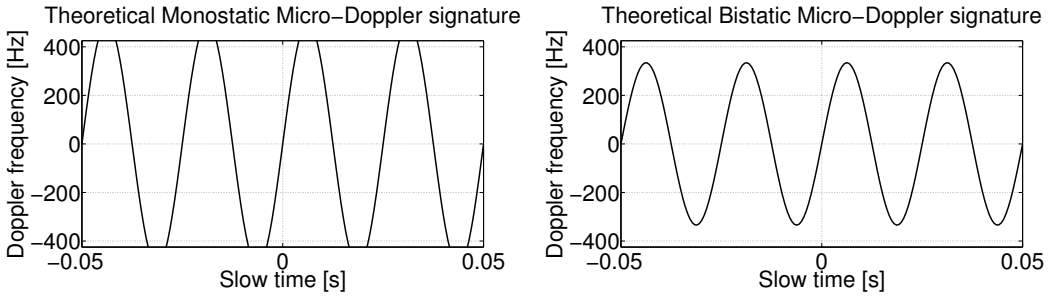


(a) (b)

Figure 6.3: Theoretical micro-Doppler signature for a target vibrating at 40 Hz wiht 3 cm of amplitude from a X band system with 950 Hz of azimuth Doppler bandwidth, a) monostatic case running over the azimuth Doppler bandwidth, b) bistatic case with the entire signature visible in the azimuth Doppler bandwidth.

Figure 6.3 shows an example of a bistatic configuration for the analysis in X-band of a 40 Hz vibrating target with 3 cm of vibrating amplitude. In Figure 6.3-a the monostatic micro-Doppler signature runs over the limit given by the Doppler bandwidth making the analysis of the signature impossible, while Figure 6.3-b shows the same vibration analysed from a bistatic system. In this case the bistatic factor $\rho$ is weighting the micro-Doppler signature, keeping it inside the Doppler bandwidth.

## 6.4 Simulation Results

Vibrating targets were simulated and their micro-Doppler signatures from a bistatic SAR system analysed. First the effect of the vibration on the focussed image is shown. The different micro-Doppler signatures are then analysed for different bistatic configurations for systems working with a carrier frequency of 10 GHz and 94 GHz. The two frequencies were chosen because theoretically they produce results that demonstrate that it is possible to detect micro-Doppler signatures of interest such as engines and humans. In addition X-band radar are very common Ender and Brenner [2003];

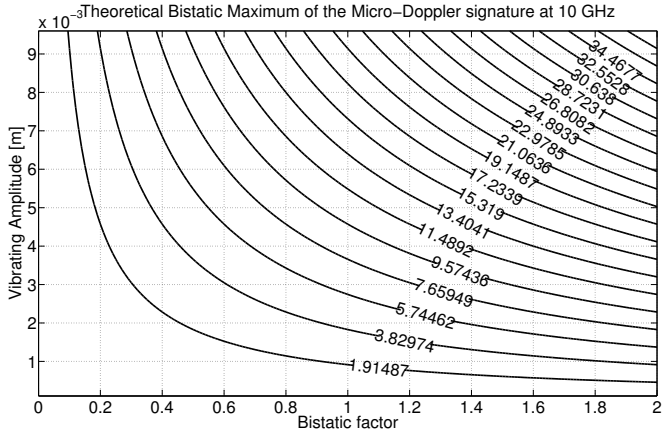


(a)

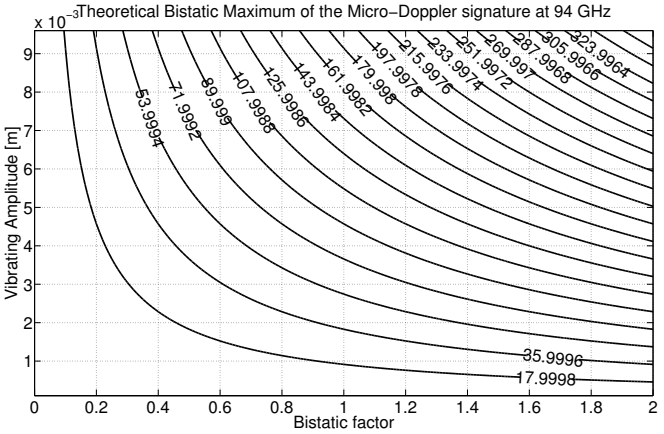


(b)

Figure 6.4: Maximum amplitude of the micro Doppler frequency shift for different bistatic configurations for a vibrating target with a vibrating frequency of 10 Hz and vibrating amplitudes from 0.1 mm to 10 mm . a) micro Doppler for a 10 GHz system b) micro Doppler for a 94 GHz system. The micro Doppler is increasing with the increasing vibrating amplitude and bistatic factor.

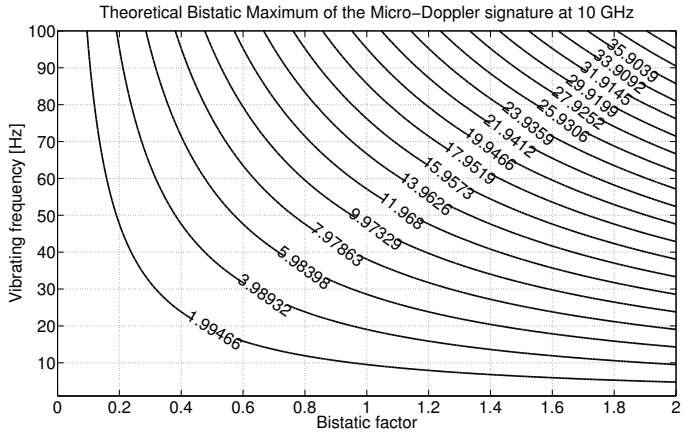


(a)

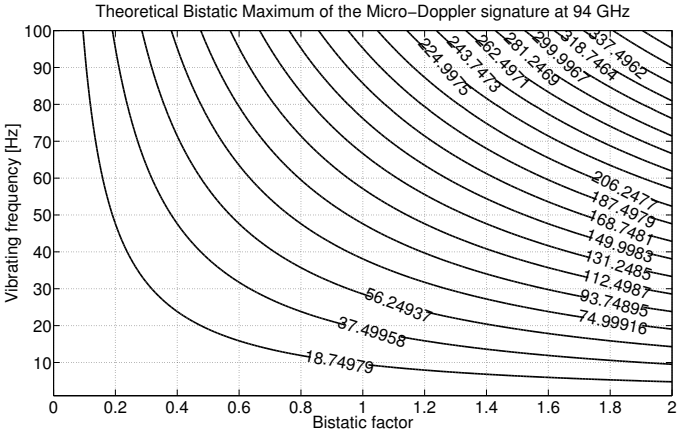


(b)

Figure 6.5: Maximum amplitude of the micro Doppler frequency shift for different bistatic configurations for a vibrating target with a vibrating amplitude of 1 mm and vibrating frequencies from 1 Hz to 100 Hz. a) micro Doppler for a 10 GHz system b) micro Doppler for a 94 GHz system. The micro Doppler is increasing with the increasing vibrating frequency and bistatic factor.

Kinghorn and Nejman [2009] and some 94 GHz radar are operational like MEMPHIS Schimpf et al. [2002].

### 6.4.1 Effect on focussing

The result of bistatic focussing for two different configurations with transmitter altitudes of 2100 m and 900 m are shown for a 94 GHz system in Figure 6.6-a and Figure 6.6-b respectively. These two altitudes were chosen to highlight the effect of the different geometry on the focussed image. The simulated point target is vibrating at 10 Hz with an amplitude of 0.5 mm. The resulting focussed images in both cases show the presence of ghost scatterers along the azimuth direction on both sides of the point scatterer. However the same vibration exhibits a different number of ghost scatterers with different amplitudes for both configurations. This aspect can be analysed and confirmed using the discussion in Section 6.3.1. For the first configuration, Figure 6.6-a, the bistatic scale factor is $1.0143$ and the value of $B$ in (6.22) is $0.9984$, while in the simulation shown in Figure 6.6-b the bistatic scale factor is $1.5382$ and $B = 1.5141$. With these values the Bessel function of the first kind $J_k(B)$ can be computed for both configurations. These values are weighting the amplitude of the scatterer and the ghost scatterers. The computed values of the first four orders of $J_k(B)$ for the two configurations are shown in Table 6.2. The values of $J_k(B)$ in Table 6.2 confirm that for

Table 6.2: Computed values of the $1^{st}$ kind Bessel function for the two configurations.

| **Order of $J_k(B)$** | **Config. (a)** | **Config. (b)** |
|---|---|---|
| 0 | 0.7659 | 0.5039 |
| 1 | 0.4395 | 0.5599 |
| 2 | 0.1146 | 0.2356 |
| 3 | 0.0195 | 0.0625 |

the configuration simulated in Figure 6.6-a the amplitude of the real point scatterer is higher than those for the ghost scatterers pairs while for the configuration in Figure 6.6-b the amplitude of the ghost scatterers is greater than the real point scatterers for the first pair of ghosts.

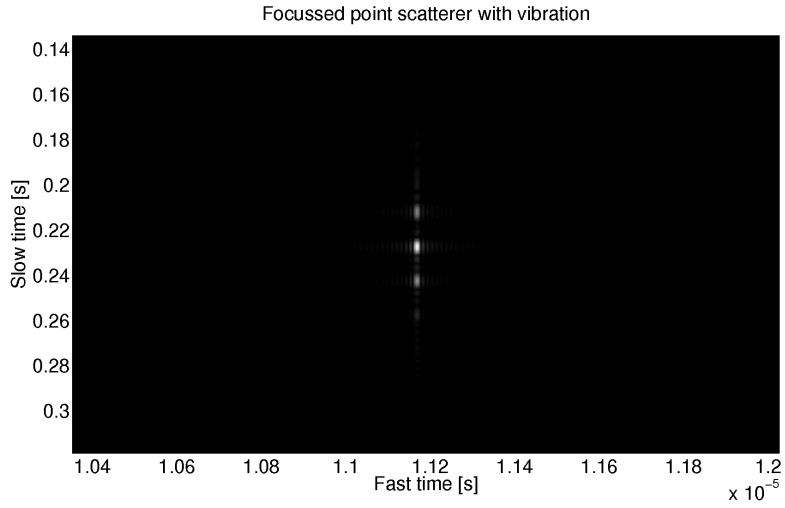


(a)

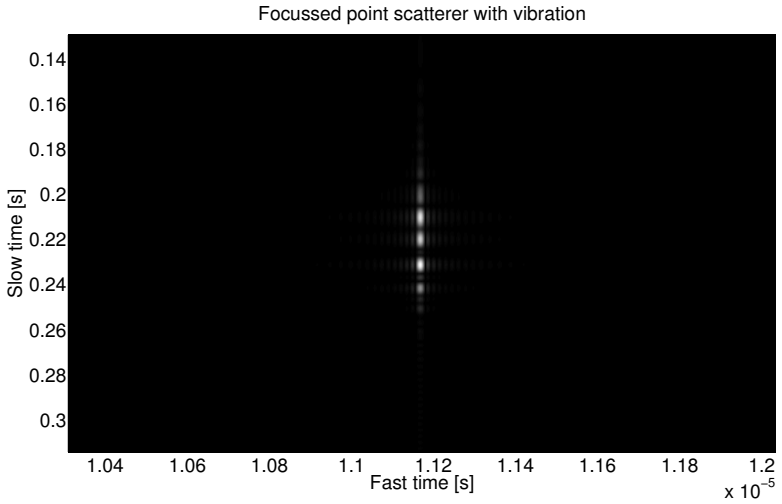


(b)

Figure 6.6: Focussed point targets in a bistatic SAR system with fixed receiver. The vibrating amplitude is 0.5 mm and the vibration frequency is 10 Hz. a) transmitter at 2100 m , b) transmitter at 900 m.

### 6.4.2 Micro-Doppler signature analysis from simulated data

Figure 6.7 shows a block diagram of the steps needed to perform the time-frequency analysis of the micro-Doppler signature for a bistatic SAR with fixed receiver. Starting

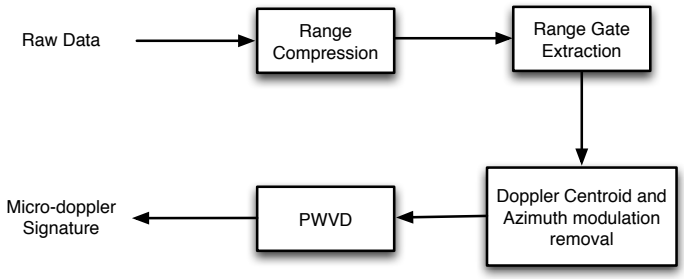


Figure 6.7: Steps for the extraction of the micro-Doppler signature from the simulated data

from the raw data the range compression step is performed using a replica of the transmitted signal. From the range compressed data the range gate containing the scatterer is selected. For the configurations analysed in this chapter the range migration is contained within a fraction of the resolution cell, however in the presence of a larger range migration a range cell migration correction Cumming and Wong [2005] step can be performed before the extraction of the range gate.

In order to align the signal within the time-frequency plane to obtain a correct visualization and positioning of the time-frequency distribution, the Doppler centroid and the azimuth frequency slope is removed from the signal before the computation of the Pseudo Wigner Ville Distribution (PWVD) Cohen [1989], which is used to extract the micro-Doppler signature of the target. Using this analysis procedure, vibrating targets in Bistatic SAR configurations with 10 GHz and 94 GHz systems were analysed and compared with the results obtained using a monostatic configuration and the theoretical micro-Doppler. Figure 6.8 shows the PWVDs of the received SAR signal for a 94 GHz system for a point target vibrating at 10 Hz with an amplitude of the vibration of 1 mm. Figures 6.8-a and -c show the PWVD obtained with the two bistatic configurations in Table 6.3, while Figure 6.8-e shows the PWVD in the monostatic case for the same target. Figures 6.8-b, -d and -f show the theoretical micro-Doppler signature for the cases analysed in Figure 6.8-a, -c and -e respectively. Table 6.3 gives

the two bistatic configurations and the monostatic configuration used in the simulation shown in Figure 6.8. It can be seen that the only difference resides in the geometry, and therefore the bistatic factor that influences the micro-Doppler signature.

Table 6.3: Simulated bistatic configurations for the simulated target in Figure 6.8.

| | Configuration 1 | Configuration 2 | Monostatic |
|---|---|---|---|
| Carrier Frequency | 94 GHz | 94 GHz | 94 GHz |
| Tx Velocity | 75 m/s | 75 m/s | 75 m/s |
| Acquisition Time | 0.5 s | 0.5 s | 0.5 s |
| Vibration Amplitude | 0.001 m | 0.001 m | 0.001 m |
| Vibration Frequency | 10 Hz | 10 Hz | 10 Hz |
| $X_T$ | 1600 m | 1600 m | - |
| $Y_T$ | 19 m | 19 m | - |
| $h_T$ | 1800 m | 1800 m | - |
| $X_R$ | 200 m | 600 m | - |
| $Y_R$ | 200 m | 200 m | - |
| $h_R$ | 100 m | 100 m | - |
| **Bistatic Factor** | **1.3310** | **1.6014** | **2** |

From Figure 6.8 it is confirmed that the analysed bistatic micro-Doppler signatures match those expected from theory. The frequency of the vibration can be measured by inspection the PWVDs confirming the 10 Hz simulated vibration. The measured micro-Doppler amplitude for the first configuration is 26 Hz. Equation (6.23) yields an estimated vibrating amplitude of $9.9985 \times 10^{-4}$ m which is close to the simulated 1 mm vibration amplitude. This is confirmed using the maximum of the theoretical micro-Doppler of 26.2 Hz obtained using (6.19). In the second configuration the measured micro-Doppler amplitude is 32 Hz yielding an estimated vibration amplitude of $1.01 \times 10^{-3}$ m. The original 1 mm amplitude can be obtained from the maximum of the theoretical micro-Doppler that is 31.5 Hz. As expected both the bistatic micro-Doppler exhibits a maximum of the micro-Doppler signature smaller than the monostatic case which is of 39.37 Hz.

Figure 6.9 shows the PWVDs of the received SAR signal for a 10 GHz system for a point target vibrating at 5 Hz with an amplitude of the vibration of 0.1 m. Figures 6.9-a and -c show the PWVD obtained with the two bistatic configurations in Table 6.4, while Figure 6.9-e shows the PWVD in the monostatic case for the same target. Figures 6.9-b, -d and -f show the theoretical micro Doppler signature for the cases analysed in

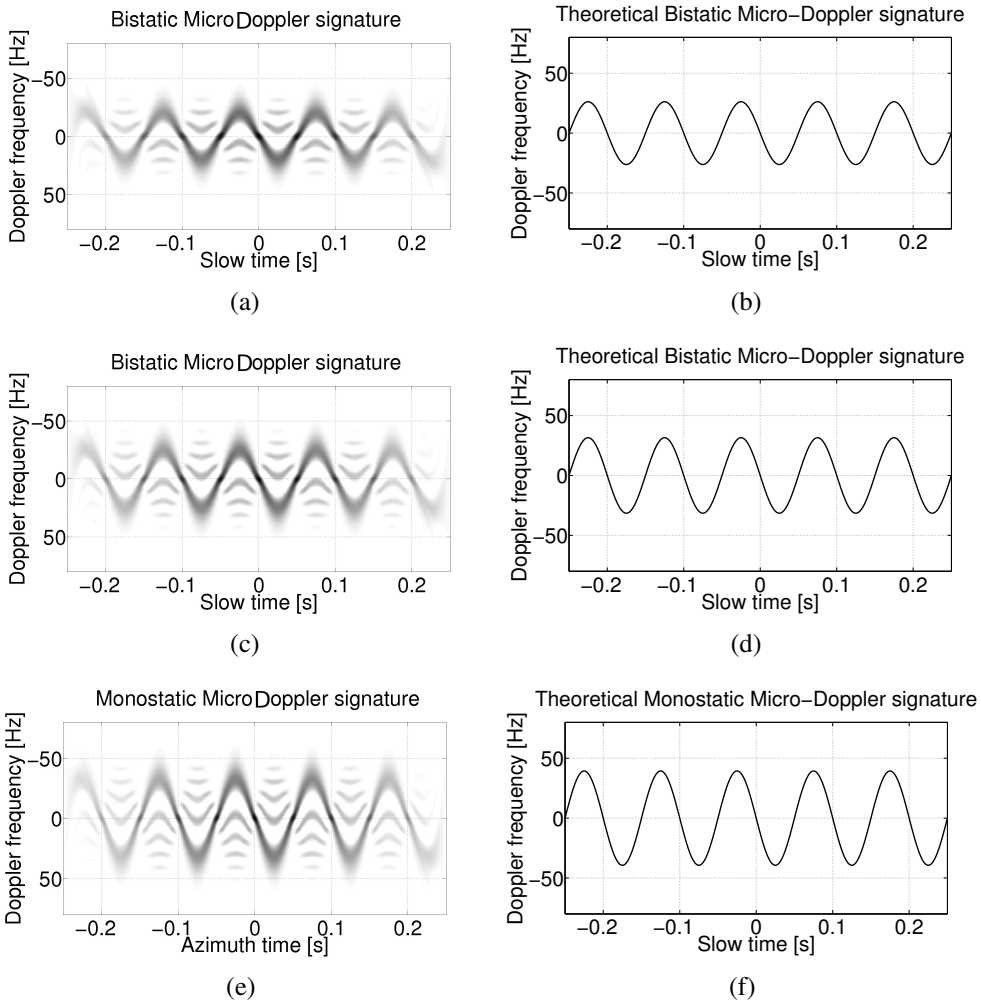


Figure 6.8: Micro-Doppler signatures of a vibrating target with 10 Hz of vibration and 1 mm of amplitude on a 94 GHz system. a) and c) shows the analysed PWVD of the two bistatic configurations shown in Table 6.3 while e) shows the micro-Doppler signature in the monostatic case. b) , d) and f) shows the theoretical signature for a), c) and e) respectively.

Figure 6.9-a, -c and -e respectively. Table 6.4 reports the two bistatic configurations and the monostatic configuration used in the simulation shown in Figure 6.9. Figure

Table 6.4: Simulated bistatic configurations for the simulated target in Figure 6.9.

| | Configuration 1 | Configuration 2 | Monostatic |
|---|---|---|---|
| *Carrier Frequency* | 10 GHz | 10 GHz | 10 GHz |
| *Tx Velocity* | 75 m/s | 75 m/s | 75 m/s |
| *Acquisition Time* | 0.5 s | 0.5 s | 0.5 s |
| *Vibration Amplitude* | 0.1 m | 0.1 m | 0.1 m |
| *VibrationFrequency* | 5 Hz | 5 Hz | 5 Hz |
| $X_T$ | 1600 m | 1600 m | - |
| $Y_T$ | 19 m | 19 m | - |
| $h_T$ | 1800 m | 2800 m | - |
| $X_R$ | 200 m | 600 m | - |
| $Y_R$ | 200 m | 200 m | - |
| $h_R$ | 100 m | 100 m | - |
| ***Bistatic Factor*** | **1.3310** | **1.1627** | **2** |

6.9 show the results for the 10 GHz simulations. The measured micro-Doppler amplitude for the first configuration is 140 Hz yielding an estimated vibrating amplitude of 0.1004 m from (6.23). This is close to the simulated 0.1 m vibration amplitude and confirmed using the maximum of the theoretical micro-Doppler of 139.38 Hz obtained using (6.19). In the second configuration the measured micro-Doppler amplitude is 125 Hz, yielding an estimated vibration amplitude of 0.102 m. The original 0.1 m amplitude is computed from the maximum of the theoretical micro-Doppler amplitude that is 121.76 Hz. The maximum amplitude of the micro-Doppler in the monostatic case which is of 209.43 Hz. These results demonstrate that the micro-Doppler signature for a specific configuration changes with the bistatic acquisition geometry. This is an important factor to be considered in the classification and recognition of targets characterized by a particular micro-Doppler signature. In addition (6.20) can be used to exploit existing micro-Doppler signatures in a bistatic environment.

## 6.5 Conclusion

In this chapter the micro-Doppler signatures from vibrating targets in bistatic SAR systems were investigated. The bistatic configuration with a fixed receiver was used

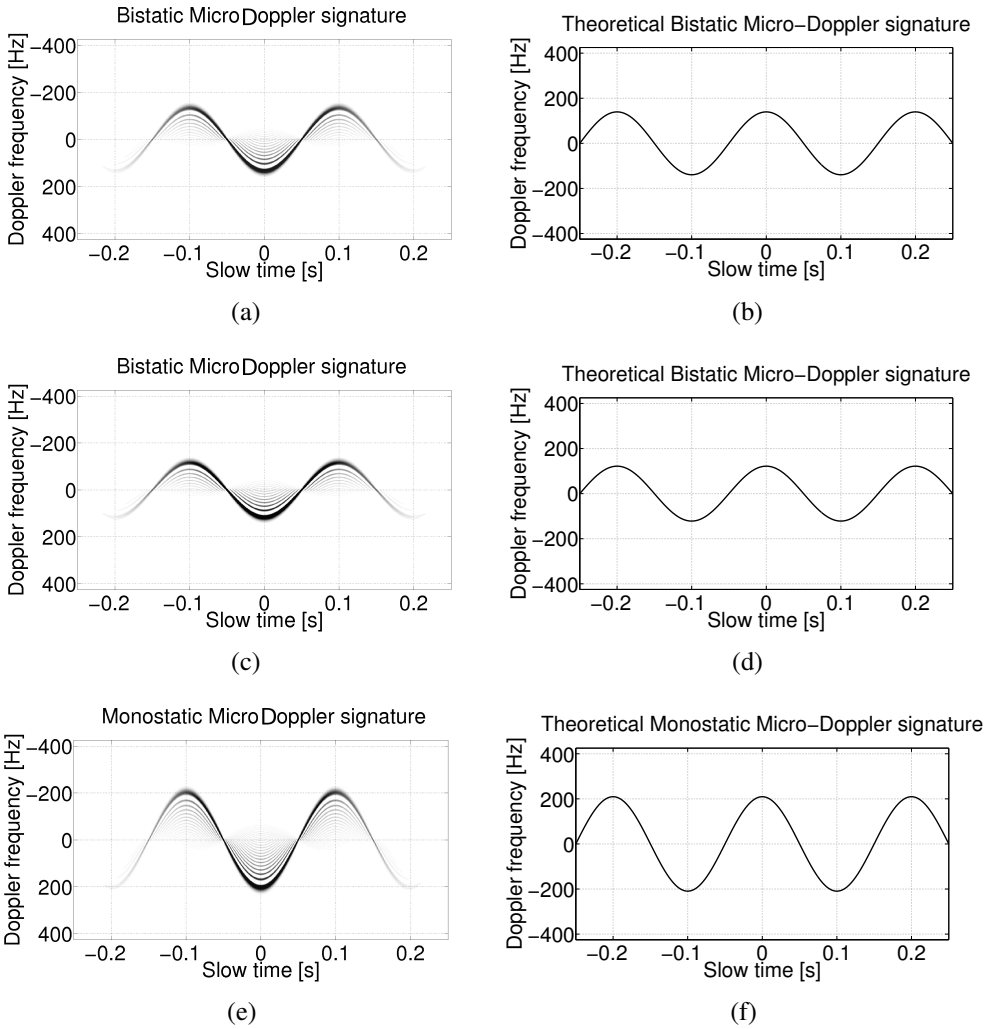


Figure 6.9: Micro Doppler signatures of a vibrating target with 5 Hz of vibration and 0.1 m of amplitude on a 10 GHz system. a) and c) shows the analysed PWVD of the two bistatic configurations shown in Table 6.4 while e) shows the micro Doppler signature in the monostatic case. b) , d) and f) shows the theoretical signature for a), c) and e) respectively.

to derive an expression for the bistatic micro Doppler signature. The effect on the focussed image was also analysed. The bistatic case shows a substantial difference to that of the traditional monostatic case. The bistatic micro Doppler signature is influenced by the bistatic geometry. Vibrating targets were simulated to confirm the theoretical analysis on the focussed image and on the micro-Doppler signatures. The simulations confirmed the model that provides a useful tool for the analysis of the micro-Doppler signature from a bistatic SAR system. The effect of the bistatic factor must be considered for target classification and recognition.

It was demonstrated that the bistatic configuration exhibits the advantage of a reduced minimum required PRF compared to that required in the monostatic SAR. Furthermore this reduces the effects of potential aliasing in the analysis of the micro-Doppler signature compared to the monostatic case. It was shown that this is due to the effect of the bistatic geometry on the maximum amplitude of the micro-Doppler signature that is seen to be equal or less to the amplitude of the micro-Doppler signature in the monostatic case. Thus for a family of micro-Doppler effects and a fixed PRF the analysis from a monostatic geometry will appear aliased while the use of a bistatic configuration could prevent aliasing. Thus the bistatic configuration facilitates the analysis of a wider range of signatures with respect to the monostatic system.

# Chapter 7

# GNSS Based Passive Bistatic Radar for Micro-Doppler analysis

## 7.1 Introduction

The alternative use of the Global Navigation Satellite System (GNSS) has recently initiated a number of studies that aim to exploit this system as an illuminator of opportunity for a passive radar system. The study of possible secondary applications of the Global Navigation Satellite System (GNSS) has lead to several remote sensing applications Cherniakov [2008]; Gleason and Gebre-Egziabher [2009]. Interest in exploiting GNSS for remote sensing is growing recently due to the advantage offered by its high coverage in time of the entire earth.

In this chapter a Passive Bistatic Radar configuration using a GNSS as illuminator in near forward scattering zone for micro-Doppler analysis is proposed.

We investigate the possibility of exploiting the GNSS signal in a Passive Bistatic Radar system when a target is in the near forward scattering zone for micro-Doppler analysis. The feasibility study will first deal with the restrictions of the GNSS system in terms of available pulse rate frequency (PRF) that can form a limitation for the maximum Doppler shift to be analysed correctly. It will be shown that as a result of using the 1.5 GHz GNSS signal in a bistatic configuration, the maximum micro-Doppler shift from the rotating blades is reduced thus allowing the time frequency analysis with the standard GNSS PRF of 1 kHz without aliasing. In addition the ambiguity function for

the used waveform will be discussed. The second aspect to analyse is the power budget of the received echoes to the receiver from this kind of target. The budget is presented and it is shown that exploiting the forward scattering enhancement will allow us to obtain sufficient forward scattered power to detect the echoes from the rotor blades within certain ranges reducing also the effect of the Direct Signal Interference.
The remainder of this chapter is organized as follows. Section 2 introduces the passive bistatic radar GNSS geometry, and the signal model. Section 3 analyses the micro-Doppler effect from helicopters rotor blades in radar and Section 4 analyses the system requirements to correctly perform the micro-Doppler analysis of rotor blades. Section 5 introduces the forward scattering enhancement concept with a particular attention to the case of the rotor blades, while in section 6 the budget analysis for the proposed system and for the micro-Doppler analysis purpose is performed. Section 7 introduces the processing method to obtain the micro-Doppler signature of the rotating blades. Results of simulations are included for different helicopters.

## 7.2 Bistatic GNSS radar system geometry and signal model

The acquisition geometry of the proposed bistatic passive radar system is shown in Figure 7.1. The transmitter is one of the assumed GNSS transmitters flying over the the receiver. $R_T$ and $R_R$ are the transmitter to target and the receiver to target ranges respectively. The angle $\beta$ is the solid bistatic angle defined as the angle between the transmitter, the target and the receiver Willis [1995].

The principal transmitted signal from the GNSS satellite is a Code Division Multiple Access code consisting of a Pseudo Random Noise (PRN) sequence called C/A code. We will concentrate on the case of the GPS constellation and will consider the $L1$ signal at $1.5$ GHz. Each satellite can be identified based on the specific C/A sequence which exhibits a very narrow cross-correlation function allowing the system to measure the time delay between the satellite platform and the GPS receiver.
The same principle can be exploited to perform target ranging when a target scatters the signal coming from the GPS satellite to a receiver located on ground or on an aircraft.

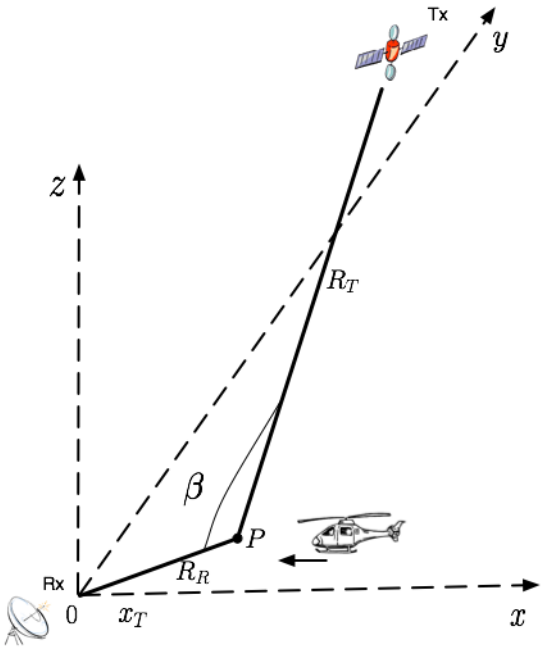


Figure 7.1: Proposed bistatic passive radar geometry with the GNSS illuminator.

The relative delay between the reference signal, obtained as the direct signal from the satellite at the receiver on a different antenna and the scattered echo from the target can be estimated. We assume that the direct signal at the receiving antenna used to perform ranging has been attenuated through physical shielding, digital beamforming or DSP techniques Howland et al. [2008]; Willis [1995].

The received radar return after the cross-correlation with the replica of the PRN signal can be modelled as Skolnik [1981]:

$$s_{rc}(\tau,\eta) = A_0 p_r\left(\tau - \frac{R_R(\eta)}{c}\right)\exp\left\{-j\frac{2\pi f_0 R(\eta)}{c}\right\} \tag{7.1}$$

where $f_0$ is the carrier frequency, $c$ is the speed of light, $p_r(\tau)$ is the range envelope where the time reference is triggered to the direct signal received from the transmitter, $A$ is the amplitude of the scattered signal, $\tau$ is the variable representing the *fast* time of the received signal, while $\eta$ represents the *slow* time of the acquisition of the different echoed PRN sequences and $R(\eta)$ is the bistatic target range. This *slow* time is required because the dynamics of the micro-motion are slower than the dynamics of the signal used to perform ranging. This is also the reason why the cross-correlation of the C/A sequence can be performed without affecting the micro-Doppler analysis. However

the signal model requires to be modified in the presence of target micro-motions where phase modulation of the signal is introduced. This aspect will be analysed in the next section.

## 7.3 Micro-Doppler from a helicopter's rotor blades

In the application considered in this work the receiver is a platform on ground. This kind of configuration allows us to obtain easily a near forward scattering configuration. The target is a helicopter approaching the Line Of Sight (LOS) between the transmitter and the receiver. It means that the bistatic angle $\beta$ is close to $180°$ where forward scattering enhancement can be obtained Willis [1995].

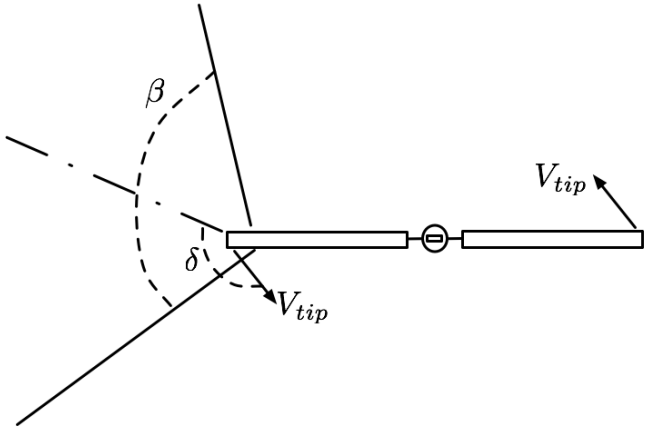


Figure 7.2: Geometry of the rotating blades seen from the bistatic radar.

Figure 7.2 shows a top view of the geometry of the rotor blades relative to the bistatic geometry. The rotating plane of the rotor blade is parallel to the ground and quasi-orthogonal to the line of sight between the transmitter and the receiver. $\mathbf{V_{tip}}$ is the velocity vector of the tip of the rotor blade and $\delta$ is the angle between $\mathbf{V_{tip}}$ and the bisector of the bistatic angle $\beta$. The angles $\beta$ and $\delta$ are two important factors that influences the micro-Doppler signature of the target in a bistatic geometry Chen [2011]. The model of the received signal in (7.1) must consider also the effect of the micro-motion as follows:

$$s_{rc}(\tau,\eta) = A_1(\eta)p_r\left(\tau - \frac{R_R(\eta)}{c}\right)\exp\left\{-j(\Phi_R(\eta)+\Phi_{mD}(\eta))\right\} \tag{7.2}$$

where $\Phi_R = 2\pi f_0 R(\eta)/c$ is the phase of the target containing the constant motion and $\Phi_{mD}(\eta)$ is the phase modulation due to the micro-motions of the target and can be expressed as Chen [2011]:

$$\Phi_{mD}(\eta) = -\frac{2\pi}{\lambda}\frac{L_b}{2}\cos\left(\frac{\beta}{2}\right)\cos(\delta)\cos(\mathbf{\Omega}\eta + \theta_0) \tag{7.3}$$

where $L_b$ is the length of the rotor blade, $\mathbf{\Omega}$ is the angular rotation rate and $\theta_0$ is the initial rotating phase. The product $\cos\left(\frac{\beta}{2}\right)\cos(\delta)$ is the factor that takes into consideration the bistatic geometry Chen [2011].

The amplitude of the received echo is also affected by the rotation of the blade and may be written as:

$$A_1(\eta) = A_0 sinc\left(\frac{2\pi}{\lambda}\frac{L_b}{2}\cos\left(\frac{\beta}{2}\right)\cos(\delta)\cos(\mathbf{\Omega}\eta + \theta_0)\right) \tag{7.4}$$

Assuming that a rotor has $N$ blades, they will have $N$ different initial phases $\theta_k = \theta_0 + k2\pi/N$ with $k = 0, 1, 2, ..., N-1$. The total received signal from the $N$ blades will be the sum of the modulated signal from each blade, from (7.2), (7.3) and (7.4) it can be written as:

$$s_{tot}(\tau, \eta) = \sum_{k=0}^{N-1} A_{1_k}(\eta) p_r\left(\tau - \frac{R(\eta)}{c}\right)\exp\left\{-j(\Phi_R(\eta) + \Phi_{mD_k}(\eta))\right\} \tag{7.5}$$

The expression (7.5) is similar to the signal model in Chen [2011] but it is adapted for the specific proposed system. The micro-Doppler shift can be obtained for each blade from (7.3) as:

$$\begin{aligned} f_{mD_k}(\eta) =& \frac{1}{4\pi}\frac{d}{d\eta}\Phi_{mD}(\eta) = \frac{L_b}{2\lambda}\mathbf{\Omega}\cos\left(\frac{\beta}{2}\right)\cos(\delta)[-\sin(\theta_k)\sin(\mathbf{\Omega}\eta) + \\ &+ \cos(\theta_k)\cos(\mathbf{\Omega}\eta)] \end{aligned} \tag{7.6}$$

Equation (7.6) represents the expression of the expected micro-Doppler signature for a rotor blade of an helicopter of length $L_b$ with a rotation rate $\mathbf{\Omega}$, it can be used then to obtain the features of the rotating blade from the micro-Doppler signature.

## 7.4 System requirements for m-D analysis

In a passive system with an illuminator of opportunity as GPS the carrier frequency and the sampling rate cannot be modified. These can become critical aspects that could render the exploitation of a PBR to perform a particular micro-Doppler analysis useless. The length of the blade and the rotation rate influences the amplitude of the micro-Doppler shift. From Equation (7.6) the maximum value of the micro-Doppler shift may be computed as:

$$f_{mD_{max}} = \frac{\mathbf{V}_{tip}}{\lambda} \cos\left(\frac{\beta}{2}\right) \cos(\delta) \tag{7.7}$$

where $\mathbf{V}_{tip} = 2\pi L_b \mathbf{\Omega}$ is the velocity of the tip of a blade. From (7.7) the minimum sampling rate to avoid aliasing and to permit a good time-frequency analysis in the *slow time* can be obtained. For a monostatic radar the maximum micro-Doppler shift may be expressed as Chen [2011]:

$$f_{mD_{max_{mono}}} = \frac{2\mathbf{V}_{tip}}{\lambda} \cos(\alpha) \tag{7.8}$$

where $\alpha$ is the elevation angle of the monostatic platform. From (7.8) and (7.7) it can be seen that the bistatic micro-Doppler shift is always less than the monostatic value and therefore the minimum sampling frequency required to avoid aliasing in a bistatic radar system is smaller than that required in the monostatic case.

An additional parameter of the system that strongly influences the micro-Doppler shift is the wavelength that, if too small, will produce a very high micro-Doppler shift. For this reason very high frequencies are more useful for micro-Doppler analysis of very small micro-motions Ruegg et al. [2007] while in cases such as helicopter blades a larger wavelength could help produce acceptable micro-Doppler shifts.

The wavelength used by the proposed PBR is 19 cm, which is a quite large value that can reduce the maximum micro-Doppler shift obtainable. In addition the bistatic configuration in the near forward scattering zone produces a small value of the product $\cos\left(\frac{\beta}{2}\right)\cos(\delta)$ that appears in (7.7). This product is also helpful in reducing the maximum micro-Doppler shift. For the reasons explained above the proposed PBR is a

good candidate to perform micro-Doppler analysis of the helicopter rotor blades. For example a blade of length of 7.3 m rotating at 4.8 rad/s observed with $\beta$ of 169° and $\delta$ of 10.3° will produce a maximum micro-Doppler shift of 102 Hz that is smaller of half of the system PRF of 1 kHz demonstrating that the proposed PBR is capable to perform micro-Doppler analysis for this kind of target.

In order to analyse performances of the Carse Acquisition (CA) code, the normalized amplitude of the ambiguity function (AF) for a sequence of the CA code is represented in Figure 7.3. The ambiguity function shows the range and Doppler resolution and the sidelobe level in both directions. In Figures 7.4 and 7.5 a cut at 0 delay and 0 Doppler shift of the ambiguity function are shown respectively. It can be seen how the delay resolution of the CA code is relatively small in order to match the original application requirements of this waveform for an accurate navigation. In the Doppler domain the AF has a $sinc^2$ like shape with zero crossing at 1 kHz and a first sidelobe at 1.5 kHz at $-15$ dB. These aspects require further analysis for both the velocities and target detection. In this section we will discuss the first of these aspects while the second one, related to the side-lobe level, will be discussed in Section 7.6.

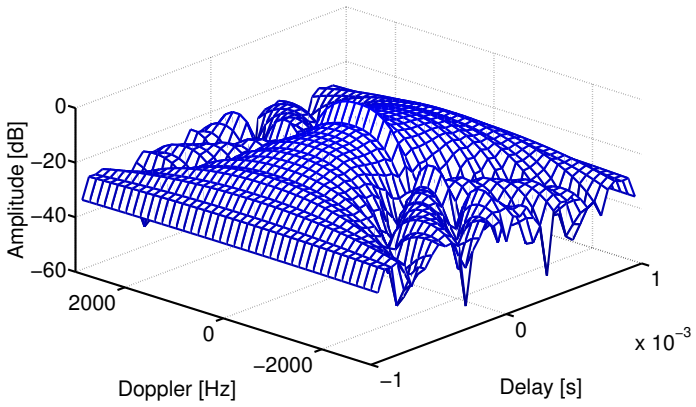


Figure 7.3: 2-D Ambiguity function for the CA code

The bistatic Doppler resolution and AF have been studied in the past Chen [2011]; Tsao et al. [1992]; Willis [1995], where it was demonstrated how the bistatic geometry influences the Doppler resolution.

$$\Delta f_{Bi} = \Delta f_{Mono} \cos\left(\frac{\beta}{2}\right) \tag{7.9}$$

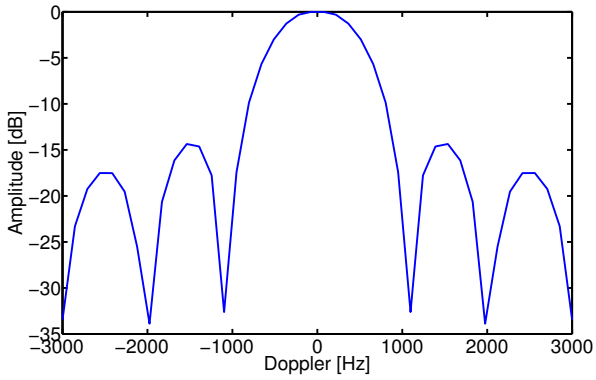


Figure 7.4: Ambiguity function for the CA code at 0 delay

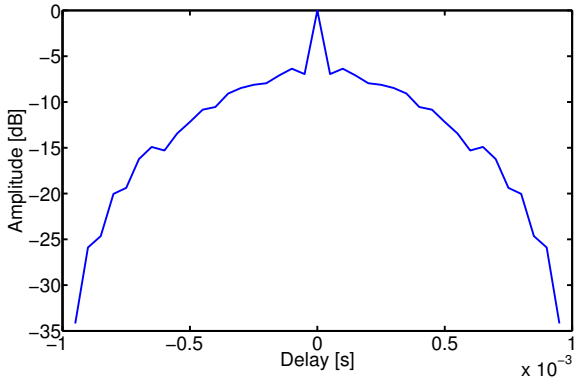


Figure 7.5: Ambiguity function for the CA code at 0 Doppler

From (7.9) the effect of the bistatic angle affects the capability to detect targets with different velocities. In addition in the case of $180^\circ$ the Doppler resolution goes to 0 making it impossible to discriminate targets using Doppler signatures Chen [2011]. Thus the Doppler resolution may not be sufficient in cases where different blades produces similar micro-Doppler shifts. For our purpose it is required to be able to detect the flashes in the time-frequency distribution. Whenever the Doppler resolution becomes ambiguous then the micro-Doppler shift amplitude will not be a discriminant between two helicopters, for example two particular combination of blade length and blade rotation velocity gives a similar m-D shift, the rotating period can still be used as a discriminant and is sufficient for target classification Molchanov et al. [2012].

## 7.5 Forward scattering enhancement

In E. P. Glennon; He et al. [2005]; Mojarrabi et al. [2002] the analysis of the bistatic GPS power budget was presented, in different conditions and with different (more or less optimistic) results, anyway in all this works the main limitation is identified in the very low power at the receiver. A possible solution to this issue is the use of high gain receiver antennas and a relatively big integration time He et al. [2005] facilitating a good maximum operative range to be obtained. An alternative is to exploit the forward scattering enhancement. In forward scattering the diffracted signal power may be many times higher than the backscattered signal Glaser [2011]. This effect can be translated as an enhancement of the radar cross section, known as forward scattering enhancement. This effect can be exploited to cope with the very low power of the received signal in a GNSS based Passive Bistatic Radar (PBR) Cherniakov [2008]; Willis [1995] opening it to the use of a new family of PBR working in near forward scattering zone Koch and Westphal [1995]; Suberviola et al. [2011].

In this section we introduce the forward scattering enhancement in order to predict the bistatic RCS for the rotor blade.

The forward scattering enhancement occurs when the bistatic angle is large, i.e. near $180^\circ$ Glaser [2011]. When an opaque object is illuminated by an electromagnetic wave, a shadow is produced if the object dimensions of the objects are larger than the wavelength. The shadow, which occurs on the opposite side of the object from the energy source, describes a region in which the electromagnetic fields are very small. It means that the currents induced in the object by the incident wave re-radiate a secondary electromagnetic wave that cancels the incident wave in the shadow region. The resulting forward-scattered radiation can be determined by integrating contributions from the induced currents. However this is very impractical, since doing so requires knowledge of the currents themselves which in turn requires knowledge that involves solving a difficult boundary value problem. For this reason the use of the equivalence theorem Felsen et al. [2009] facilitates the forward scattered radiation to be obtained. For this purpose it is required that the radiation scattered by currents induced in the object must be equal to the radiation from appropriate electrical and magnetic surface currents on

an infinite plane. These surface currents are proportional to the cancelled fields in the shadow region and are zero elsewhere. By integrating the different contributions over the plane it is possible to compute the radiation from the surface currents. Since the cancelled fields on the plane are in phase, their different contributions also add up in phase in the forward direction, resulting in a strong radiation peak. Moreover, the radiation pattern is similar to the pattern generated when the same incident fields impinge on an aperture in an opaque screen whose shape is identical to the object's shadow, or silhouette. In Siegel [1958] it was shown that based on the physical optics, the forward-scatter RCS for a target with silhouette area $A$ is:

$$\sigma_{b_{peak}} = \frac{4\pi A^2}{\lambda^2} \tag{7.10}$$

This is principally due to the Babinet's principle, which says that the diffracted wave from a perfect absorbing target is the same as that radiated from an aperture of the same shape and area $A$ of the target. In our case we are considering a rotor blade of length $L_b$ and blade width $W_b$, then the surface area $A$ can be replaced in (7.10) that becomes:

$$\sigma_{b_{peak}} = \frac{4\pi (L_b W_b)^2}{\lambda^2} \tag{7.11}$$

For example Figure 7.6 shows the bistatic RCS for a rectangular shaped rotor blade sized $5.5\text{m}\times 0.6\text{m}$.

In order to calculate the RCS of a helicopter rotor blade, in literature the Physical

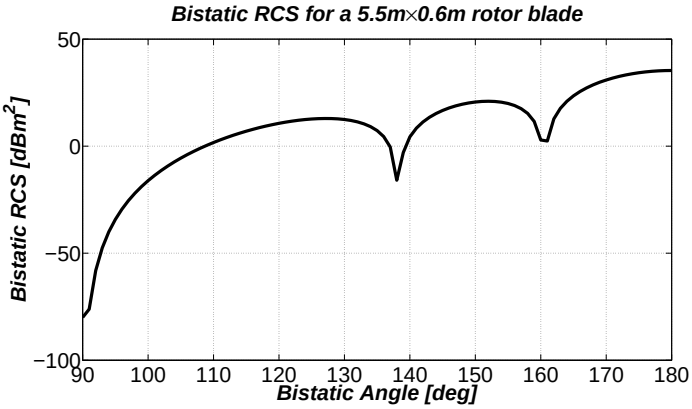


Figure 7.6: Bistatic RCS for a $5.5 \times 0.6$ m rotor blade.

Optics approximation has been used Pouliguen et al. [2002]. In our analysis we will use a simpler model of the rotor blade and the Physic Optics to obtain the angle dependent RCS. We used the physical optics approximation provided in the POfacets tool for Matlab® POfacets simulating a flat metallic blade with the rotating plane parallel to the ground. The simulated rotating blade is illuminated on the top face from the transmitter and the receiver looks at it from the bottom. The bistatic angle is then measured at the tip of the blade. Working in the near-forward scattering zone the Babinet principle warranties that the most important part is the target silhouette and not its composition or the shape of the blade surface. In Pouliguen et al. [2003] the case of big bistatic angles was analysed and a strong return from a rotor blade at $180°$ was demonstrated. In Figure 7.6 it can be seen that for values of the bistatic angles between $165°$ and $180°$ the bistatic RCS values are higher than $20$ dBsm which still represent considerable high values.

The value of the bistatic RCS of the rotor blade is a critical aspect in the proposed approach. High RCS values that are obtained in the near forward scattering zone are required to provide an acceptable maximum operative range. This aspect will be analysed in the budget analysis developed in the next section.

## 7.6 Budget analysis

In this section the analysis is contextualized in the case of the helicopter rotor blades showing that they can be detected using an appropriate system configuration within an acceptable range.

The power density that reaches the receiving antenna after the scattering from the rotor blades is given by Skolnik [1981]:

$$S_r = \left(\frac{P_t G_t}{4\pi R_T^2}\right)\left(\frac{\sigma_b}{4\pi R_R^2}\right) \tag{7.12}$$

where $P_t$ is the transmitted power, $G_t$ is the transmitter antenna gain and $\sigma_b$ is the radar cross section of the rotor blade that, in our case, is increased by the forward scattering enhancement as explained in section 7.5. From (7.12) the power at the receiver after

the target reflection can be expressed as:

$$P_r = \left(\frac{P_t G_t}{4\pi R_T^2}\right)\left(\frac{\sigma_b}{4\pi R_R^2}\right)\left(\frac{\lambda^2 G_r}{4\pi}\right) \tag{7.13}$$

The first factor on the right side of (7.13) is the power density of the direct signal incident on the target and is termed $S_{dir}$. The noise at the output of the RF front-end is $N_0 = kT_{eff}BW$, where $k$ is the Boltzmann constant, $T_{eff}$ is the equivalent noise temperature and $BW$ is the bandwidth. In this budget the losses due to processing $L_{sp}$ and the processing gain $G_{sp}$ are also required in order to obtain the final signal to noise ratio E. P. Glennon:

$$SNR = \frac{S_{dir}\sigma_b \lambda^2 G_r G_{sp}}{(4\pi)^2 L_{sp} R_R^2 k T_{eff} BW} \tag{7.14}$$

For the case of a PBR another factor must be considered in the analysis: the direct signal interference (DSI). In our specific case a strong signal from the transmitting GNSS satellite will be received introducing limitations on the capability to detect a target Griffiths and Baker [2007]. The DSI is defined as the ratio between the received power from the target and the direct signal.

$$DSI = \frac{P_r}{\left(\frac{P_t G_t}{4\pi R_{TR}^2}\right)\left(\frac{\lambda^2 G_r}{4\pi}\right)} \tag{7.15}$$

where $R_{TR}$ is the baseline between the transmitter and the receiver. In Figure 7.7 the DSI for a $5.5 \times 0.6$ m rotor blade is shown. The power reflected from the target depends on the bistatic angle since the bistatic RCS changes with it. Thus the DSI also depends on the bistatic configuration.

Considering a range of operative angles between $140°$ and $175°$ then from Figure 7.7 is is seen that the DSI varies between -60 and -30 dB. However this is the expected DSI in the zero Doppler. The Doppler shift from a rotor blade seen from a monostatic radar is in the order of 1500 Hz but this shift is reduced in the bistatic case. For increasing bistatic angles the Doppler shift produced by the component of the velocity vector orthogonal to the bisector of the bistatic angle results in the order of 100 Hz for helicopter rotor blades, appearing in the first side lobe of the shrunk version of the

ambiguity function in Figure 7.3. For this reason 15 dB less of DSI can be considered. However a suppression strategy will still be required in order to mitigate the DSI of maximum -45 dB. Different approaches have been proposed to mitigate the DSI Griffiths and Baker [2007]. Existing PBR are able to work in more restrictive conditions, with stronger interference Howland et al. [2008]. For this reason existing methods can be applied in our case. For example in Howland et al. [2008] a two-stage adaptive noise canceller was developed. The first stage is an adaptive M-stage lattice predictor, and the second an adaptive tapped delay line. This approach provides a high level of suppression of the DSI in the order of 75 dB. The selection of the best technique for the DSI removal in our specific case goes beyond the scope of this work and might be addressed in the future.

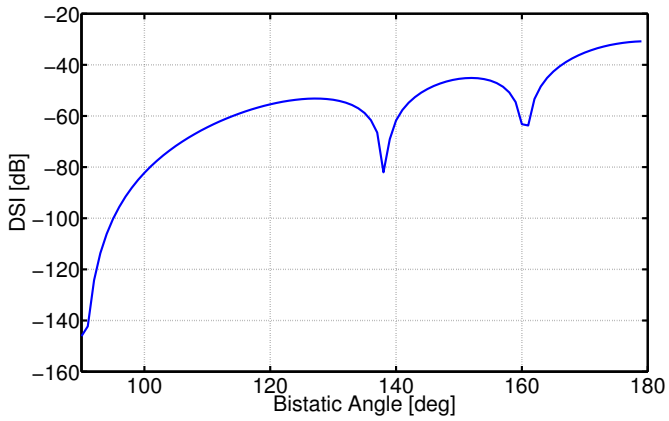


Figure 7.7: DSI for a $5.5 \times 0.6m$ rotor blade.

From the discussion above it is now possible to compute the maximum achievable range assuming a minimum Signal to Interference and Noise Ratio (SINR) value, defined as:

$$\text{SINR} = \frac{P_r}{\frac{P_t G_t}{4\pi R_{TR}^2}\frac{\lambda^2 G_r}{4\pi} + kT_{eff}BW} \tag{7.16}$$

The maximum range that can be obtained as:

$$R_{R_{max}} = \sqrt{\frac{S_{dir}\sigma_b \lambda^2 G_r G_{sp}}{(4\pi)^2 L_{sp} \text{SINR}_{min} kT_{eff}BW}} \tag{7.17}$$

The values to be used in (7.17) to obtain the maximum range for the application under

Table 7.1: Simulated parameters in the budget analysis.

| Parameter | Value | Units |
|---|---|---|
| $S_{dir}$ | $39.81 \times 10^{-15}$ | $W/m^2$ |
| $L_b$ | 5.5 | $m$ |
| $W_b$ | 0.6 | $m$ |
| $\sigma_b$ | 379 | $m^2$ |
| $\text{SINR}_{min}$ | 8 | dB |
| Bandwidth | $2.046 \times 10^6$ | Hz |
| $T_{eff}$ | 344 | K |
| $\lambda$ | 0.19 | m |
| $G_{sp}$ | 53.2 | dB |
| $L_{sp}$ | 3.25 | dB |
| $G_r$ | 25 | dB |
| $k$ | $1.30 \times 10^{-23}$ | |
| $R_{max}$ | 2420 | m |

consideration are shown in Table 7.1. These values differs from the one used in E. P. Glennon. In that work a processing gain of 63 dB was assumed. This gain is not acceptable for the micro-Doppler analysis where the integration time is limited by the time coherence of the specific target. For this reason the 40 dB gain coming from the C/A code cross-correlation is considered and 13.2 dB is added assuming a 21 ms integration time. Due to this decrease in the processing gain a 25 dB receiver antenna gain is considered. The RCS of the rotor blade with blade length $L_b$ and blade width $W_b$ is considered to be ten times less than the peak RCS obtainable in the forward scattering configuration from (7.11). From the parameters in Table 7.1 the maximum range is in the order of 2.4 km. This is a reasonable distance to have an effective near forward scattering configuration for this kind of PBR.

## 7.7 Simulations and results

In this section the results obtained simulating the rotor blades of different helicopters using the proposed PBR are presented. Results that compute the maximum range for different helicopters based on the rotor blades parameters given in Table 7.2 and the budget parameters (excluding the RCS) in Table 7.1 are now presented.

Table 7.2: Simulated helicopter rotor blade features and target parameters for the configuration in Table 7.3.

| Model | AW-109 Agusta | AH-64 Apache | UH-60 Black Hawk | MD 500E Defender |
|---|---|---|---|---|
| # of blades | 4 | 4 | 4 | 5 |
| Blade length [m] | 5.5 | 7.3 | 8.18 | 4 |
| Blade width [m] | 0.6 | 0.6 | 0.6 | 0.6 |
| Rotor vel. [r/s] | 7 | 4.8 | 4.3 | 8.2 |
| Tip velocity [m/s] | 241.90 | 220.16 | 221.00 | 206.08 |
| Maximum m-D shift [Hz] | 112.24 | 102.13 | 102.52 | 95.60 |
| RCS [dBsm] | 25.76 | 28.2 | 29.2 | 22.9 |

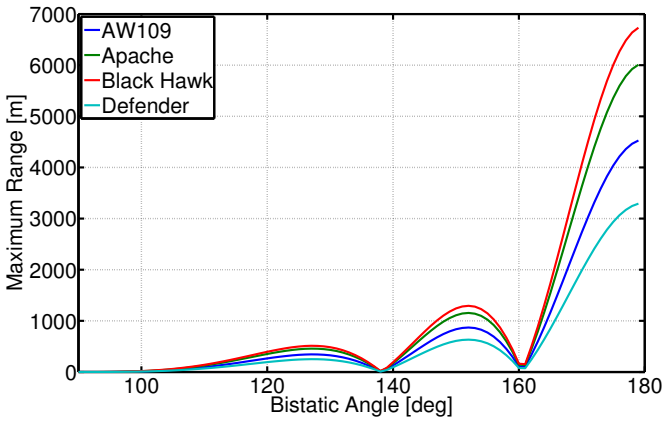


Figure 7.8: Maximum Range for the helicopters in Table 7.2 with the parameters in Table 7.1.

In Figure 7.8 the maximum ranges obtained for the four helicopters are shown. It can be seen that the maximum range increases as the bistatic gets closer to 180°. It can be seen from Figure 7.8 that for smaller rotor blades, like in the case of the Defender, the maximum range is smaller, while for bigger blades, like those of the Black Hawk, the maximum range becomes larger as it is able to exploit the forward scattering enhancement in a superior fashion.

In Figure 7.9 the resulting DSIs for the four helicopter rotor blades at a range distance of 4 km from the receiver is shown. It can be seen how for each of the helicopters we obtain a wide range of angles where the power reflected from the blades reduces the direct signal interference due to the forward scattering enhancement.

Numerical values for the simulated geometry shown in Figure 7.1 are given in Table 7.3 where the helicopter is located at P. The geometry simulates the case where the helicopter is approaching the baseline leading to the condition that can produce forward scattering enhancement. This condition seems to be very particular and restrictive, however with a high degree of probability, there are generally three or four satellites

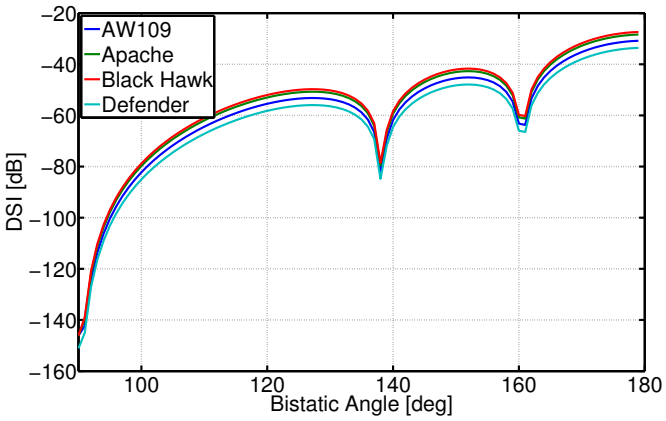


Figure 7.9: DSI for the helicopters in Table 7.2 with the parameters in Table 7.1.

Table 7.3: Simulated geometry.

| | | |
|---|---|---|
| $X_T$ | 0 | $m$ |
| $Y_T$ | 0 | $m$ |
| $Z_T$ | $20200 \times 10^3$ | $m$ |
| $X_R$ | 0 | $m$ |
| $Y_R$ | 0 | $m$ |
| $Z_R$ | 0 | $m$ |
| $X_P$ | 400 | $m$ |
| $Y_P$ | 0 | $m$ |
| $Z_P$ | 2200 | $m$ |
| $\beta$ | 169.69 | $deg$ |
| $\delta$ | 10.30 | $deg$ |

illuminating the same area, thus increasing the probability to have such a configuration. In Table 7.2 the characteristics of the four simulated helicopters are provided. It can be seen that they have different blade length and rotation velocity and three of them have an even number of blades while one has an odd number of blades. The table provides also the maximum micro-Doppler shift expected in the case of the simulated geometry using the parameters given in Table 7.3. It can be seen that despite the different features of the helicopters, the interval containing the maximum micro-Doppler is very small. However we will show that it remains sufficient to discriminate between the different helicopters.

Figures 7.10-a, 7.11-a, 7.12-a and 7.13-a show the amplitude of the radar return from the rotor blades of the four helicopters. These clearly shows that the radar return comprises flashes that repeats with an interval equal to the rotation frequency of the

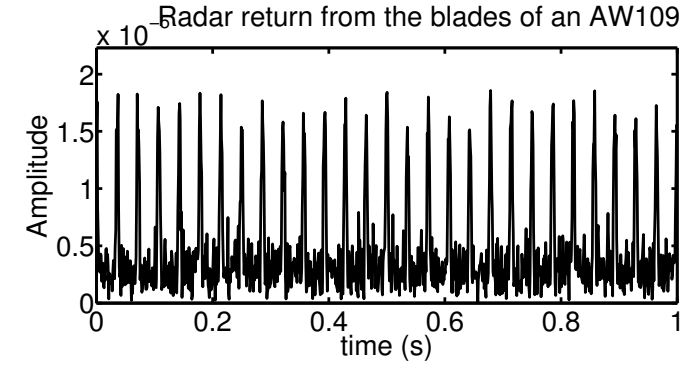


(a)

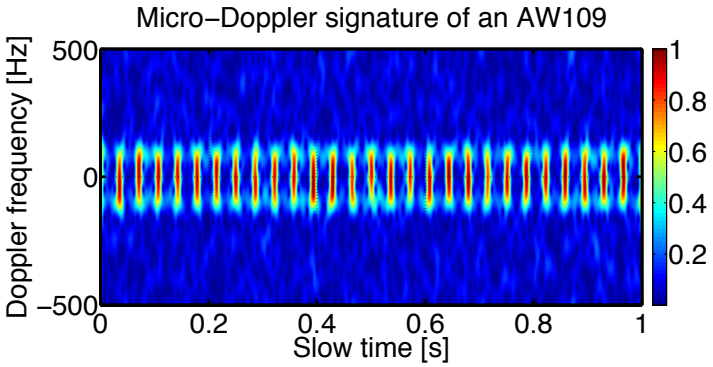


(b)

Figure 7.10: Radar return and micro-Doppler signature for an AW109.

rotor blades divided by the number of blades. However this is the only information about the rotor feature that can be obtained from this plot. For a more accurate, complete and useful analysis a time-frequency analysis is required. From Figure 7.13-a it can be seen that the signal is more affected by noise principally due to the smaller RCS of the rotor blades that are actually smaller as it can be seen from the data reported in Table 7.2. For this reason the analysis of the radar return amplitude is very difficult and almost useless for our purpose.

In Figures 7.10-b, 7.11-b, 7.12-b and 7.13-b the micro-Doppler signature of the simulated received signal from each of the helicopters rotors are shown. The time-frequency analysis is performed using the short time Fourier transform using an Hamming window of the duration of 21 ms.

For the helicopters with an even number of blades, Figures 7.10-b, 7.11-b and 7.12-b it can be seen that flashes in both the positive and negative Doppler appears. This is due to the symmetry of the rotor meaning that while a blade is approaching the receiver

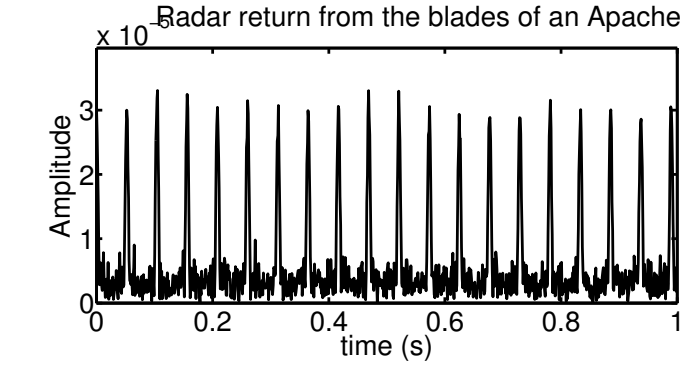


(a)

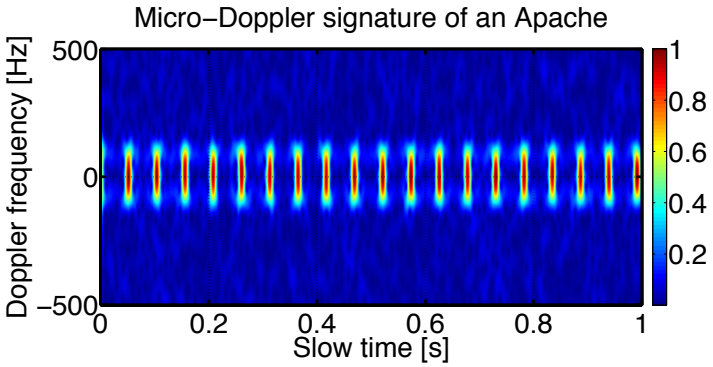


(b)

Figure 7.11: Radar return and micro-Doppler signature for an Apache.

the one on the same axis of the rotor is receding from the receiver, then two blades at the same time will produce the same micro-Doppler shift at the same time but with different sign. In Figure 7.13-b the flashes are not aligned, this is due to the fact that since the number of blades is odd. It means that there will not be two blades with the velocity vector $\mathbf{V}_{tip}$ parallels to the bisector of the bistatic angle $\beta$ at the same time. For the case shown in Figure 7.10 the period of the rotation can be obtained from the flashes and is measured to be of 0.1432 seconds corresponding to 6.9832 rps close to the original 7 rps. The maximum amplitude of the micro-Doppler shift measured at the -3 dB point is of 112.5 Hz. From this information the following formula can be obtained from (7.7) and can be used to estimate the blade length:

$$\hat{L}_b = \frac{\hat{f}_{mD_{max}}\lambda}{\cos\left(\frac{\beta}{2}\right)\cos(\delta)2\pi\hat{\mathbf{\Omega}}} \tag{7.18}$$

where $\hat{f}_{mD_{max}}$ and $\hat{\mathbf{\Omega}}$ are the estimated maximum Doppler shift and rotation rate re-

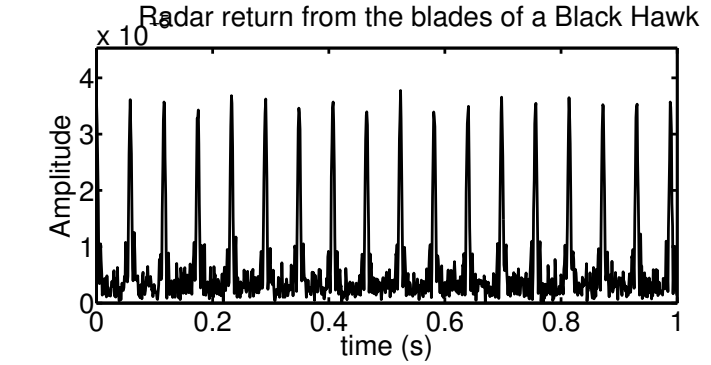


(a)

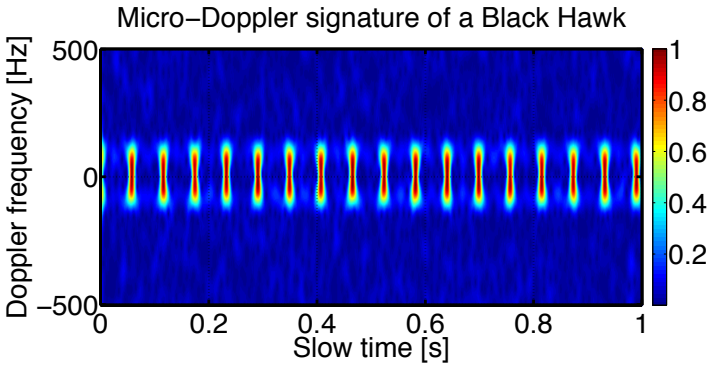


(b)

Figure 7.12: Radar return and micro-Doppler signature for a Black Hawk.

spectively. From (7.18) for the case of the Agusta AW109 the estimated blade length results to be 5.5268 m a value very close to the simulated value in Table 7.2. For the case of the Apache in Figure 7.11 the measured rotation rate is of 4.78 rps while the maximum micro-Doppler results to be 97.39 Hz leading to an estimated blade length of 6.98 m, the error is principally due to the choice of frequencies bins in the time-frequency analysis. The measured rotation rate for the Black Hawk Figure 7.12 is of 4.29 rps while the maximum micro-Doppler results to be 102.4 Hz leading to an estimated blade length of 8.1887 m, again the micro-Doppler signature is good to extract the features of the rotor blades. Last case is the case Figure 7.13 with 5 blades, in this case the measured rotating rate is 8.1566 rps and the maximum micro-Doppler frequency results to be of 97.39 Hz, these values leads to obtain a blade length of 4.0962 m that is a good estimation of the original length.

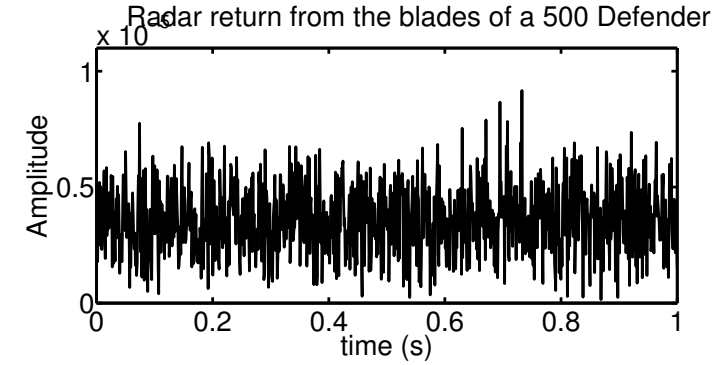


(a)

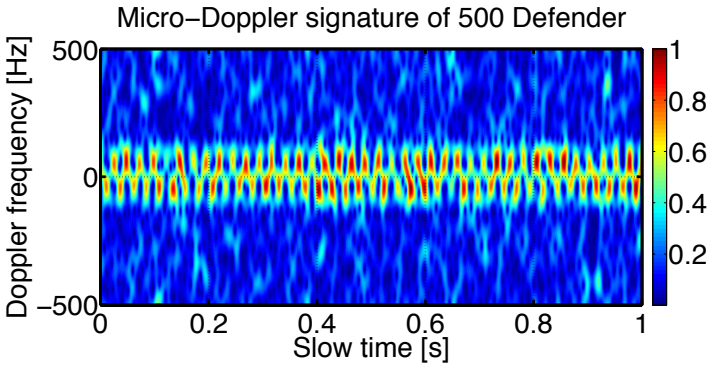


(b)

Figure 7.13: Radar return and micro-Doppler signature for a Defender.

## 7.8 Conclusion

This chapter investigated the possibility of exploiting the GNSS signal in a Passive Bistatic Radar system when a target is in the near forward scattering zone for micro-Doppler analysis. The feasibility study has provided the budget analysis showing that by exploiting the forward scattering enhancement it is possible to obtain enough forward scattered power from the rotor blades of a helicopter. The feasibility study investigated the micro-Doppler characteristics of the echoes received from the rotating blades, showing that this particular system operating in the near forward scattering zone allows useful analysis of the micro-Doppler signatures.

The proposed PBR system has been simulated and the presence of different helicopters flying in the near forward scattering zone has been simulated. The micro-Doppler signature relative to their rotor blades in this kind of system has been analysed and the possibility to extract the rotor blades features from it has been shown with a good confidence in the possibility to recognize the specific helicopter.

The proposed PBR is therefore a good candidate to be an alternative application of the GNSS signal and is useful for the analysis of the micro-Doppler signatures of helicopters and can find applications in areas such as borders or coastal surveillance.

# Chapter 8

# Advanced micro-Doppler analysis and extraction

## 8.1 Introduction

In this chapter two advanced aspect of the micro-Doppler analysis are discussed: the effect of wind turbines in SAR imaging and the extraction of micro-Doppler signatures from clutter. In Chapter 3 we have introduced the effect on SAR images of vibrating targets. A case of extended objects of particular interest is the effect on SAR images introduced by rotating wind turbines, which is analysed in this chapter. The results show that an image can appear corrupted and that smearing and ghost echoes can possibly hide details of the images that can be distant from the wind turbine.

In an operative system the micro-Doppler signal will normally be embedded in clutter with a low Signal to Clutter Ratio (SCR) and the challenge becomes the extraction of this feature from the received signal.

In this chapter a technique based on SSA is developed and applied for micro-Doppler extraction from SAR data in the case of the PBR system proposed in Chapter 7.

The remainder of this chapter is organized as follows. Section II introduces the acquisition SAR geometry with respect to the presence of a wind turbine in the scene and derives the signal model showing some simulation results on the effect in two canonical geometries. Section III presents the SSA approach and its novel application of for the effective extraction of micro-Doppler signatures from the radar returns. Results

obtained through simulations confirms the usefulness of the extraction technique.

## 8.2 Effect of wind turbines in SAR images

In this section the acquisition geometry and the received signal model are introduced. A top view of the acquisition geometry is shown in Figure 8.1. The wind turbine is located at $P$ with $\theta_t$ indicating the rotation angle between the rotor and the platform flight track. The angle $\theta_g$ is the observation angle between the platform and the wind turbine.

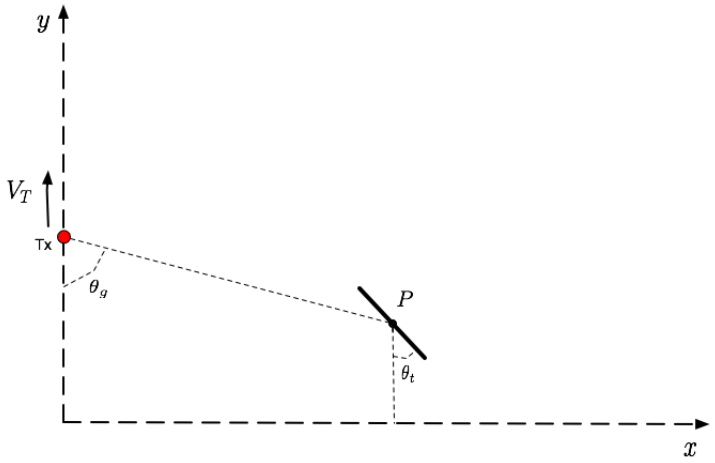


Figure 8.1: Acquisition geometries, top view.

The effect of targets with micro-motions in SAR was theoretically studied in Chen et al. [2006], while in Sparr and Krane [2003a] and Ruegg et al. [2007] the effect was analysed using real experiments. Mechanical vibrations or rotations of radar targets induce a superimposed phase modulations in the received SAR signal. In the case of a wind turbine rotating with angular velocity $\Omega_t$, the phase modulation induced on the SAR received signal is Gallardo-Hernando et al. [2011]:

$$\Phi_{WT_i}(\eta) = -\frac{4\pi}{\lambda_c} L \cos(\theta_t - \theta_g) \cos(\Omega_t \eta + \phi_i) \tag{8.1}$$

where $\eta$ represents the slow time, $\lambda_c$ the carrier frequency, $L$ is the blade length and $\phi_i$ is the initial rotating phase of the $i$-th blade. From the derivative of (8.1) the induced

Doppler frequency shift from the $i$-th blade results:

$$f_{WT_i}(\eta) = \frac{2L\Omega_t}{\lambda_c} cos(\theta_t - \theta_g)\sin(\Omega_t\eta + \phi_i) \tag{8.2}$$

Thus the received SAR signal after range compression from a point scatterer located on the tip of the $i$-th blade of the wind turbine results to be Ruegg et al. [2007]:

$$s_{rc_i}(\tau,\eta) = p_r\left(\tau - \frac{R(\eta)}{c}\right) w_{az}(\eta)\exp\left\{-j\frac{4\pi f_0 R(\eta)}{c}\right\}\exp\left\{-j2\pi f_{WT_i}\eta\right\} \tag{8.3}$$

where $c$ is the speed of light, $R(\eta)$ is the slant range function, $\tau$ is the fast time, $p_r(.)$ is the range envelope and $w_{az}(.)$ is the antenna pattern.

The second exponential in (8.3) that includes the Doppler shift from the wind turbine blade can be expanded as a series of Bessel functions of the first kind Chen et al. [2006]. Assuming $\phi_i = 0$ the contribution of a single blade the radar return can be modelled as:

$$J_k(B) = \frac{1}{2\pi}\int_{-\pi}^{\pi} e^{j(B\sin\Omega_t\eta - k\Omega_t\eta)} d\Omega_t\eta \tag{8.4}$$

where $B = \frac{2\pi}{\lambda_c} L\Omega_t\cos(\theta_t - \theta_g)$ and $J_k(B)$ decreases with increasing $k$. Thus the received signal can be written as:

$$\begin{aligned} s_{rc}(\tau,\eta) =& p_r\left(\tau - \frac{R(\eta)}{c}\right) w_{az}(\eta) e^{-j\frac{4\pi f_0 R(\eta)}{c}} \sum_{k=-\infty}^{\infty} J_k(B) e^{jk\Omega_t\eta} = \\ & p_r\left(\tau - \frac{R(\eta)}{c}\right) w_{az}(\eta) e^{-j\frac{4\pi f_0 R(\eta)}{c}} [J_0(B) + J_1(B)e^{j\Omega_t\eta} - J_1(B)e^{-j\Omega_t\eta} \\ & + J_2(B)e^{j2\Omega_t\eta} + J_2(B)e^{-j2\Omega_t\eta} + J_3(B)e^{j3\Omega_t\eta} - J_3(B)e^{-j3\Omega_t\eta} + \cdots] \end{aligned} \tag{8.5}$$

From (8.5) it can be seen that the rotating turbine introduces a Doppler shift that will result in an infinite number of ghost targets in the final focussed image. It can be seen how the series of echoes depends on the turbine characteristics: the blade length, rotation velocity and aspect angle defined as $\theta_a = \theta_t - \theta_g$. This last parameter influences the amplitude of the maximum Doppler shift. Indeed the maximum Doppler

shift increases with $|\theta_a| \rightarrow 90°$, for this reason in the next section simulations with two different values of $\theta_a$ are presented in order to address the two canonical geometries: the case of the wind turbine facing the flight track and the case of the wind turbine orthogonal to the flight track.

### 8.2.1 Simulation Results

In this section the results obtained simulating the acquisition from an X-band side-looking SAR and focussed using the Range Doppler Algorithm Cumming and Wong [2005] are reported. Two simulations are presented, the first with the rotor of the wind turbine facing the flight track of the SAR platform while the second is with the blades rotating in the plane orthogonal to the platform flight track. Illustrations of the simulated geometries are shown in Figure 8.2-a and Figure 8.2-b. These two simulations cover two canonical cases, the case $\theta_a \approx 0°$ and $\theta_a \approx 90°$ respectively.

In Table 8.1 the simulation parameters for the SAR acquisition and the wind turbine are reported. In each simulation 20 scatterers have been considered along each blade and 5 scatterers have been considered on the rotor and the tower of the wind turbine.

In Figure 8.3 the results obtained for the configuration with the wind turbine facing

Table 8.1: Simulation parameters

| | |
|---|---|
| PRF | 1000 Hz |
| Carrier Frequency | 9.5 GHz |
| Pulse Duration | 10 $\mu$s |
| Flight Duration | 1 s |
| Pulse Bandwidth | 50 MHz |
| Platform Velocity | 100 m/s |
| Wind Turbine: range position | 4000 m |
| Wind Turbine: rotor altitude | 50 m |
| Wind Turbine: # of blades | 3 m |
| Wind Turbine: blade length | 26 m |
| Wind Turbine: rotating velocity | 0, 18 and 30 rpm |
| Wind Turbine: aspect angle | 0 and 90 deg |

the flight track of the platform (configuration in Figure 8.2-a) are presented. Figure 8.3-a shows the result when the wind turbine has the rotating velocity of 0 rpm while Figure 8.3-b and Figure 8.3-c show the case of 18 and 30 rpm respectively. In the first

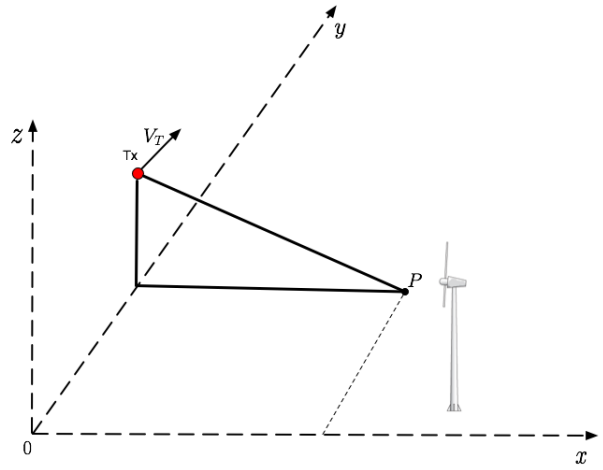


(a)

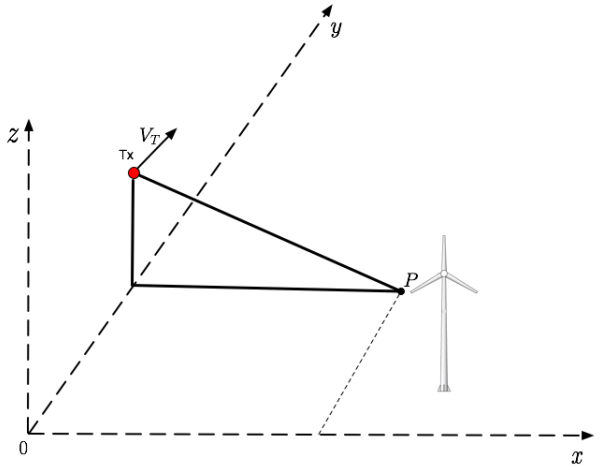


(b)

Figure 8.2: Simulated geometries: a) wind turbine facing the flight track of the platform, b) wind turbine orthogonal to the flight track of the platform.

case there is no smearing in the image while in both cases where the rotating frequency is different from 0 it can be seen how the focussing stage in the azimuth direction fails to focus correctly the wind turbine leading to a smeared image, the smearing of the image increases with the wind turbine rotating velocity.

In Figure 8.4 the results obtained for the configuration with the wind turbine placed with the rotor orthogonal to the platform flight track (configuration in Figure 8.2-b) are presented. Figure 8.4-a shows the result when the wind turbine has the rotating velocity of 0 rpm while Figure 8.4-b and Figure 8.4-c show the case of 18 and 30 rpm respectively. In the first case there is no smearing or ghost echoes in the image while

in both cases where the rotating frequency is different from $0$ it can be seen how the focussing stage in the azimuth direction fails to focus correctly the wind turbine leading to an image that shows ghost echoes for each of the scatterers on the $3$ blades, in accordance with (8.5). The intensity and the shape of resulting ghost image is the overlap of the intensities of the echoes of each scatterer located along the blades leading to an extended stripe of echoes that affects all the range gates in which the blades are present.

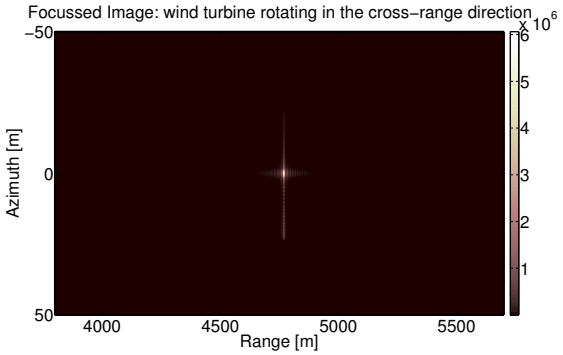


(a)

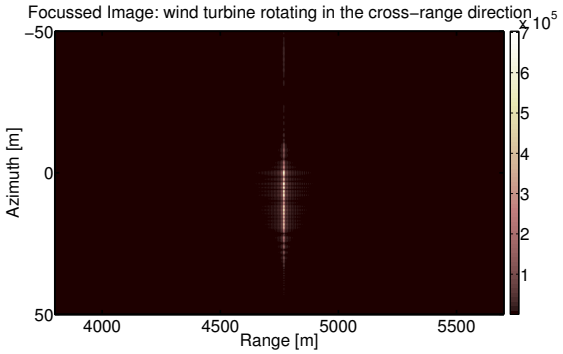


(b)

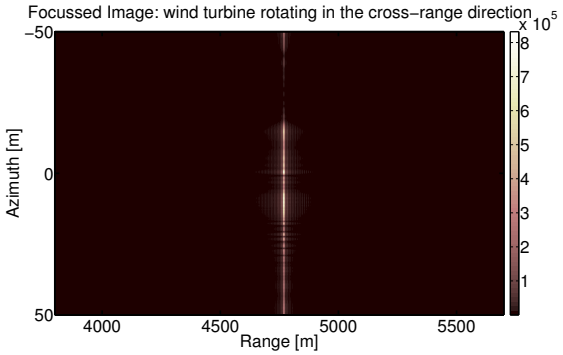


(c)

Figure 8.3: Focussed SAR image with the wind turbine placed with the blades parallel to the platform flight track a) fixed b) rotating at 18 rpm and c) rotating at 30 rpm.

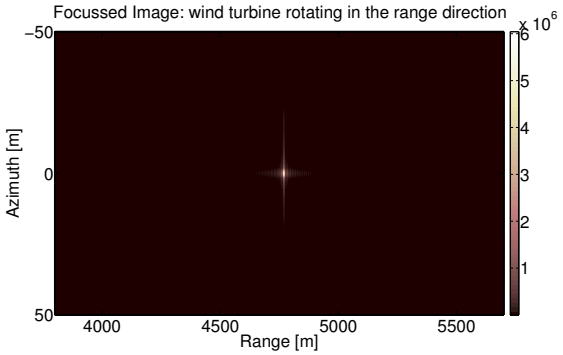


(a)

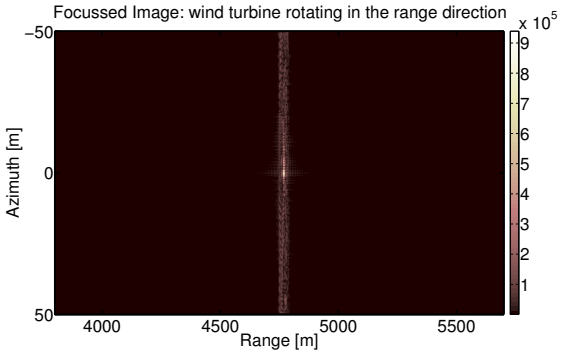


(b)

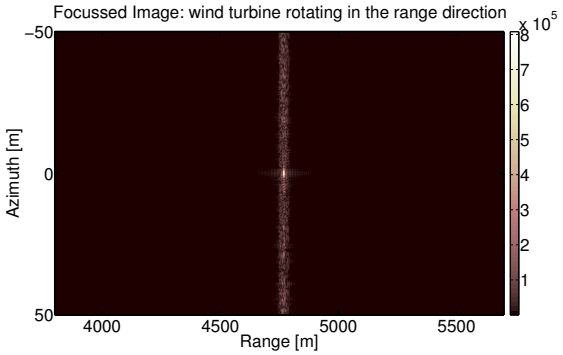


(c)

Figure 8.4: Focussed SAR image with the wind turbine placed with the blades orthogonal to the platform flight track a) fixed b) rotating at 18 rpm and c) rotating at 30 rpm.

## 8.3 Singular Spectrum Analysis based Extraction of micro-Doppler signatures

In Chapter 3 the extraction techniques applied to radar data to extract the micro-Doppler signatures have been introduced. The problem rises in presence of strong return from stationary objects in the scene or from interference signals that could bury the micro-Doppler signature. For this reason signal processing techniques are required to mitigate the effect of the clutter, in this chapter we apply the Singular Spectrum Analysis as useful technique to suppress the clutter and extract correctly the micro-Doppler signature.

Singular Spectrum Analysis (SSA) is a technique used to analyse time series signals based on Singular Value Decomposition (SVD) Golyandina [2001]. The aim of SSA is to decompose the original time series into the sum of a small number of independent and interpretable components such as trends, slowly varying components and noise.

The SSA technique consists of two complementary stages: decomposition and reconstruction. The decomposition firstly uses embedding to decompose the original signal in a trajectory matrix which is then separated into an independent trajectory matrix using SVD. In the reconstruction stage subgroups of the trajectory matrices and diagonal averaging are used to reconstruct the new time series.

The first step in the analysis is the construction of the trajectory matrix Hassani [2007]. Consider a time series of length N , $Y_N = (y_1, \cdots, y_N)$, fix the window length $L \leq N/2$ and defining $K = N - L + 1$. The embedding stage builds a multi-dimensional time series $X_1, \cdots, X_K$ starting from $Y_N$, where $X_i$ is populated with $(y_i, \cdots, y_{i+L-1}) \in \mathbf{R}^L$. The parameter to be selected in this stage is the window length $L$, the trajectory matrix $\mathbf{X} = [X_1, \cdots, X_k]$ is a Hankel matrix which means that all the elements on the diagonal $i + j = const$ are equal.

SVD is then applied to the matrix $\mathbf{X}\mathbf{X}^T$, to form eigenvalues and eigenvectors of $\mathbf{X}\mathbf{X}^T$ represented with $\mathbf{X}\mathbf{X}^T = \mathbf{P}\mathbf{\Lambda}\mathbf{P}^T$ where $\mathbf{\Lambda} = diag(\Lambda_1, \Lambda_2, \cdots, \Lambda_L)$ is the diagonal matrix of the eigenvalues of $\mathbf{X}\mathbf{X}^T$ in non-increasing order and $\mathbf{P} = (P_1, P_2, \cdots, P_L)$ is the corresponding orthogonal matrix of the eigenvectors of $\mathbf{X}\mathbf{X}^T$.

At this stage a selection of the eigenvectors, from a selection of a group of $l$ $(1 \leq$

$l \leq L$) eigen-vectors $P_{i_1}, P_{i_2}, \cdots, P_{i_l}$ from the matrix $\mathbf{P}$ can be performed. This step corresponds to splitting the elementary matrix $\mathbf{X_i}$ in groups and summing the matrix within each group.

The final step is the reconstruction, the matrix $\tilde{\mathbf{X}}$ can be computed as an approximation to $\mathbf{X}$ as $||\tilde{x}_{ij}|| = \sum_{k=1}^{l} P_{i_k} P_{i_k}^T \mathbf{X}$. The one dimensional series can be obtained by the averaging over the diagonals of $\tilde{\mathbf{X}}$ containing the contribute of the components corresponding to the $l$ selected eigen-vectors.

The proposed approach to extract the micro-Doppler signature from SAR data is shown in Figure 8.5.

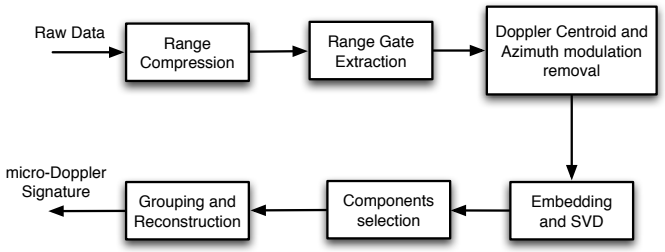


Figure 8.5: Proposed micro-Doppler extraction process.

Starting from the raw data, the range compression step is performed using a replica of the transmitted signal. From the range compressed data the range gate containing the scatterer is selected. Depending on the analyzed configurations a range cell migration correction step Cumming and Wong [2005] can be performed before the extraction of the range gate.

In order to align the signal within the time-frequency plane to obtain a correct visualization and positioning of the time-frequency distribution, the Doppler centroid and the azimuth frequency slope is removed from the signal before the three steps of the SSA. After the reconstruction the resulting micro-Doppler signature can be visualized and used for target classification through the computation of the Pseudo Wigner Ville Distribution (PWVD) Cohen [1989]. For the case of the PBR using the GNSS illuminator the extraction algorithm is the same shown in Figure 8.5 without the Doppler centroid estimation and azimuth modulation removal step.

In order to select the components the clutter energy should be considered, in a realistic scenario the clutter energy results to be higher than the energy from the target with micro-Doppler meaning that the eigenvalues spectrum exhibits clear separation between the clutter components and the micro-Doppler components.

### 8.3.1 Simulation results

The proposed micro-Doppler extraction method was tested with simulated data. In this section will be shown first the results obtained on SAR data then the results about the PBR.

For the SAR case the simulated system is an X band (10 GHz) SAR. In the simulations a K-distributed clutter is assumed. This kind of distribution was shown to fit properly for both monostatic and bistatic ground and sea clutter Yates et al. [2006].

Two simulations with different vibrating amplitudes and frequencies were performed all with a SCR less than $-3$ dBs. The point scatterer model has been used to perform the simulations, in the first simulation a vibrating target with a vibrating amplitude of $10$ cm and a vibrating frequency of $8$ Hz was placed in the scene centre. The PWVD of the range gate under test is shown in Figure 8.6, it can be seen that the sinusoidal modulation induced from the target vibration is not clearly visible while the clutter is strong and evident in the time-frequency analysis.

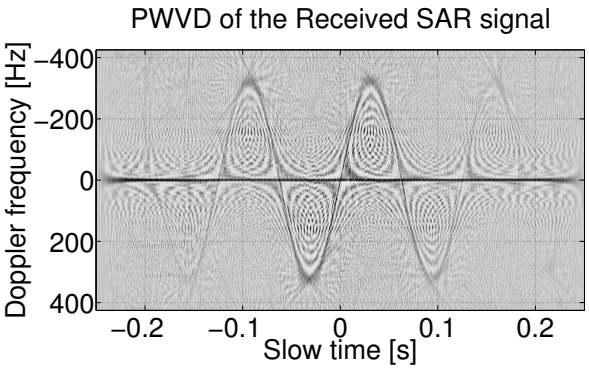


Figure 8.6: Pseudo-Wigner Ville Distribution of the analyzed range gate for the first simulated configuration.

From the eigenvalue spectrum, shown in Figure 8.7, obtained using the SSA it is

possible to identify the main component containing the higher amount of energy.

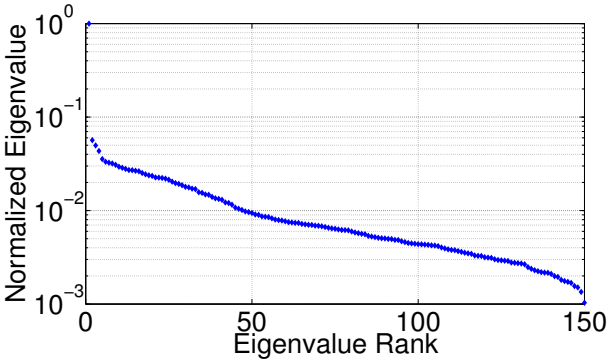


Figure 8.7: Eigenvalue spectrum for the first simulated configuration.

This component contains the contribution of the strong echoes of the stationary clutter signal, while components from 2 to 33 result to contain the micro-Doppler signature of the simulated vibrating target. In Figure 8.8 it is shown the obtained reconstructed micro-Doppler signature extracted from the clutter. It can be seen that the resulting micro-Doppler signature contains all the features describing the vibration. In Figure 8.8 are now clearly visible the 4 periods in 0.5 seconds corresponding to the $8$ Hz vibration of the simulated point target while it can be measured a maximum micro-Doppler frequency of $325$ Hz, corresponds to $0.097$ m of vibrating amplitude.

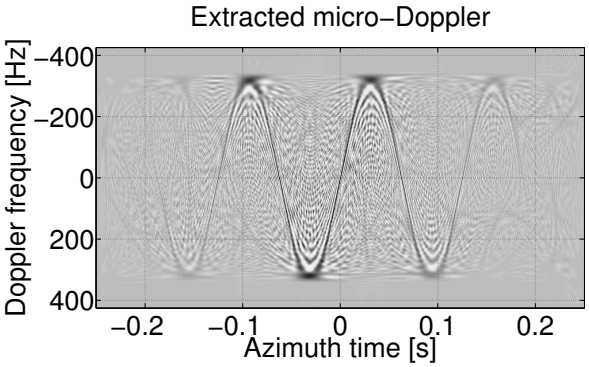


Figure 8.8: Extracted m-D signature for the first simulated config.

The point target for the second case has a vibrating frequency of $5$ Hz and $2$ cm of vibrating amplitude. The PWVD of the range gate under test is shown in Figure 8.9, it

can be seen that the modulation induced from the target vibration is not clearly visible and is actually mixed with the clutter.

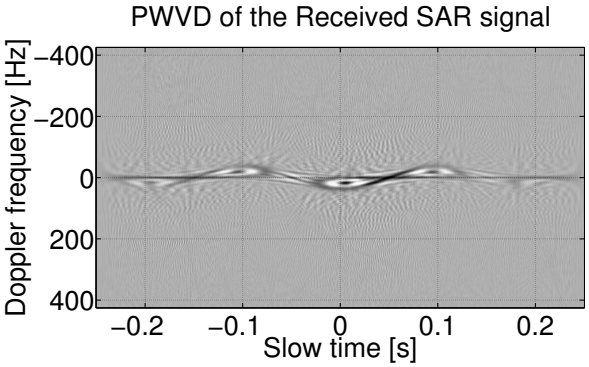


Figure 8.9: Pseudo-Wigner Ville Distribution of the analyzed range gate for the second simulated configuration.

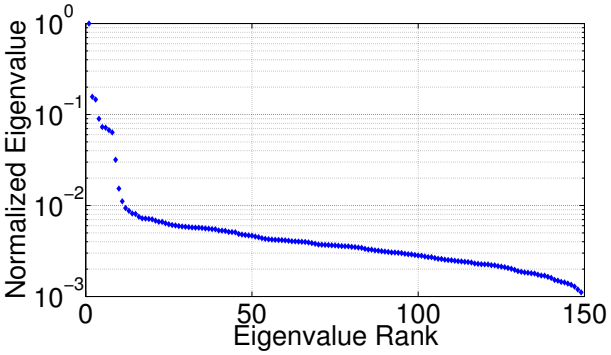


Figure 8.10: Eigenvalue spectrum for the second simulated configuration.

From the eigenvalue spectrum, shown in Figure 8.10, obtained using the SSA it is possible to identify the main component containing the higher amount of energy. This component contains the contribution of the strong echoes of the stationary clutter signal, while components from 2 to 11 contain the micro-Doppler signature of the simulated vibrating target. In Figure 8.11 it is shown that the obtained reconstructed micro-Doppler signature is extracted from the clutter. It can be seen that the resulting micro-Doppler signature contains all the features describing the vibration. In Figure 8.11 can be measured 2.5 periods in 0.5 seconds corresponding to the 5 Hz vibration of the simulated point target while a maximum micro-Doppler frequency of 46 Hz cor-

responding to $0.022$ m of vibrating amplitude was measured.

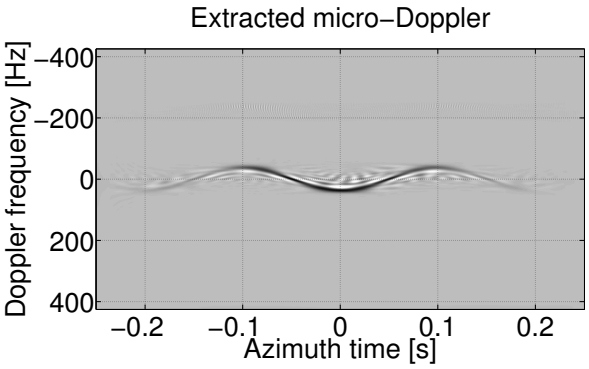


Figure 8.11: Extracted m-D signature for the second simulated config.

The results obtained simulating the returns from helicopters rotor blades buried by high clutter due to the strong return of the helicopter fuselage are now presented.
The simulated system parameters are reported in Table 8.2. These values are the same used for the budget analysis proposed in chapter 7 with the only exception of the SCR that now is considered in the analysis. In chapter 7 has been demonstrated that with these parameters rotor blades can be detected within ranges in the order or 3 km with a minimum SNR of $8$ dBs. An important parameter is the maximum Signal to Clutter

| **Parameter** | **Value** | **Units** |
|---|---|---|
| $S_{dir}$ | $39.81 \times 10^{-15}$ | $W/m^2$ |
| $L_b$ | $5.5$ | $m$ |
| $W_b$ | $0.6$ | $m$ |
| $\sigma_b$ | $379$ | $m^2$ |
| $MaxSCR$ | -98 | dB |
| Bandwidth | $2.046 \times 10^6$ | Hz |
| $T_{eff}$ | $344$ | K |
| $\lambda$ | $0.19$ | m |
| $G_{sp}$ | $53.2$ | dB |
| $L_{sp}$ | $3.25$ | dB |
| $G_r$ | $35$ | dB |
| $k$ | $1.30 \times 10^{-23}$ | |

Table 8.2: Simulated parameters.

Ratio, $MaxSCR$, where the useful signal is the return from the blade and the clutter

is the return from the fuselage. This is a very low value providing a good test bench for the SSA technique.

The simulated helicopters parameters are reported in Table 8.3. The bistatic RCS of the blades has been computed using the physical optics approximation provided in the POfacets tool for Matlab® POfacets considering a metallic blade. The rotating plane for the blades is assumed to be parallel to the earth, different angles will reflect in a deviation of the angle $\delta$. In Figures 8.12-a and 8.13-a the time-frequency analysis obtained using the Short Time Fourier Transform of the received signal is shown. It can be seen how the strong return from the fuselage buries the return from the rotor blades.

In Figure 8.12-b the eigenvalues spectrum obtained using the SSA with an embedding

| **Model** | **# of blades** | **Blade length [m]** | **Blade width [m]** | **Rotor vel. [r/s]** |
|---|---|---|---|---|
| AH-64 Apache | 4 | 7.3 | 0.6 | 4.8 |
| MD 500E Defender | 5 | 4 | 0.6 | 8.2 |

Table 8.3: Simulated helicopters and rotor blades features.

length of 150 samples is shown for the case of the Apache. It is possible to identify the first stronger component that contains the strong clutter return, while the others contain other features of the echoes. Components 2 to 10 are used to reconstruct the micro-Doppler signatures. The noise floor begins 11 and is kept out of the reconstruction. In Figure 8.12-c the time-frequency analysis of the reconstructed signal is shown. The period of rotation of the rotor and their Doppler shift are now clearly observed.

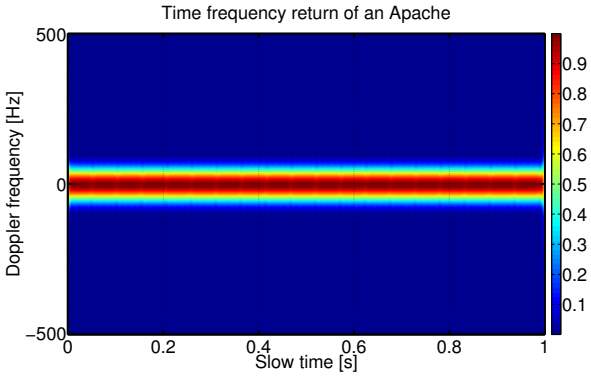


(a)

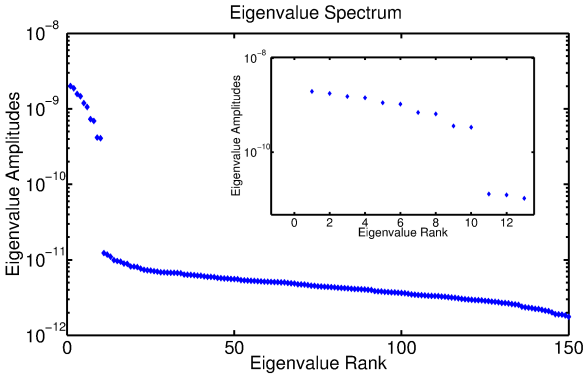


(b)

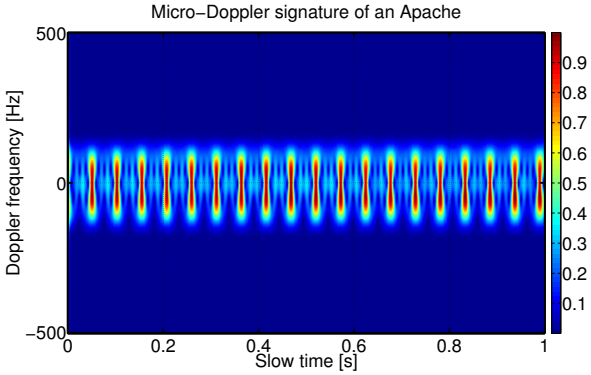


(c)

Figure 8.12: a) Time-Frequency return of an Apache b) its eigenvalues spectrum and c) the extracted micro-Doppler signature of the rotor blades.

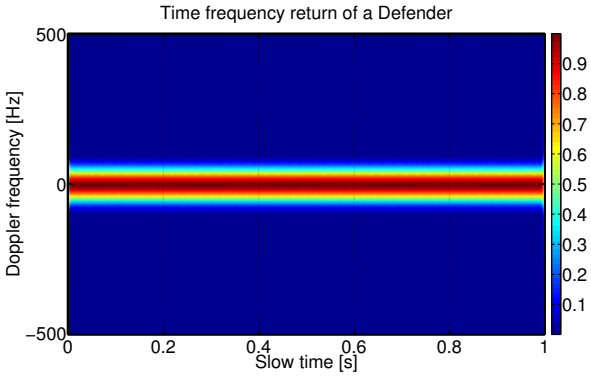


(a)

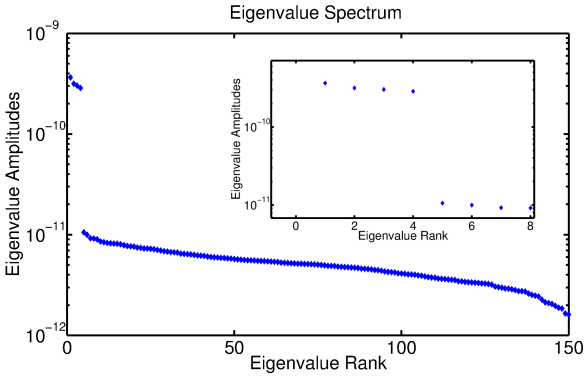


(b)

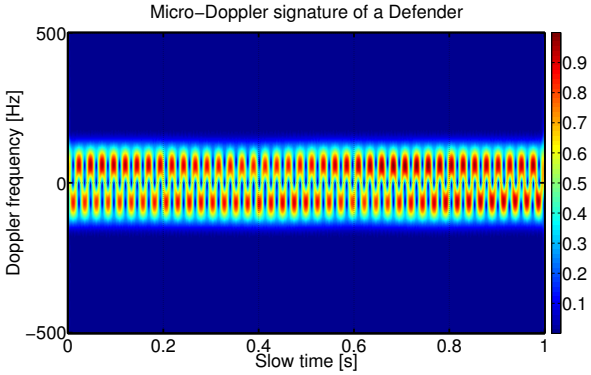


(c)

Figure 8.13: a) Time-Frequency return of a Defender b) its eigenvalues spectrum and c) the extracted micro-Doppler signature of the rotor blades.

For the case shown in Figure 8.12-c the period of the rotation can be obtained from the flashes and is measured to be 4.78 rps. The maximum amplitude of the micro-Doppler shift measured at the -3 dB point is of 101.15 Hz. From this information, the

following formula can be used to estimate the blade length:

$$\hat{L}_b = \frac{\hat{f}_{mD_{max}}\lambda}{\cos\left(\frac{\beta}{2}\right)\cos(\delta)2\pi\hat{\mathbf{\Omega}}} \tag{8.6}$$

where, $\hat{L}_b$ is the estimated blade length, $\hat{f}_{mD_{max}}$ and $\hat{\mathbf{\Omega}}$ are the estimated maximum Doppler shift and rotation rate respectively. From equation (8.6) for the case of the Apache the estimated blade length of 7.25 m, close to the simulated value seen in Table 8.3.

For the simulated case the bistatic angle is $169.9$ degrees while $\delta$ is of $10.30$ degrees. In Figure 8.13-b the eigenvalues spectrum obtained using the SSA with an embedding length of 150 samples is shown for the case of the Defender. It is possible to identify the first strong component that contains the strong clutter return, while the others contain other features of the echoes. Components 2 to 4 are used to reconstruct the micro-Doppler signatures, while component 5 and higher is considered noise. In Figure 8.13-c the time-frequency analysis of the reconstructed signal is shown. It can be seen that the rotational period of the rotor and their Doppler shift, in this case the measured rotating rate is 8.1566 rps and the maximum micro-Doppler frequency results to be of 97.39 Hz, these values leads to obtain a blade length of 4.0962 m that is a good estimation of the original length as seen in Table 8.3.

## 8.4 Conclusion

In this chapter advanced analysis of micro-Doppler and an extraction technique have been presented. The effect of wind turbines in SAR images has been modelled and studied through simulations. The effect of wind turbines on radar systems is of great interest due to their interference. In our work we showed that the effect on the focussed image changes with the orientation of the wind turbine with respect to the flight direction of the platform carrying the SAR sensor. We showed also that the effect changes with the rotating frequency of the wind turbine, similar dependence is expected for different blade lengths since the series of echoes can be modelled as a series of Bessel function with the amplitude depending on the wind turbine features.

Generally wind farms are composed of many turbines, which could lead to an image strongly affected by smearing and ghost echoes that could mask other features in the image. For example a wind farm could be used to temporary mask targets of military interest.

Further studies will be conducted on the removal of the effect of the wind turbines in order to obtain SAR images of good quality and the possible military and commercial exploitation of this effect.

In this chapter we also demonstrate the effectiveness of the use of the Singular Spectrum Analysis to extract micro-Doppler signatures from SAR and passive radar signals in clutter. The technique is robust with respect to high signal to clutter ratio providing an useful tool for micro-Doppler analysis in realistic environments. The SSA has been applied to simulated data with a very low SCR demonstrating that it is useful also for the extraction of this family of micro-Doppler signatures, maintaining their characterizing features.

# Chapter 9

# Conclusions and Future Works

This thesis investigated signal processing techniques, models and concept for radar imaging and micro-Doppler signatures analysis.

The basics of SAR imaging were introduced in Chapter 2. This chapter provided a review of the Range Doppler Algorithm and the Chirp Scaling Algorithm. In addition the Fractional Fourier Transform and the FrCSA algorithm were described. In Chapter 2 also the focussing problem in the bistatic SAR case was described and the different approaches for the development of an accurate focussing strategy were analysed. In particular two models for the bistatic point target spectrum were discussed in detail: the BPTS based on the Method of Series Reversion and the BPTS derived using the 2D Principle of Stationary Phase.

The review of micro-Doppler was presented in Chapter 3. The recent advances in radar based m-D analysis from radar imaging systems were introduced. The presented review indicated how the information produced from the micro-motions of a target can affect the return to a SAR/ISAR platform. The radar imaging community could then take advantage of this complementary source of information for example to remove uncertainty in automatic target recognition systems.

Two new SAR focussing algorithms were presented using the Fractional Fourier Transform applied to the Range Doppler Algorithm and to the Chirp Scaling algorithm in Chapter 4. The FrFT and a time-mapping operation were used to replace the matched filter used in the RDA and CSA. The resulting FrRDA and eFrCSA algorithms use the property of the Fractional Fourier Transform to resolve chirp signals to increase the

resolution of the point scatterers in the scene. The proposed approach was tested with simulated data and real Radarsat-1 data. For both the proposed algorithms the proposed approach showed to improve the quality of the impulse response both in terms of side lobes and resolution.

In Chapter 5 a new polynomial Chebyshev approximation of the bistatic slant range function and of the bistatic frequency coupling terms were analytically derived to improve the accuracy and the efficiency of bistatic SAR focussing algorithms. The proposed approximation is intended to replace the Taylor approximation used in Neo [2007]; Neo et al. [2007]; Wang et al. [2011] to derive the analytical bistatic point target spectrum. The proposed approximation is easy to compute and does not increase the computational complexity with respect to the Taylor based approach. The approximation error using the Taylor and the Chebyshev polynomials was evaluated, confirming the theoretical capability of the Chebyshev approach to minimize the norm of the error.

In Chapter 6 the micro-Doppler signatures from vibrating targets in bistatic SAR systems were investigated. The bistatic configuration with a fixed receiver was used to derive an expression for the bistatic micro Doppler signature. The effect on the focussed image was also analysed. The bistatic case shows a substantial difference to that of the traditional monostatic case. The bistatic micro Doppler signature is influenced by the bistatic geometry. The simulations confirmed the model that provides a useful tool for the analysis of the micro-Doppler signature from a bistatic SAR system. It was demonstrated that the bistatic configuration exhibits the advantage of a reduced minimum required PRF compared to that required in the monostatic SAR. Furthermore this reduces the effects of potential aliasing in the analysis of the micro-Doppler signature compared to the monostatic case.

A novel concept of Passive Bistatic Radar was investigated in Chapter 7. The proposed system exploits the GNSS signal when a target is in the near forward scattering zone for micro-Doppler analysis. The feasibility study provided the budget analysis showing that by exploiting the forward scattering enhancement it is possible to obtain enough forward scattered power from the rotor blades of an helicopter. The proposed PBR system was simulated and the presence of different helicopters flying in the near

forward scattering zone has been simulated. The micro-Doppler signature relative to their rotor blades in this kind of system was analysed and the possibility to extract the rotor blades features from it was shown with a good confidence in the possibility to recognize the specific helicopter.

In Chapter 8 advanced analysis of micro-Doppler and an extraction technique were presented. The effect of wind turbines in SAR images was modelled and studied through simulations. The effect of wind turbines on radar systems is of great interest due to their interference. The effect on the focussed image changes with the orientation of the wind turbine with respect to the flight direction of the platform carrying the SAR sensor. We showed also that the effect changes with the rotating frequency of the wind turbine, similar dependence is expected for different blade lengths since the series of echoes can be modelled as a series of Bessel function with the amplitude depending on the wind turbine features.

In the same chapter we also demonstrated the effectiveness of the use of the Singular Spectrum Analysis to extract micro-Doppler signatures from SAR and passive radar signals in clutter. The technique is robust with respect to low signal to clutter ratio providing an useful tool for micro-Doppler analysis in realistic environments.

## 9.1 Future Directions

Based on the research presented throughout this thesis, different research areas will be of interest for potential further investigation.

**Further testing of the 2D PSP based focussing RDA with Chebyshev approximation**: The bistatic Range Doppler Algorithm that derives directly from the 2D PSP BPTS can be tested with both versions of the BPTS ( Taylor and Chebyshev). The efficiency and the accuracy could be analysed and discussed in the future.

**Application of the SSA to human micro-Doppler:** The SSA can be applied also in the case of radar micro-Doppler of humans, for example it could be exploited for the extraction of the micro-Doppler signature of the chest due to the breathing from clutter in order to detect humans for rescue operations.

**Feature extraction for micro-Doppler classification:** Investigation of novel tech-

niques for the extraction of the micro-Doppler features. The extracted features can be used in classifiers in order to provide a robust classification system based on micro-Doppler signatures.

**Implementation of micro-Doppler extraction and classification on embedded platforms:** In order to get a real time classification result, the time-frequency analysis, the feature extraction and the classification stage must be accomplished in a reasonable time. For this reason a future development will be the realization of the micro-Doppler classification chain on high performance DSP processors.

Furthermore the proposed algorithms and can be applied in many other areas of interest including sonar, biomedical engineering, and communications.

# Appendix A

# Chebyshev Polynomial Approximation

## A.1 Polynomial Approximation

Weistrass theorem Rivlin [2003] suggests that polynomial approximation of continuous function in an interval $[a, b]$ can be always performed. The objective is to represent a continuous function $f(x)$ with a polynomial in the form:

$$f(x) \approx a_0 + a_1 x + a_2 x^2 + \cdots + a_n x^n \tag{A.1}$$

where n is the approximation order.

A diffused approach in obtaining an approximating polynomial is to minimize the square residual for the approximation of a function. It is defined as Rivlin [2003]:

$$e^2 = \sum_{i=1}^{k} [y_i - (a_0 + a_1 x_i + \cdots + a_n x_i^n)]^2 \tag{A.2}$$

where $y$ is the discrete version of $f(x)$. This minimization finds a solution for the least squares problem, which is solved using an interpolating polynomial families of orthogonal polynomials.

The orthogonal Chebyshev polynomials allows to obtain an approximation which minimizes the error in the sense of the least squares Rivlin [2003] and the infinity norm $||\cdot||_\infty$, hence reducing the so called Runge phenomenon, meaning that the maximum approximation error is bounded.

### A.1.1 Chebyshev Polynomials

Chebyshev polynomials play an important role in numerical analysis J.Mason [1996]. They have been used in approximation of functions, computation of integrals, and solution of differential equations. These polynomials have many properties, including:

- Continuous
- The least deviation from zero property
- The recurrence relation that leads to efficient computation

There are four families of Chebyshev polynomials. Their power derive from the close relation with the trigonometric function *cosine* and *sine* functions. The first kind is defined as:

$$T_n(x) = \cos n\theta \qquad where \qquad x = \cos\theta \tag{A.3}$$

where $x\epsilon[-1, 1]$, and $\theta\epsilon[0, \pi]$.
Recurrence relation for this kind of Chebyshev polynomial can also be obtained by:

$$T_n(x) = 2nT_{n-1}(x) - T_{n-2}(x) \quad n = 2, 3, \cdots \tag{A.4}$$

with initial conditions:

$$T_0(x) = 1 \quad and \quad T_1(x) = x; \tag{A.5}$$

This is the most common kind and is used in this thesis.

#### A.1.1.1 Chebyshev series expansion

Restricting the range on [-1,1], Chebyshev series expansion of $f(x)$ can be expressed in the form:

$$f(x) \simeq \sum_{i=0}^{\infty} c_i T_i(x) = c_0 T_0(x) + c_1 T_1(x) + \cdots \tag{A.6}$$

where $c_i$ are the Chebyshev coefficients computed using the Chebyshev nodes.

### A.1.1.2 Chebyshev nodes and coefficients

Due to the so called Runge phenomenon J.Mason [1996] the set of zeroes of the Chebyshev poynomial can make the interpolation more efficient and stable. The Chebyshev nodes for $x\epsilon[-1,1]$ are defined as:

$$x_k = cos\left(\left(\frac{2k+1}{2(n+1)}\right)\pi\right), \quad k = 0,1,...,n \tag{A.7}$$

The more general formulation for the nodes in the interval [a,b] is given by:

$$x_k = \frac{a+b}{2} + \left(\frac{b-a}{2}\right) cos\left(\left(\frac{2k+1}{2(n+1)}\right)\pi\right) \tag{A.8}$$

The Chebyshev coefficients computed in the Chebyshev nodes allows us to obtain uniform convergence for $n \to \infty$. The coefficients are defined as:

$$c_0 = \frac{1}{n+1}\sum_{k=0}^{n} f(x_k)T_0(x_k) \quad c_j = \frac{1}{n+2}\sum_{k=0}^{n} f(x_k)T_j(x_k) \tag{A.9}$$

After the coefficients have been calculated, the interpolating polynomial of $f(x)$ can be defined as follows:

$$f(x) \simeq P_n(x) = \sum_{j=0}^{n} c_j T_j(x) \tag{A.10}$$

where $n$ is the approximation order.

# Author's Publications

## Journals

- **Carmine Clemente, John J. Soraghan** ,*"Approximation of the Bistatic Slant Range Using Chebyshev Polynomials"*, IEEE Geoscience and Remote Sensing Letters Vol.9, Issue 4, pages 682-686.

- **Carmine Clemente, John J. Soraghan** ,*"Vibrating Target Micro-Doppler Signature in Bistatic SAR with a Fixed Receiver"*, IEEE Transactions on Geoscience and Remote Sensing, Vol. 50, No 8, pages 3219-3227.

- **Carmine Clemente, John J. Soraghan** ,*"Range Doppler and Chirp Scaling Processing of SAR Data using the Fractional Fourier Transform"*, IET Signal Processing. Vol. 6, No 5, pages 503-510.

## Conferences

- **T. Beltramonte, C. Clemente, M. di Bisceglie, C. Galdi**,*"Robust Multiband Detection Of Thermal Anomalies Using The Minimum Covariance Determinant Estimator"*,2009 IEEE International Geoscience and Remote Sensing Symposium, July 13-17 2009, Cape Town-South Africa.

- **C. Clemente, M. di Bisceglie, M. Di Santo, N. Ranaldo, M. Spinelli**, *"Processing of synthetic aperture radar data with GPGPU"*, 2009 IEEE Workshop on Signal Processing Systems, October 07-09 2009, Tampere-Finland.

- **Carmine Clemente, John J. Soraghan**, *"Range Doppler SAR processing Using the fractional Fourier Transform"*,International Radar Symposium, IRS2010, June 15-18 2010, Vilnius-Lithuania.

- **Carmine Clemente, John J. Soraghan** ,*"Fractional RDA and Enhanced FrCSA for SAR Imaging"*, Sensor Signal Processing For Defence, SSPD-2010, 29-30 September 2010 ,London

- **Sherif Elgamel, Carmine Clemente, John J. Soraghan** ,*"Radar Matched Filtering using the Fractional Fourier Transform"*, Sensor Signal Processing For Defence, SSPD-2010, 29-30 September 2010 ,London

- **Carmine Clemente, John J. Soraghan** ,*"Fractional Range Doppler Algorithm for SAR Imaging"*, European Radar Conference, Eurad-2010, September 26-October 1, Paris

- **Carmine Clemente, John J. Soraghan** ,*"Bistatic Slant Range Approximation using Chebyshev Polynomials"*, IEEE Radar Conference 2011, Radarconf2011, May 23-27, Kansas City, USA

- **Carmine Clemente, John J. Soraghan**,*"Characterization of Vibrating Targets in Bistatic SAR"*, Sensor Signal Processing For Defence, SSPD-2011, 28-29 September 2011, London

- **Carmine Clemente, John J. Soraghan**,*"On the Effect of Vibrating Targets in Bistatic SAR Images"*, 2nd IMA Conference on Mathematics in Defence, 20 October 2011, Swindon, United Kingdom.

- **Carmine Clemente, John J. Soraghan**,*"Vibrating Micro-Doppler signature extraction from SAR data using Singular Value Decomposition"*, EUSAR2012, European Conference on Synthetic Aperture Radar.

- **Carmine Clemente, John J. Soraghan**, *"Passive Bistatic Radar for Helicopters Classification: a Feasibility Study"*, IEEE Radar Conference 2012, May 7-11,

Atlanta, USA

- **P. Lipinski, S. McCabe, A. Stark, G. Di Caterina, C. Clemente and J. J. Soraghan**, *"RoboKinect - A low-cost mobile vision system for 2.5D object detection"* , 5th European DSP Education and Research Conference (EDERC) 2012, 13-14 September 2012, Amsterdam (NL)

- **Jaime Zabalza, Jinchang Ren, Carmine Clemente, Gaetano Di Caterina and J. J. Soraghan**, *"Embedded SVM on TMS320C6713 for Signal Prediction in Classification and Regression Applications"*, 5th European DSP Education and Research Conference (EDERC) 2012, 13-14 September 2012, Amsterdam (NL)

- **Carmine Clemente, John J. Soraghan**, *"Chebyshev Expansion for Accurate and Efficient 2D PSP Bistatic Point Target Spectrum"* , Sensor Signal Processing For Defence, SSPD 2012, 25- 27 September 2012, London (UK)

- **Carmine Clemente, John J. Soraghan**, *"Application of the singular spectrum analysis for extraction of micro-Doppler signature of helicopters"* , IET Radar Conference 2012, 22-25 October 2012 Glasgow (UK)

- **Carmine Clemente, John J. Soraghan**, *"Analysis of the effect of wind turbines in SAR images"* , IET Radar Conference 2012, 22-25 October 2012, Glasgow (UK)

# Book Reviews

- **Carmine Clemente**,*"Review of the book "The micro-Doppler effect in Radar" by Victor C. Chen"*, The Aeronautical Journal, February 2012.

# Submitted Papers

- **C. Clemente, J. Soraghan**,*"GNSS Based Passive Bistatic Radar for micro-Doppler analysis of helicopter rotor blades"*, IEEE Transactions on Aerospace

and Electronic Systems

- **Carmine Clemente, Alessio Balleri, Karl Woodbridge, John Soraghan**, *"Developments in Target Micro-Doppler Signatures: Imaging, Ultrasound and Through-the-Wall Radar"*, Eurasip Journal on Advances in Signal Processing, Special Issue on Emerging Radar Techniques

# References

Rea sar processor. http://www.eonic.com/. 10

A. S. Amein and J. J. Soraghan. Azimuth Fractional Transformation of the Fractional Chirp Scaling Algorithm (FrCSA). *IEEE Transactions on Geoscience and Remote Sensing*, 44:2871–2879, October 2006. 14, 17, 55, 61, 65

M.A Abutheraa and D Lester. Computable Function Representation Using Effective Chebyshev Polynomial. *Proc of the 4th CMSE*, 2007. 72

T. Alieva, V. Lopez, F. Agullo-Lopez, and L. B. Almeida. The Fractional Fourier Transform in optical propagation problems. *Journal of the Modern Optics*, 41(5): 1037–1044, May 1994. 15

L. B. Almeida. The fractional Fourier Transform and time-frequency representations. *IEEE Transactions on Signal Processing*, 42(11):3084–3091, November 1994. 15

A. S. Amein and J. J. Soraghan. Fractional chirp scaling algorithm: Mathematical model. *IEEE Transactions on Signal Processing*, 55:4162–4172, August 2007. xv, 14, 17, 55, 61, 65, 66

A.Papoulis. *Systems and Transforms With Applications in Optics*. Krieger Pub Co, 1981. 19

Xueru Bai, Mengdao Xing, Feng Zhou, Guangyue Lu, and Zheng Bao. Imaging of micromotion targets with rotating parts based on empirical-mode decomposition. *IEEE Transactions on Geoscience and Remote Sensing*, 46(11):3514 –3523, nov. 2008. ISSN 0196-2892. doi: 10.1109/TGRS.2008.2002322. xi, 50, 51, 52

Xueru Bai, Feng Zhou, Mengdao Xing, and Zheng Bao. High resolution isar imaging of targets with rotating parts. *IEEE Transactions on Aerospace and Electronic Systems*, 47(4):2530 –2543, october 2011. ISSN 0018-9251. doi: 10.1109/TAES.2011.6034649. xi, 51, 52, 53

R. Bamler and E. Boerner. On the use of numerically computed transfer functions for processing of data from bistatic SARs and high squint orbital SARs. In *Geoscience and Remote Sensing Symposium, 2005. IGARSS '05. Proceedings. 2005 IEEE International*, volume 2, pages 1051 – 1055, july 2005. doi: 10.1109/IGARSS.2005.1525295. 23, 24

R. Bamler, H.Breit, U. Steinbrecher, and D. Just. Algorithm for X-SAR processing. In *Geoscience and Remote Sensing Symposium, 1993. IGARSS '93 Proceedings, Tokyo, Vol.4*, pages 1589–1592, August 1993. 10

Zhu Ben-yu, Xue Lei, and Bi Da-ping. A micro-motion feature deception jamming method to isar. In *IEEE 10th International Conference on Signal Processing (ICSP)*, pages 2287 –2290, oct. 2010. doi: 10.1109/ICOSP.2010.5655184. xi, 52, 53, 54

Li Bin, Wan Jian-wei, Yao Kang-ze, Wang Yan, Ci Lin-lin, and Lu Jun. ISAR based on micro-doppler analysis and Chirplet parameter separation. In *1st Asian and Pacific Conference on Synthetic Aperture Radar, 2007. APSAR 2007.*, pages 379 –384, nov. 2007. doi: 10.1109/APSAR.2007.4418631. 49

S. Bjorklund, T. Johansson, and H. Petersson. Evaluation of a micro-doppler classification method on mm-wave data. In *2012 IEEE Radar Conference (RADAR)*, pages 0934 –0939, may 2012. doi: 10.1109/RADAR.2012.6212271. 37

B. Borden. The Fractional Fourier Tranform and ISAR imaging. *Inverse Problem Letters, IOP*, 16(2):547–559, April 2000. 16

A. Bultheel and H. Martinez. A shattered Survey of the Fractional Furier Transform, 2002. http://nalag.cs.kuleuven.be/papers/ade/frft/index.html. 14, 57

C. Capus and K. Brown. Short-time fractional Fourier methods for the time-frequency

representation of chirp signals. *Journal of the Acoustical Society of America*, 113 (6):3253–3263, June 2003. 16, 57

C.Gierull, C. Pike, and F.Paquet. Mitigation of phase noise in bistatic SAR systems with extremely large synthetic apertures. In *Proc. European Conference of Synthetic Aperture Radar,EUSAR'06, Dresden, Germany*, 2006. 20

V. Chen. *Micro-Doppler Effect in Radar*. Artech House, first edition, 2011. 2, 3, 36, 37, 38, 108, 109, 110, 111, 112

V.C. Chen, F. Li, S.-S. Ho, and H. Wechsler. Micro-Doppler effect in radar: phenomenon, model, and simulation study. *IEEE Transactions on Aerospace and Electronic Systems*, 42(1):2 – 21, 2006. ISSN 0018-9251. doi: 10.1109/TAES.2006.1603402. 36, 39, 45, 91, 92, 127, 128

V.C. Chen, W.J. Miceli, and B. Himed. Micro-Doppler analysis in ISAR - review and perspectives. In *International Radar Conference - Surveillance for a Safer World, 2009.*, pages 1 –6, oct. 2009. 49

Mikhail Cherniakov. *Bistatic Radar: Emerging Technology*. John Wiley, Ltd, 2008. 20, 21, 105, 113

C. Clemente and J.J. Soraghan. Fractional RDA and Enhanced FrCSA for sar imaging. In *Sensor Signal Processing for Defence, SSPD-2010, London*, sept. 2010. 61

C. Clemente, M. di Bisceglie, M. Di Santo, N. Ranaldo, and M. Spinelli. Processing of synthetic Aperture Radar data with GPGPU. In *IEEE Workshop on Signal Processing Systems, 2009. SiPS 2009.*, pages 309 –314, oct. 2009. doi: 10.1109/SIPS.2009.5336272. 2, 11, 63

L. Cohen. Time-frequency distributions-a review. *Proceedings of the IEEE*, 77(7):941 –981, July 1989. ISSN 0018-9219. doi: 10.1109/5.30749. 99, 135

I.G. Cumming and F.H. Wong. *Digital Processing of Synthetic Aperture Radar Data: Algorithms and Implementation*. Artech House Publishers, first edition, 2005. 2, 8, 10, 13, 21, 24, 57, 60, 66, 99, 129, 135

C.Wu. A digital system to produce imagery from SAR data. In *AIAA, System Design Driven By Sensors*, October 1976. 10

C.Wu. Processing of SEASAT SAR data. In *SAR Technology Symp., Las Cruces, NM*, September 1977. 10

D. Mendlovic and H.M. Ozaktas. Fractional Fourier Transforms and their optical implementation: I. *Journal of the Optical Society of America A*, 10(9):1875–1881, September 1993. 15

D. D'Aria, A.M. Guarnieri, and F. Rocca. Focusing bistatic synthetic aperture radar using dip move out. *IEEE Transactions on Geoscience and Remote Sensing*, 42(7): 1362 – 1376, july 2004. ISSN 0196-2892. doi: 10.1109/TGRS.2004.830166. 25

M. di Bisceglie, M. Di Santo, C. Galdi, R. Lanari, and N. Ranaldo. Synthetic Aperture Radar Processing with GPGPU. *IEEE Signal Processing Magazine*, 27(2):69 –78, mar. 2010. ISSN 1053-5888. doi: 10.1109/MSP.2009.935383. 11, 63

S. Duque, P. Lopez-Dekker, and J.J. Mallorqui. Single-Pass Bistatic SAR Interferometry Using Fixed-Receiver Configurations: Theory and Experimental Validation. *IEEE Transactions on Geoscience and Remote Sensing*, 48(6):2740 –2749, 2010. ISSN 0196-2892. doi: 10.1109/TGRS.2010.2041063. 86

A. G. Dempster E. P. Glennon. Feasibility of Air Target Detection Using GPS as a Bistatic Radar. *Journal of Global Positioning System*. 113, 116, 118

J.H.F. Ender and A.R. Brenner. PAMIR- a wideband phased array SAR/MTI system. *IEE Proceedings Radar, Sonar and Navigation*, 150(3):165 –172, june 2003. ISSN 1350-2395. doi: 10.1049/ip-rsn:20030445. 94

Leopold B. Felsen, Mauro Mongiardo, and Peter Russer. *Electromagnetic Field Computation by Network Methods*. Springer, 2009. 113

G. Franceschetti and R. Lanari. *Synthetic Aperture Radar Processing*. Boca Raton, CRC Press, 1999. 32

Su Fulin and Jiu Mingyuan. ISAR Imaging of Target with Micro-motion Parts Based on SSA. *2010 8th European Conference on Synthetic Aperture Radar (EUSAR)*, pages 1 –4, june 2010. xi, 49, 50, 51

B. Gallardo-Hernando, J.M. Munoz-Ferreras, F. Perez-Martinez, and F. Aguado-Encabo. Wind turbine clutter observations and theoretical validation for meteorological radar applications. *IET Radar, Sonar Navigation*, 5(2):111 –117, feb. 2011. ISSN 1751-8784. doi: 10.1049/iet-rsn.2009.0296. 48, 127

A. Ghaleb, L. Vignaud, and J.M. Nicolas. Micro-Doppler analysis of wheels and pedestrians in ISAR imaging. *IET Signal Processing*, 2(3):301 –311, september 2008. ISSN 1751-9675. doi: 10.1049/iet-spr:20070113. 49

A. Giancaspro, L. Candela, E. Lopinto, V.A. Lore, and G. Milillo. COSMO-SkyMed SAR processing parallel implementation. In *2002 IEEE International Geoscience and Remote Sensing Symposium, 2002. IGARSS '02.*, volume 6, pages 3165 – 3166 vol.6, 2002. doi: 10.1109/IGARSS.2002.1027118. 11

J. Glaser. Forward Scatter Radar for Future Systems. *WSTIAC Quarterly*, 10(3), March 2011. 113

S. Gleason and D. Gebre-Egziabher. *GNSS Applications and Methods*. Artech House, 2009. 105

N. et al Golyandina. *Analysis of Time Series Structrure: SSA and Related Techniques.* Chapman & HallCRC, 2001. 134

H. Griffiths and C. Baker. The signal and interference environment in passive bistatic radar. In *Information, Decision and Control, 2007. IDC '07*, pages 1 –10, feb. 2007. doi: 10.1109/IDC.2007.374516. 116, 117

H. Griffiths, Y. Ohya, A. Balleri, K. Tong, A. Al-Armaghany, T. Matsuura, and T. Karasudani. Measurement and analysis of the radar signature of a new type of wind turbine. In *2011 IEEE CIE International Conference on Radar (Radar)*, volume 1, pages 837 –840, oct. 2011. doi: 10.1109/CIE-Radar.2011.6159671. 48

H Hassani. Singular spectrum analysis: methodology and comparison. *mpra.ub.uni-muenchen.de*, Jan 2007. URL http://mpra.ub.uni-muenchen.de/4991/2/MPRA_paper_4991.pdf. 134

X. He, T. Zeng, and M. Cherniakov. Signal detectability in SS-BSAR with GNSS non-cooperative transmitter. *IEE Proceedings Radar, Sonar and Navigation*, 152 (3):124–132, june 2005. ISSN 1350-2395. doi: 10.1049/ip-rsn:20045042. 113

P.E. Howland, H.D. Griffiths, and C.J Baker. *Passive Bistatic Radar: Emerging Technology*, chapter Passive Bistatic Radar. Wiley, 2008. 107, 117

W. Hughes, K. Gault, and G.J. Princz. A comparison of the Range-Doppler and Chirp Scaling algorithms with reference to RADARSAT. In *Geoscience and Remote Sensing Symposium, 1996. IGARSS '96. 'Remote Sensing for a Sustainable Future.', International*, volume 2, pages 1221 –1223 vol.2, may 1996. doi: 10.1109/IGARSS.1996.516621. 63

J.Mason. *Chebyshev Polynomial:Theory and Applications*. Kluwer Academic, 1996. 71, 72, 73, 150, 151

A.M Kinghorn and A Nejman. PicoSAR- an advanced lightweight SAR system. In *European Radar Conference, 2009. EuRAD 2009.*, pages 168–171, 2009. 97

V. Koch and R. Westphal. A new approach to a multistatic passive radar sensor for air defense. In *Radar Conference, 1995., Record of the IEEE 1995 International*, pages 22–28, may 1995. doi: 10.1109/RADAR.1995.522513. 113

Fanxing Kong, Yan Zhang, R. Palmer, and Ying Bai. Wind turbine radar signature characterization by laboratory measurements. In *2011 IEEE Radar Conference (RADAR)*, pages 162 –166, may 2011. doi: 10.1109/RADAR.2011.5960520. 48

Gerhard Krieger and Younis Marwan. Impact of Oscillator Noise in Bistatic and Multistatic SAR. *IEEE Geoscience and Remote Sensing Letters*, 3(3):424 – 429, july 2006. 21

M. A. Kutay, H. M. Ozaktas, O. Arikan, and L. Onural. Optimal filtering in fractional fourier domains. *IEEE Transactions On Signal Processing*, 45(5):1129–1143, May 1997. 15

Xiang Li, Bin Deng, Yuliang Qin, Hongqiang Wang, and Yanpeng Li. The Influence of Target Micromotion on SAR and GMTI. *IEEE Transactions on Geoscience and Remote Sensing*, 49(7):2738 –2751, july 2011. ISSN 0196-2892. doi: 10.1109/TGRS.2011.2104965. 46, 48

O. Loffeld, H. Nies, V. Peters, and S. Knedlik. Models and useful relations for bistatic SAR processing. In *2003 IEEE International Geoscience and Remote Sensing Symposium, 2003. IGARSS '03. Proceedings.*, volume 3, pages 1442 – 1445, july 2003. doi: 10.1109/IGARSS.2003.1294138. 23, 25

J Mason. Chebyshev polynomials of the second, third and fourth kinds in approximation, indefinite integration, and integral transforms. *Journal of Computational and Applied Mathematics*, Jan 1993. URL http://www.sciencedirect.com/science/article/pii/0377042793901485. 72, 73

D. Mendlovic and H.M. Ozaktas. Fractional Fourier Transforms and their optical implementation: II. *Journal of the Optical Society of America A*, 10(12):2522–2531, December 1993. 15

B. Mojarrabi, J. Homer, K. Kubik, and I.D. Longstaff. Power budget study for passive target detection and imaging using secondary applications of GPS signals in bistatic radar systems. In *IEEE International Geoscience and Remote Sensing Symposium, 2002. IGARSS '02.* , volume 1, pages 449–451 vol.1, 2002. doi: 10.1109/IGARSS.2002.1025069. 113

P. Molchanov, J. Astola, K. Egiazarian, and A. Totsky. Ground moving target classification by using DCT coefficients extracted from micro-Doppler radar signatures and artificial neuron network. In *Microwaves, Radar and Remote Sensing Symposium (MRRS), 2011*, pages 173 –176, aug. 2011a. doi: 10.1109/MRRS.2011.6053628. 37

P. Molchanov, J. Astola, K. Egiazarian, and A. Totsky. Classification of ground moving radar targets by using joint time-frequency analysis. In *2012 IEEE Radar Conference (RADAR)*, pages 0366 –0371, may 2012. doi: 10.1109/RADAR.2012.6212166. 37, 112

Pavel A. Molchanov, Jaakko T. Astola, Karen O. Egiazarian, Grigory I. Khlopov, Vladimir Ye. Morozov, Boris B. Pospelov, and Alexander V. Totsky. Object recognition in ground surveillance doppler radar by using bispectrum-based time-frequency distributions. In *11th International Radar Symposium (IRS), 2010*, pages 1 –4, june 2010. 37

P.O. Molchanov, J.T. Astola, K.O. Egiazarian, and A.V. Totsky. Moving target classification in ground surveillance radar ATR system by using novel bicepstral-based information features. In *2011 European Radar Conference (EuRAD)*, pages 194 –197, oct. 2011b. 37

P.M. Morse and H. Feshbach. *Methods of Theoretical Physics, Part I*. McGraw-Hill, 1953. 26

V. Namias. The fractional order fourier transform and its application to quantum mechanics. *Journal of Institute of Mathematics and its Applications*, pages 241–265, 1980. 15

Yew Lam Neo. *Digital Processing Algorithms for Bistatic Synthetic Aperture Radar Data*. PhD thesis, The University of British Columbia, 2007. 23, 26, 55, 71, 72, 73, 74, 83, 87, 146

Yew Lam Neo, F. Wong, and I.G. Cumming. A Two-Dimensional Spectrum for Bistatic SAR Processing Using Series Reversion. *IEEE Geoscience and Remote Sensing Letters*, 4(1):93 –96, jan 2007. ISSN 1545-598X. doi: 10.1109/LGRS.2006.885862. 26, 71, 72, 73, 74, 84, 146

Yew Lam Neo, F.H. Wong, and I.G. Cumming. Processing of Azimuth-Invariant Bistatic SAR Data Using the Range Doppler Algorithm. *IEEE Transactions on*

*Geoscience and Remote Sensing*, 46(1):14 –21, jan. 2008. ISSN 0196-2892. doi: 10.1109/TGRS.2007.909090. 29

L.M. Novak, G.J. Owirka, and W.S. Brower. An efficient multi-target SAR ATR algorithm. In *Conference Record of the Thirty-Second Asilomar Conference o Signals, Systems amp; Computers, 1998.*, volume 1, pages 3 –13 vol.1, nov. 1998. doi: 10.1109/ACSSC.1998.750815. 41

H.M. Ozaktas, Z. Zalevsky, and M. A . Kutay. *The Fractional Fourier Tranform with applications in Optics and Signal processing*. John Wiley & Sons Ltd, UK, January 2001. 15, 16

J. Perry and A. Biss. Wind farm clutter mitigation in air surveillance radar. In *2007 IEEE Radar Conference*, pages 93 –98, april 2007. doi: 10.1109/RADAR.2007.374197. 47

POfacets. Radar cross section calculations using the physical optics approximation, pofacets. http://faculty.nps.edu/jenn/. 115, 140

P. Pouliguen, L. Lucas, F. Muller, S. Quete, and C. Terret. Calculation and analysis of electromagnetic scattering by helicopter rotating blades. *IEEE Transactions on Antennas and Propagation*, 50(10):1396 – 1408, oct 2002. ISSN 0018-926X. doi: 10.1109/TAP.2002.800693. 115

P. Pouliguen, J.F. Damiens, and R. Moulinet. Radar signatures of helicopter rotors in great bistatism. In *Antennas and Propagation Society International Symposium, 2003. IEEE*, volume 3, pages 536 – 539 vol.3, june 2003. doi: 10.1109/APS.2003.1219904. 115

Radarsat-1. Canadian Space Agency. URL `http://www.asc-csa.gc.ca/eng/satellites/radarsat1/`. 66

R.K. Raney, H. Runge, R. Bamler, I.G. Cumming, and F.H. Wong. Precision SAR processing using chirp scaling. *IEEE Transactions on Geoscience and Remote Sensing*, 32:768–799, July 1994. 12, 14, 61

Theodore J. Rivlin. *An Introduction to the Approximation of Functions*. Dover Publications, 2003. 72, 149

M. Ruegg, E. Meier, and D. Nuesch. Vibration and Rotation in Millimeter-Wave SAR. *IEEE Transactions on Geoscience and Remote Sensing*, 45(2):293 –304, 2007. ISSN 0196-2892. doi: 10.1109/TGRS.2006.887025. xi, 42, 44, 45, 46, 47, 48, 90, 91, 93, 110, 127, 128

H. Schimpf, H. Essen, S. Boehmsdorff, and T. Brehm. MEMPHIS-a fully polarimetric experimental radar. In *2002 IEEE International Geoscience and Remote Sensing Symposium, 2002. IGARSS '02.*, volume 3, pages 1714 – 1716 vol.3, june 2002. doi: 10.1109/IGARSS.2002.1026230. 97

K. Siegel. Bistatic radars and forward scattering. In *Proceedings of the National Conference on Aeronautical Electronics*, pages 286–290, May 1958. 114

S.D. Silverstein and C.E. Hawkins. Synthetic aperture radar image signatures of rotating objects. In *Conference Record of the Thirty-Eighth Asilomar Conference on Signals, Systems and Computers, 2004.*, volume 2, pages 1663 – 1667 Vol.2, nov. 2004. doi: 10.1109/ACSSC.2004.1399441. 44

M. I. Skolnik. *Introduction to Radar Systems*. McGraw-Hill, 1981. 107, 115

G.E. Smith, K. Woodbridge, and C.J. Baker. Multistatic Micro-Doppler Signature of personnel. In *2008. RADAR '08. IEEE Radar Conference*, pages 1 –6, may 2008. doi: 10.1109/RADAR.2008.4721060. 37

G.E. Smith, K. Woodbridge, C.J. Baker, and H. Griffiths. Multistatic micro-Doppler radar signatures of personnel targets. *IET Signal Processing*, 4(3):224 –233, june 2010a. ISSN 1751-9675. doi: 10.1049/iet-spr.2009.0058. 37

Graeme E. Smith, Karl Woodbridge, and Chris J. Baker. Template based micro-doppler signature classification. In *The Institution of Engineering and Technology Seminar on High Resolution Imaging and Target Classification, 2006.*, pages 127 –144, nov. 2006. 37

Graeme E. Smith, Karl Woodbridge, and Chris J. Baker. Radar Micro-Doppler Signature Classification using Dynamic Time Warping. *IEEE Transactions on Aerospace and Electronic Systems*, 46(3):1078 –1096, july 2010b. ISSN 0018-9251. doi: 10.1109/TAES.2010.5545175. 37

T. Sparr. Moving target motion estimation and focusing in SAR images. In *2005 IEEE International Radar Conference*, pages 290 – 294, may 2005. doi: 10.1109/RADAR.2005.1435836. xi, 44

T. Sparr and B. Krane. Micro-Doppler analysis of vibrating targets in SAR. *IEE Proceedings Radar, Sonar and Navigation*, 150(4):277–83, 2003a. ISSN 1350-2395. doi: 10.1049/ip-rsn:20030697. 90, 127

T. Sparr and B. Krane. Micro-Doppler analysis of vibrating targets in SAR. *IEE Proceedings - Radar, Sonar and Navigation*, 150(4):277–83, aug. 2003b. ISSN 1350-2395. doi: 10.1049/ip-rsn:20030697. x, xi, 42, 43

I. Suberviola, I. Mayordomo, and J. Mendizabal. Experimental Results of Air Target Detection With a GPS Forward-Scattering Radar. *IEEE Geoscience and Remote Sensing Letters*, PP(99):1–5, 2011. ISSN 1545-598X. doi: 10.1109/LGRS.2011.2159477. 113

D. Tahmoush and J. Silvious. Radar micro-doppler for long range front-view gait recognition. In *IEEE 3rd International Conference on Biometrics: Theory, Applications, and Systems, 2009. BTAS '09.*, pages 1 –6, sept. 2009. doi: 10.1109/BTAS.2009.5339049. 37

T. Thayaparan, L. Stankovic, P. Suresh, K. Venkataramaniah, S. SivaSankaraSai, T. Sairam, S. Shankar, and K. Nikhilesh. Focusing ISAR images of moving targets in real-time using time-frequency-based method. In *11th International Radar Symposium (IRS), 2010*, pages 1 –4, june 2010. 50

T. Tsao, D. Weiner, P. Varshney, H. Schwarzlander, M. Slamani, and S. Borek. Ambiguity function for a bistatic radar. In *Time-Frequency and Time-Scale Analysis,*

*1992., Proceedings of the IEEE-SP International Symposium*, pages 497 –500, oct 1992. doi: 10.1109/TFTSA.1992.274151. 111

F. Wang and X. Li. A New Method of Deriving Spectrum for Bistatic SAR Processing. *IEEE Geoscience and Remote Sensing Letters*, 7(3):483 –486, July 2010. ISSN 1545-598X. doi: 10.1109/LGRS.2009.2039695. 72

R. Wang, Yun Kai Deng, O. Loffeld, H. Nies, I. Walterscheid, T. Espeter, J. Klare, and J.H.G. Ender. Processing the Azimuth-Variant Bistatic SAR Data by Using Monostatic Imaging Algorithms Based on Two-Dimensional Principle of Stationary Phase. *IEEE Transactions on Geoscience and Remote Sensing*, 49(10):3504 –3520, oct. 2011. ISSN 0196-2892. doi: 10.1109/TGRS.2011.2129573. x, 26, 29, 30, 33, 34, 55, 71, 72, 81, 83, 84, 146

Charles Werner, Urs Wegmuller, Tazio Strozzi, and Andreas Wiesmann. GAMMA SAR AND INTERFEROMETRIC PROCESSING SOFTWARE. In *ERS-ENVISAT Symposium, Gothenburg, Sweden*, October 2000. 10, 66

Nicholas J. Willis. *Bistatic Radar*. Artech House, 1995. 106, 107, 108, 111, 113

F.H. Wong, I.G. Cumming, and Yew Lam Neo. Focusing Bistatic SAR Data Using the Nonlinear Chirp Scaling Algorithm. *IEEE Transactions on Geoscience and Remote Sensing*, 46(9):2493 –2505, sept. 2008. ISSN 0196-2892. doi: 10.1109/TGRS.2008.917599. 29

G Yates, A Horne, A Blake, and R Middleton. Bistatic sar image formation. *Radar Sonar and Navigation*, Jan 2006. URL `http://www.geo.uzh.ch/microsite/rsl-documents/research/SARlab/BistaticLiterature/Ver09/PDF/YHBM06.pdf`. 136

Feng Zhu, Ying Luo, Qun Zhang, You-Qian Feng, and You-Qing Bai. ISAR Imaging for Avian Species Identification With Frequency-Stepped Chirp Signals. *IEEE Geoscience and Remote Sensing Letters*, 7(1):151 –155, jan. 2010. ISSN 1545-598X. doi: 10.1109/LGRS.2009.2028902. 50